Multi-Scale and Topology Graphene-based Nanomaterials for Investigation and Modulation of Electrical Activity of Excitable Cells

Submitted in partial fulfillment of the requirements for the

degree of

Doctor of Philosophy

in

Department of Biomedical Engineering

Sahil Kumar Rastogi

B.Tech., Biotechnology, Indian Institute of Technology Guwahati

M.S., Biomedical Engineering, Carnegie Mellon University

Carnegie Mellon University Pittsburgh, PA

December 2019

ACKNOWDEGEMENTS

The last four years of graduate school at Carnegie Mellon University (CMU) were the most exciting as well as challenging phases of my life. They not only shaped me into a better scientist but also molded me into the person I am today. None of my achievements throughout these years would have been possible without the contribution from all my mentors, friends, colleagues and family.

First and foremost, I would like to thank my Ph.D. advisor, Dr. Tzahi Cohen-Karni. He always showed more faith in me than I had in myself. Reflecting back on the last four years, I realized that I achieved much more than I could have imagined, and it was all thanks to his constant support, dedication, his love for science and his confidence to dream big. His focus and passion for his work is contagious and motivates everyone around him to keep pushing and never back down from any challenge.

Another big motivation for me to pursue my Ph.D. was my former M.S. advisor, Dr. Ge Yang. When I first joined his lab for my M.S. research, he gave me all the freedom to explore what I wanted to do irrespective of his expertise in the field. He always did his best to keep the motivation level of his students as high as possible, and he made me believe that I could achieve whatever I wanted. I never had to think twice before knocking at his door to discuss problems, be it academic or personal. Each time we met, he always checked if I was doing well personally before talking about work. I would not have applied for Ph.D. programs if it wasn't for him. I thank him from the bottom of my heart and wish him all the luck and success in life.

It would not be fair if I don't acknowledge one of my idols, Prof. Ian Cheong. I had the pleasure of meeting and working with him during my summer internship at Temasek Life Sciences,

National University of Singapore, after my junior year at Indian Institute of Technology (IIT), Guwahati. He was the reason I decided to apply for graduate school. Working with him was one of the best experiences of my undergraduate studies. His passion towards science and his eagerness to help his fellow researchers and students is something that can't be explained in words. He is the perfect blend of intelligence, kindness and enthusiasm, and I hold him in high regard. I am very grateful to him and I hope he keeps impacting the lives of other people as he did for me.

I would like to thank Dr. Adam Feinberg, Dr. Chris Bettinger and Dr. Aryn Gittis, for agreeing to be part of my thesis committee and providing me with their valuable suggestions and insight, that helped me significantly in formulating my projects into a coherent thesis. I would also like to acknowledge the funding sources namely, Bushnell fellowship, National Science Foundation (CBET1552833) and the Office of Naval Research (N000141712368). Without their support, none of the work would have been possible.

For any graduate student, the lab mates and the team environment play a very critical role at both personal and professional levels. I am very grateful especially to Guru, Raghav and Anna for their unconditional friendship and for being with me through all the ups and downs. Thank you for always being there to listen to all my rants and frustrations, and celebrate the achievements, however big or small. Their positivity and constant support has helped me through tough times and motivated me to complete this tough journey. I would also like to thank all the other current and former students of the Cohen-Karni group, including Daniel, Nick, Atul, Elnatan, and Arjuna. I appreciate all their help in the lab, and their fruitful and insightful discussions that helped steer my research questions and goals in the right direction. I would especially like to acknowledge Atul for being patient while training me on various tools and processes when I first joined the group. The field of bioelectronics was completely new to me and his constant support and guidance

instilled a sense of confidence in me. I would like to thank all the undergraduate students, Gaurav, Nick, Gordon, Shivani, Stella and Chloe, who I had the pleasure of working with. Their eagerness to ask questions and learn constantly was a big source of inspiration for me. And as someone rightly said “teaching is a great way to keep learning”, I did in fact learn a lot while mentoring these brilliant students.

I would like to thank all my friends, the staff members and professors in the department of BME at CMU. Their positive attitude, friendly nature and eagerness to help each other makes this department really special and sets it apart from any other department or institute I have come across. They have not only helped me become a better scientist but also shaped the department tremendously and I am sure our department will touch new heights in the coming years.

I am thankful to all the friends I made in and outside CMU during my graduate life. Listing them all here will definitely take up many pages so I will skip that for now. A special acknowledgment to the amazing friends I met during my participation in the Indian Graduate Student Association (IGSA) events. They never let me feel home sick and have made a significant contribution to all the amazing memories I have made during my stay in Pittsburgh. Seeing them successfully graduate from MS and PhD programs was a great source of motivation for me too.

A special thanks to Neha, my pillar throughout the graduate program, for her constant presence, support and faith in me, especially during the times when I was low and frustrated. She never gave up on me and was one of the biggest reasons I could complete this journey successfully while keeping my sanity intact. I can’t thank her enough! Last but certainly not the least, my parents, grandparents, brother, uncles, aunts and all the cousins, a big thank you to all for keeping my motivation high by constantly praising my work and achievements. I would also like to

mention that the first and biggest motivation for me to even think of pursuing a Ph.D. was my dad, my idol, whom I've always looked up to. The incredible trust he has shown in me right from my childhood days has greatly influenced my personality and confidence. He is and will always be my superman!

ABSTRACT

Investigation and modulation of the electrical activity of neurons and cardiomyocytes is essential to understand the underlying mechanisms and treatment of neurological and cardiac diseases. Furthermore, having two-way interfaces with cells is crucial for brain-machine interfacing and engineering of more effective tissue regenerative scaffolds. Development of various optical and bioelectronics platforms over the decades has enabled probing of excitable cells to monitor and modulate their electrical activity. Ideally, the recording/stimulating platform should enable long-term stable interfaces and multi-site recordings/stimulation with sub-millisecond temporal and sub-cellular spatial resolution. Even though significant progress has been made, the current technologies are still limited on various fronts. Specifically, (i) patch clamp technique is limited by its recording sites, (ii) metal-based microelectrode array (MEA) are incapable to record at a single cell or sub-cellular level, (iii) high rigidity of Si-based probes lead to mechanical mismatch with the tissue thus impeding long-term stable interfaces, (iv) planar field effect transistors (FETs) are limited by the charge storage and injection capacities needed to stimulate cells, (v) voltage/ion sensitive dyes are limited in temporal resolution especially for volume measurements, and (vi) optogenetics is limited by the need of genetic modification of cells.

In this thesis work, the limitations of current techniques were addressed by developing platforms using an extraordinary carbon-based nanomaterial called graphene. Graphene's physical, chemical and electrical properties were tuned by tailoring its morphology and structure. The high transparency of two-dimensional planar graphene was leveraged to develop transparent MEA platform that enabled simultaneous optical and electrical recordings, thus integrating the high spatial and temporal advantages of both the techniques. The high surface area of out-of-plane grown three-dimensional (3D) graphene was leveraged to develop ultra-microelectrode arrays that

enabled recordings at sub-cellular spatial and sub-msec temporal resolutions. The high photo-absorbance and photo-thermal efficiency of nanowire-templated 3D graphene was leveraged to enable non-genetic photo-stimulation of neurons with high precision and sub-cellular spatial resolution. The tools developed in this thesis push the limits of the current technology which will further enhance our understanding of the tissue functioning both in healthy and disease states. Furthermore, it will enable development of better diagnostic and therapeutic platforms for both cardiac and neurological disorders.

TABLE OF CONTENTS

LIST OF FIGURES

LIST OF TABLES

Chapter 1- Introduction

"There is plenty of room at the bottom", a great lecture in 1959 by the Nobel Laureate, Richard Feynman, where he seeded the concepts of nanotechnology and introduced the ground breaking idea of developing molecular machines.[1] Since then, scientists and engineers have been exploring this concept and trying to develop nanomaterials with extraordinary properties using two approaches, i.e., bottom-up approach which refers to building up from molecules and nanostructures, and top-down approach, which refers to miniaturization of bulk materials and structures.[2-3] At the nanoscale, material properties are dominated by surface energy and surface properties which are different from those of bulk counterparts, thus enhancing their electronic, optical, magnetic, and structural properties that cannot be achieved at macro-scale.[4] Given that the functional elements and components in biology, such as nucleic acids, proteins, organelles, cell membrane, etc. are in nano- to micron-scale, development of nanomaterials has led to the possibility of probing, investigating and manipulating the biological processes.

1.1 Nanomaterials in biology and medicine

One of the important aspects of nanotechnology lies in the ability to tune materials such that their spatial and temporal scales are compatible with biomolecules. Nanomaterials are defined as materials with building units smaller than ca. 100 nm at least in one dimension.[5-6] Nanomaterials include nanoparticles, nanoclusters, nanotubes, nanofibers, nanowires, nanorods, two-dimensional (2D) sheets or films, etc., and can be made of metals, ceramics, polymers, organic materials and composites. Various top-down and bottom-up techniques such as electrospinning, phase separation, self-assembly processes, thin film deposition, chemical vapor deposition (CVD), chemical etching, nano-imprinting, photolithography, and electron beam lithography have been developed to synthesize nanomaterials and fabricate nanomaterial-based platforms.[5, 7-10] Scaling-

down the material size into the nanoscale significantly increases the surface area, surface roughness and surface area-to-volume ratios thus enhancing the physiochemical properties such as mechanical, electrical, optical, catalytic, magnetic properties, etc.[4, 11] The enhanced properties of nanomaterials in addition to their ability to interact with sub-cellular components make them a great candidate for various biomedical applications, such as bioactive scaffolds for tissue engineering,[5, 12] drug delivery for therapeutic applications,[13-14] and biosensors for diagnostics, investigation and modulation of cells and tissues.[15-17] However, there are two key points that are needed to be considered while applying nanotechnology in biology or medicine: first, the nanomaterials interfaced with cells or tissues should not interfere with the biological activities, and second, nanomaterials must be non-toxic.

1.2 Electrophysiology

The most complex network in the body, the nervous system, is made up of specialized cells called glia and neurons. Glial cells mechanically support the neural growth, form the immune system, supply nutrients to the neurons, and electrically isolate the neurons from each other.[18] Neurons are electrically excitable cells that relay information down a neuronal network in terms of electrical signals. The electrical signals, also referred to as action potentials, occur due to flow of certain ions such as Na^+ and K^+ across the cell membrane through the ion channels present in the cell membrane (Figure 1.1A).[18] At the resting state, the voltage-gated ion channels are closed. Since the resting membrane comprises of high number of leak channels specific to K^+ ions, the resting membrane potential (V_M) is around -85 mV to -60 mV, i.e., closer to the K^+ equilibrium potential. However, if an external stimulus or summation of multiple stimuli at the origin of the axon increases V_M above a threshold value of ca. -55 mV, it triggers the voltage gated Na^+ channels. When the channels open, Na^+ ions flow inside the cell and depolarize the cell, thus,

generating a positive intracellular potential change. The reversed V_M results in the closing of Na^+ channels and activation of the voltage gated K^+ channels. The outflow of K^+ ions repolarizes the cell which eventually crosses the resting V_M leading to hyperpolarization. The exchange of 3 intracellular Na^+ for 2 extracellular K^+ via Na^+-K^+ pumps, gets the cell back to its resting V_M. Once an action potential is initiated on a small section of the membrane, it triggers an action potential in the subsequent section, ensuring the signal propagation along the membrane. At the same time a transient negative shift due to the hyperpolarization prevents the backpropagation of the signal.[19] The amplitude of an action potential remains constant while traveling down the axon because the action potential is an all-or-none impulse that is regenerated at regular intervals along the axon.[19]

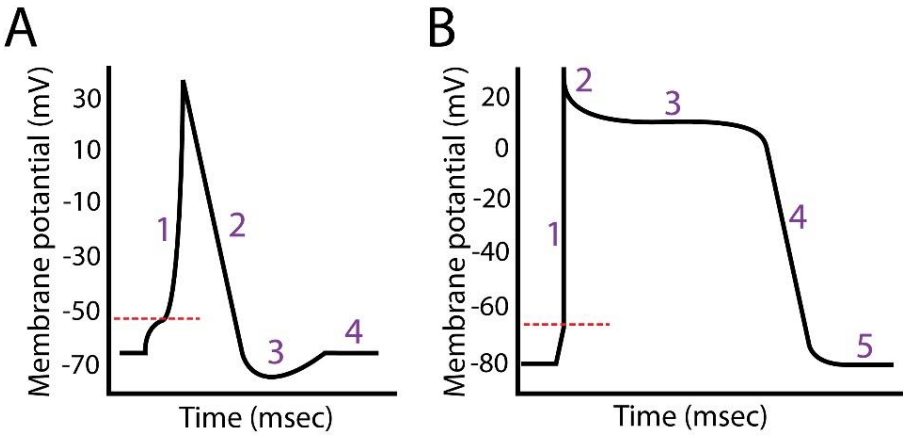

Figure 1.1 Schematic of an action potential.

(A) Action potential of a neuron. 1, 2, 3, and 4 denote depolarization due to Na^+ influx, repolarization due to K^+ outflux, hyperpolarization, and resting membrane potential, respectively. (B) Action potential of a cardiomyocyte. 1, 2, 3, 4, and 5 denote depolarization due to Na^+ influx, repolarization due to K^+ outflux, plateau phase due to Ca^{2+} influx, repolarization due to K^+ outflux and resting membrane potential, respectively. Dotted red line denotes the threshold potential to initiate an action potential.

The communication between neurons, also called neurotransmission, is accomplished either by the movement of chemicals across the chemical synapse or electrical signals across the gap junctions.[18] The frequency and pattern of the action potentials determine the functions of the neuronal networks. Another tissue in the body, heart, also consists of excitable cells called cardiomyocytes. These cells also have ion channels that enable flow of ions across the cell membrane thus leading to action potentials. However, one major difference between cardiac and neural action potential is the role of Ca^{2+} ions in depolarization of cardiomyocytes. The 1st two phases of action potential are similar to neurons, i.e., depolarization of the membrane due to Na^{+} influx and repolarization due to K^{+} outflux. However, during the repolarization, the voltage-gated Ca^{2+} channels get activated. The combination of K^{+} outflux and Ca^{2+} influx leads to the plateau phase as observed in Figure 1.1B. Once the voltage-gated Ca^{2+} channels close, outflux of K^{+} ions repolarizes the cell membrane. Cardiomyocytes are coupled by gap junctions allowing the movement of ions between cells to coordinate the action potential propagation and contraction across the heart.[20]

1.3 Investigation and modulation of electrical activity

Since the seminal works of Luigi Galvani, Kenneth Cole, Howard Curtis, Alan Hodgkin and Andrew Huxley in the 18th and 20th century that laid the foundation of the electrophysiology of excitable cells,[21-31] generations of investigators have invested immense efforts into developing tools for recording and modulating the electrical activity of neurons and cardiomyocytes. Characterizing the electrical signals has enabled understanding of the intracellular processes and intercellular communications crucial for the functioning of the heart and brain tissues.[16-17] Investigating electrical signals is crucial to understand pathophysiology, since most cardiac and neurological disorders are linked to impaired electrical activity at the cellular as well as tissue

level.[20, 32-33] In addition to fundamental research, pharmaceutical industries rely heavily on *in vitro* electrophysiological assay systems since the ion channels that are the basis of electrical activity serve as one of the major therapeutic drug targets.[16, 34-35] More recently, stimulation and recording of electrical activity has been explored for enabling brain-machine interfacing,[36] as well as tissue engineering applications for regeneration of cells and tissues.[37-39]

1.3.1 Current techniques and platforms

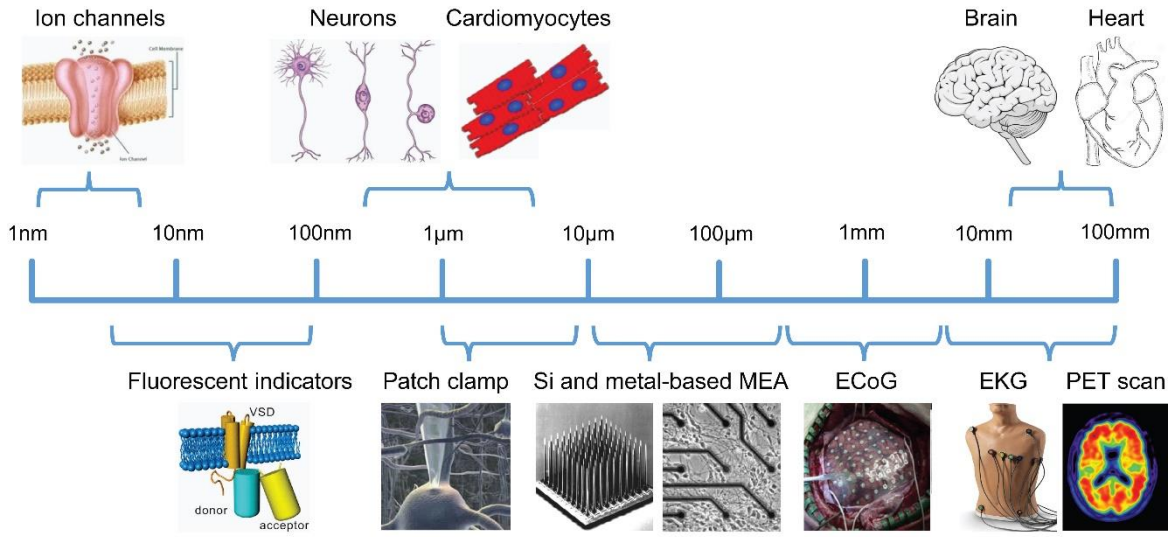

Figure 1.2 Comparing current imaging and bioelectronics platforms with the biological length scale.

Positron emission tomography (PET) and electrocorticography (ECoG) are specifically for monitoring brain activity, and electrocardiography (EKG) is specifically to monitor electrical activity of heart. The fluorescent indicators, patch clamp and microelectrode arrays (MEAs) are used for both neural and cardiac cells.

Development of patch-clamp technique in the late 20th century, that enabled electrical recordings at a sub-cellular scale with sub-msec temporal resolution, has played a crucial role in understanding the basic electrophysiology of excitable cells.[40] However, patch-clamp requires a

dedicated 3D manipulator for precise interfacing between a micropipette and cell membrane performed under a microscope, which impedes multiplexed recordings. Whole-cell patch clamping also leads to mixing of cell cytosol and the exogenous solution filling the pipette, which can lead to cell damage and complicate long-term measurements.[16, 41-42]

Over the years, many modalities have been developed to monitor and/or modulate the electrical activity of cellular networks and tissues (Figure 1.2), that can be categorized into three groups: First category includes neuroimaging approaches, such as functional magnetic resonance imaging (fMRI) and positron emission tomography (PET),[43-44] that allow noninvasive and long-term monitoring of brain activity. However, the detected signal represents a low bandwidth superimposition of the activity of large neuron populations leading to low spatiotemporal resolutions which limit the investigations and study of circuit dynamics at the cellular level.[44]

Second category includes optical imaging techniques, such as voltage and Ca^{2+}-based fluorescent indicators,[45] and optogenetics,[46] that use reporter chemicals or proteins that convert changes in membrane potential or flow of ions to an optical signal. These techniques enable recording and/or stimulation at sub-cellular as well as cellular network scale, however, they are limited by the penetration depth of light in the tissue, the toxicity of the fluorescent dyes, genetic incorporation of the proteins, or slow temporal-resolution in macroscopic 3D imaging.[45]

Third category includes the use of passive electrodes such as microelectrode arrays (MEAs) and active devices such as field effect transistors (FETs) (Figure 1.3). When an excitable cell is interfaced with an electrode or a transistor, a cleft is formed which generates a resistance called seal resistance or R_{Seal} as shown in Figure 1.3C, D. Excitation of the cell leads to the flow of ions across the cell membrane. This gives rise to an extracellular potential difference called

junctional voltage, V_J, with respect to the bath solution. When the electrode or transistor is interfaced with the cells, the V_J leads to changes in the recorded potential in the case of an electrode or changes in the recorded current in the case of a transistor, thus enabling recording of the cellular electrical activity.[16-17, 41]

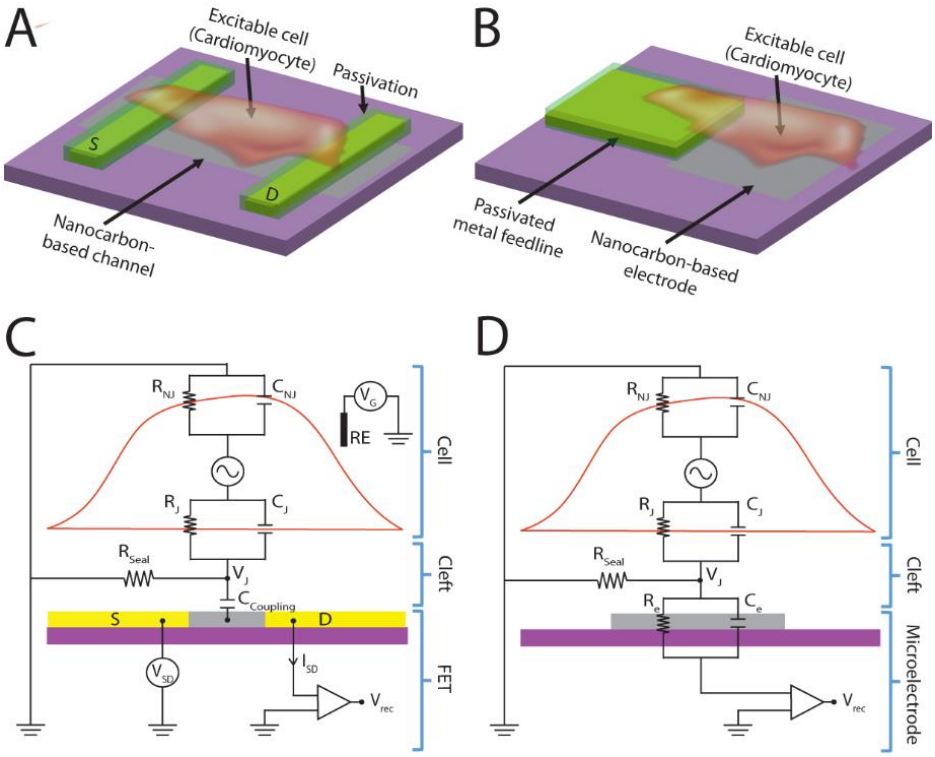

Figure 1.3 Cell-sensor interface.

Schematic illustrating the interface of excitable cells with (A) FET and (B) MEA. Electrical circuit analog of the (C) cell-FET and (D) cell-microelectrode interfaces. S and D represent source and drain leads, respectively. R_J, R_{NJ}, R_{Seal}, and R_e represent junctional, non-junctional, seal and electrode resistances, respectively. C_J, C_{NJ}, $C_{Coupling}$, and C_e represent junctional, non-junctional, coupling, and electrode capacitances, respectively. V_J, V_{SD}, V_G, V_{rec} and I_{SD} represent junctional voltage across the cleft, source-drain voltage, gate voltage, recorded voltage, and source-drain current, respectively. RE represents reference electrode.

The primary strength of this technique is the capability to achieve high temporal resolution that enables investigation of a wide range of phenomena, from the sub-msec spiking activity of individual cells to the slower network oscillations of small populations.[47-49] In addition, the passive electrodes can be used to inject charge to the cell thus stimulating the cells electrically. Furthermore, the quality of the recorded signals by electrodes can be improved by tuning certain design parameters that affect the impedance of the electrode and the seal of the sensor-cell interface, as per the equation:

$$\frac{V_e}{V_m} = \frac{Z_l}{Z_j + (\frac{Z_j}{R_{seal}} + 1)(Z_l + Z_e)}$$

where, V_e is the voltage detected by the electrode, V_m is the membrane potential, and Z_j, Z_l and Z_e are the junctional, load and electrode impedances, respectively.[16-17, 41, 50] MEAs and FET arrays allow for the simultaneous recording of signals from multiple excitable cells at multiple locations, thereby improving the understanding of signal propagation in a cellular network. However, typical metal-based MEAs, such as Au and Pt, and Si-based MEAs, such as Utah arrays, are limited by the presence of rigid materials with different mechanical properties from the biological tissue, leading to mechanical mismatch.[51-55] Furthermore, the poor biocompatibility of these electrodes' materials lead to chronic immune responses.[55-60] These factors lead to degradation of recording and stimulation capabilities over time.[51, 54, 58-59, 61-65] Furthermore, there is a trade-off between spatial resolution and sensitivity of MEAs since decreasing the geometric area of a recording site to a cellular or sub-cellular scale causes (i) a significant increase in the electrode impedance, Z_e, thus affecting the recording capabilities of the MEAs, and (ii) reduction in charge storage and injection capacities, thus affecting the stimulation capabilities of the MEAs.[66-70]

1.3.2 Factors for ideal platform and promise of nanomaterials

There are certain key factors that make a platform ideal for interfacing with excitable cells and tissues[16-17, 41, 70-71]: (i) high biocompatibility to avoid immune response and cell death, (ii) high flexibility to minimize mechanical mismatch and avoid shear motion at the cell-electrode interface, thus enabling long-term stable interfaces, (iii) multi-site recordings to enable investigation of cellular behavior at a network scale, (iv) high temporal resolution to allow recordings of sub-millisecond events, and (v) sub-cellular spatial resolution to enable high precision and accuracy, avoid averaging of signals from multiple cells, and enable investigation of sub-cellular events.

Nano-bioelectronics, an interdisciplinary field that combines nanomaterials and nanoscience with biology and electronics, offers the potential to overcome existing challenges faced by conventional platforms, such as low spatial resolution, low signal-to-noise ratio (SNR), poor specificity, and limited biocompatibility.[16-17, 72] Nanomaterials' high surface area-to-volume ratio and comparable size scale as that of biological building blocks offers possibility to interface, investigate and perturb biological processes from tissue scale down to sub-cellular scale.

In this thesis work, we addressed the above-mentioned limitations of the current techniques by developing platforms using an extraordinary carbon-based nanomaterial called graphene. By tailoring the morphology and structure of graphene we tuned its physical, chemical and electrical properties.[15, 73] The high transparency of 2D monolayer graphene was leveraged to develop transparent MEA platform.[15] This enabled simultaneous optical and electrical recordings, unlike standard metal/Si-based MEAs, thus integrating the high spatial and temporal advantages of both the techniques. The high surface area of out-of-plane grown 3D graphene was leveraged to develop ultra-microelectrode (UME) arrays with ~600 folds smaller geometric area of the electrodes compared to conventional MEAs, thus enabling recordings at sub-cellular spatial and sub-msec

temporal resolution. The high photo-absorbance and photo-thermal efficiency of nanowire-templated 3D graphene was leveraged to enable non-genetic photo-stimulation of neurons with high precision and sub-cellular spatial resolution. The tools developed in this thesis will further enhance our understanding of the tissue functioning both in healthy and disease states. Furthermore, it will enable development of better diagnostic and therapeutic platforms for both cardiac and neurological disorders.

1.4 Flow of thesis

This thesis is divided into 7 chapters: Chapter 1 focused on the brief introduction about the electrophysiology of excitable cells, investigation and modulation of electrical activity of excitable cells, current techniques and platforms, the nanotechnology and its usage in bioelectronics, and the ideal device parameters. Chapter 2 focuses on the synthesis and characterization of graphene-based nanomaterials with varying morphology, and physical, chemical and electrical properties. Chapter 3 focuses on investigation of the biocompatibility of graphene-based nanomaterials with both non-excitable and excitable cells. Chapter 4 focuses on the development of monolayer graphene-based transparent MEA platform to enable simultaneous electrical and optical recordings. Chapter 5 focuses on the development of 3D fuzzy graphene-based ultra-microelectrodes for electrical recordings at sub-millisecond temporal and sub-cellular spatial resolution. Chapter 6 focuses on development of a nanowire-templated 3D fuzzy graphene-based platform that enables non-genetic optical modulation of neurons at high spatial and temporal resolution. The final chapter summarizes all the other chapters and shines light on the future directions and further applications that can be pursued using the recording and stimulation platforms developed in this thesis work.

Chapter 2- Graphene-based nanomaterials

2.1 Introduction

Graphene is a one-atom thick 2D honeycombed arrangement of sp^2-hybridized C atoms. Since its discovery in 2004,[74] it has attracted considerable interest in the scientific community owing to its chemical stability,[75] high electrical conductivity (charge carrier mobility up-to 200000 $cm^2\ V^{-1}\ s^{-1}$),[76] mechanical robustness (Young's modulus of ca. 1 TPa),[77] high surface-to-volume ratio (theoretical value of ca. 2630 $m^2\ g^{-1}$),[78] and optical transparency (optical transmittance of ca. 97.7%).[79]

2.2 2D graphene

Over the years, different methods have been developed to obtain planar graphene, such as, (i) mechanical exfoliation, i.e. isolating monolayer graphene sheet from the highly ordered pyrolytic graphite (HOPG) using scotch tape;[74] (ii) chemical exfoliation, i.e. formation of graphene oxide (GO) suspension from graphite using Brodie, Staudenmaier, or Hummers method, followed by formation of thin films, and reduction of the GO to graphene using thermal, ultraviolet light or chemical methods;[80-82] (iii) epitaxial growth by thermal decomposition of SiC at 1200-1700 ºC under high vacuum;[83] and (iv) chemical vapor deposition (CVD), a surface-catalyzed process that decomposes C precursor gases such as CH_4, on transition metals such as Ni, Co, and Cu-based substrates at elevated temperatures of ca. 1000 °C either under ambient pressure (APCVD) or low pressure conditions (LPCVD).[84-86]

Graphene film produced by mechanical exfoliation is the cheapest way to produce high quality graphene, however, graphene production is labor intensive and not scalable, and the flake size is restricted to <1000 μm^2.[85] Chemical methods provide low-cost synthesis and fabrication of

large-scale films, however, these assembled graphene films show relatively inferior electrical conductivity owing to the poor interlayer junction contact resistance and the structural defects formed during the exfoliation and reduction processes.[84] Thermal decomposition of SiC yields relatively large graphene sheets on insulating substrates, however, it is not transferrable to other substrates, thus impeding the usage of graphene for flexible and transparent devices. CVD process, on the other hand, enables controlled synthesis of high-quality defect-free monolayer graphene. Furthermore, CVD synthesized graphene is transferrable to any substrate of interest using wet transfer and dry transfer techniques.[87-89]

2.2.1 CVD synthesis of monolayer graphene

We have optimized the synthesis of high-quality monolayer graphene using a custom-built LPCVD system. The quality of graphene sheet is determined by 3 major steps: (i) preparation of the growth substrate, (ii) synthesis of graphene via CVD process, and (iii) transfer of graphene to the desired substrate.

2.2.1.1 Substrate preparation

Cu foil was used as a growth catalyst because of its low solubility for C.[86] The as-purchased Cu foil has a native oxide layer on the surface which can hinder graphene growth.[90] The quality of Cu foil affects the graphene synthesis, therefore a pre-treatment of the foil is necessary. The foil is cut into desired dimensions and sonicated in acetone and isopropyl alcohol (IPA) to remove all the organic impurities from the surface. This is followed by HNO_3 acid treatment of the foil. 5.4% wt/wt HNO_3 acid treatment for 30 seconds was found to be most effective to clean the Cu foil without inducing any damage to the surface. After thoroughly rinsing the foil with deionized (DI) water and blow drying, it is introduced in the CVD system.

2.2.1.2 CVD synthesis

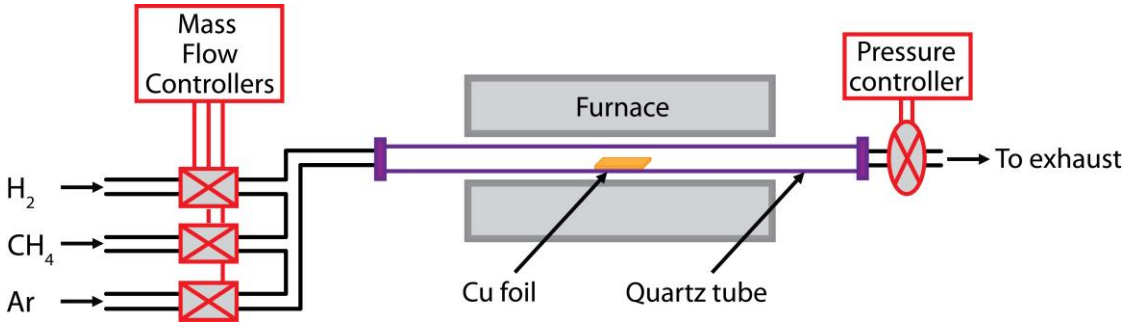

Figure 2.1 Schematic of the LPCVD system.

The quartz tube acts as a chamber for the substrate. The mass flow controllers, furnace and pressure controller regulate the gas flow rates, temperature and the pressure inside the chamber, respectively.

The foil is loaded in the quartz tube as shown in the Figure 2.1. The system is kept under vacuum to prevent environmental impurities to affect the foil and the synthesis process. The process occurs under the flow of CH_4 and H_2 over Cu substrate heated to a 1050 ^oC which is slightly below the melting point of Cu thus enabling adsorption of C atoms at the surface.[85] The low solubility of C in Cu restrains the growth of graphene to the surface of the catalyst, thus allowing formation of monolayer graphene. CH_4 acts as a C precursor gas whereas H_2 acts as a co-catalyst in formation of active surface bound C species (C_yH_x)s which is required for graphene growth.[91] H_2 also controls the grains shape and dimension.[91]

2.2.1.3 Graphene transfer

Transfer of CVD-grown graphene can be done either by wet transfer and dry transfer techniques.[87-89] Here we optimized the transfer of graphene using wet etch technique to both hydrophilic and hydrophobic substrates. The transfer process is illustrated in the Figure 2.2.

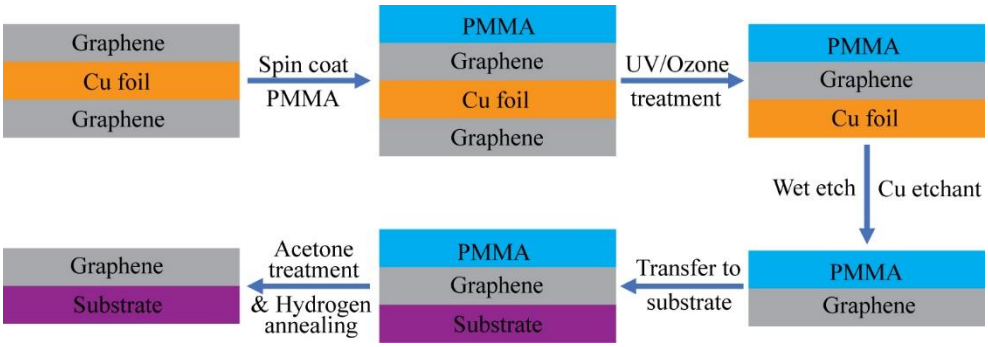

Figure 2.2 Schematic of graphene transfer process.

Monolayer graphene is synthesized by Cu-catalyzed LPCVD process and can be transferred to any substrate of interest using wet-transfer method.

During the LPCVD process, graphene is synthesized on both sides of the Cu foil, therefore to facilitate the transfer, graphene needs to be etched off from one side. Polymethylmethacrylate (PMMA) polymer is spin-coated on one side of the Cu to provide mechanical support and protect one of the graphene layers. Graphene on the other side is etched off using the UV/Ozone treatment. Post graphene etch, the PMMA-graphene-Cu foil stack is exposed to a $FeCl_3$-based Cu etchant. Once the Cu is etched, the PMMA-graphene stack is carefully transferred to clean DI water 3 times to remove traces of Cu etchant. The stack is then scooped onto the transfer substrate. Prior to this final transfer, the substrate is cleaned with acetone and IPA. In case of glass and Si/SiO_2 based substrates, we realized that UV/Ozone treatment leads to a smoother transfer with minimal tears. UV/Ozone treatment renders the surface hydrophilic which promotes spreading of water on the substrate leading to a smoother transfer. Furthermore, it enables the escape of water between the graphene-PMMA stack and the substrate during the drying step thus minimizing tears due to water evaporation. In case of polymer-based substrates that are sensitive to UV/Ozone treatment, such as SU8, we found that transferring the graphene-PMMA stack to IPA water mixture (1:3 IPA:water) followed by scooping on to the substrate led to a smoother transfer since IPA reduces

the surface tension and promotes wetting of the polymer-substrates. Post-transfer, the samples are dried overnight, followed by baking of the PMMA-graphene-substrate stack above the glass transition temperature (T_G) of PMMA. The baking step promotes adhesion of graphene on to the substrate and leads to conformal coating of PMMA on to the graphene thus minimizing cracks and tears during the final step of PMMA removal. The sample is then exposed to acetone to dissolve the PMMA layer. Finally, the samples are annealed at 300 ^oC for an hour in the reducing environment to get rid of any residual PMMA and enhance the substrate-graphene adhesion. (For more details about Cu preparation, graphene synthesis and transfer, see Appendix A).

2.2.2 Characterization of monolayer graphene

To characterize graphene film continuity and integrity, LPCVD synthesized graphene was transferred to a Si substrate with a 285 nm thick oxide layer (Si/285nm SiO_2), which provides optimal optical contrast for monolayer graphene imaging.[92] As evident from the DIC image, the synthesized graphene film is highly continuous with minimal observed tears (Figure 2.3A). To further validate the film quality, Raman spectra of graphene transferred on glass coverslip and Si/285 nm SiO_2 were acquired (Figure 2.3B, Table 1). The acquired spectrum exhibits a sharp G peak at ca. 1580 cm^{-1}, a symmetric 2D peak at ca. 2700 cm^{-1} with full width at half maximum (FWHM) of ca. 38 cm^{-1}, and no significant D peak at ca. 1350 cm^{-1}, indicating defect-free monolayer graphene.[93] This conclusion was further supported by measurement of ca. 97.7% transmittance, confirming high transparency and presence of mono-layer graphene[87] (Figure 2.3C). We note that the dip at 250 nm is observed due to the presence of benzene rings in the graphene sheet.[94] Since presence of surface impurities can have an adversely affect graphene's properties as well as biocompatibility, the fine microstructure and surface of the graphene films

were further investigated using scanning electron microscope (SEM).[95] The SEM characterization confirmed the absence of surface contaminants on the graphene film (Figure 2.3D).

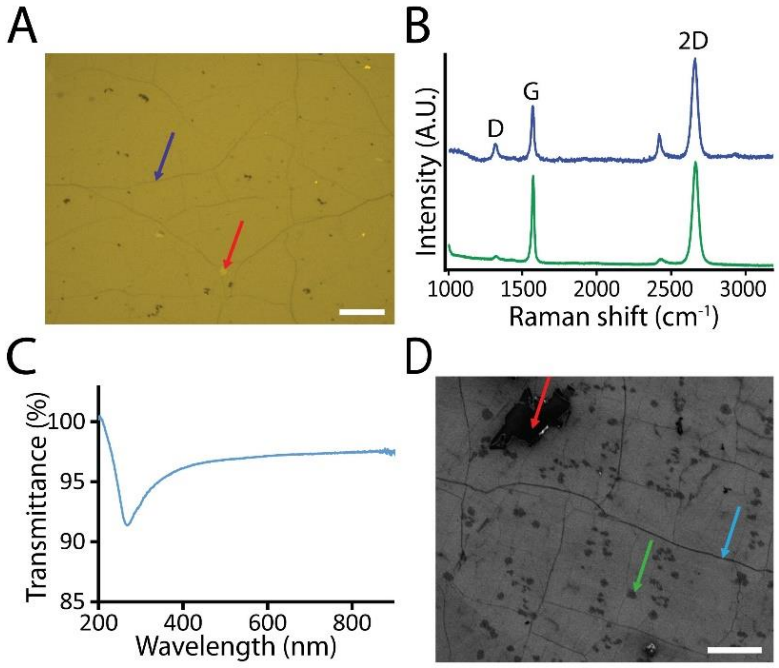

Figure 2.3 Characterization of graphene.

(A) Optical image of graphene transferred on Si/285 nm SiO_2 substrate. Purple and red arrows indicate grain boundary and a tear in the graphene film, respectively. Scale bar: 200 µm. **(B)** Raman spectra of graphene on glass cover slip (blue) and Si/285 nm SiO_2 substrate (green). **(C)** Transmittance of graphene transferred on a quartz substrate. **(D)** SEM image of graphene. Red, green and blue arrows indicate tear, nucleation point of second layer graphene and grain boundary, respectively. Scale bar: 15 µm.

The synthesis and transfer methods optimized in this work enables high quality defect-free monolayer graphene suitable for studying graphene-cell interactions and development of graphene-based bioelectronics.

2.3 3D graphene

High transparency of planar graphene makes it an attractive material for bioelectronics, however, the low available surface area due to its 2D planar structure limits its use as ultra-microelectrodes for sub-cell recordings and electrical stimulation. High surface area is crucial to enhance electrochemical activity, reduce the electrode impedance, and enhance the charge storage and injection capacities. Recently, 3D topology of graphene has been demonstrated by various approaches, including, synthesis of graphene or assembly of reduced graphene oxide (rGO) on nanoparticles followed by their organization in 3D,[96-99] synthesis of graphene on Ge nanowires (NWs),[100-101] synthesis of graphene on transition-metal foams,[102] and synthesis of 3D graphene hydrogels.[103] All these forms enhance the properties of graphene by increasing the surface area. However, in all these cases, the graphene flakes or films are lying flat, hence exposing a 2D surface topology thus limiting the advantages of extremely high surface area-to-volume ratio of graphene.

Another approach is to enable exposure of both sides of graphene, i.e., by out-of-plane growth of graphene. Out-of-plane graphene flakes have been synthesized using various methods, such as, thermal decomposition of SiC to synthesize large-area vertically aligned graphene sheets (VAGS),[104-105] and plasma-enhanced chemical vapor deposition (PECVD) for catalyst-free vertical growth of carbon nanowalls (CNWs).[106-108] Due to the out-of-plane morphology, the specific surface area of these materials is significantly higher as compared to planar graphene. However, the VAGS and CNWs are generally composed of few-to-dozens of graphene layers tethered to a 2D surface.

To further enhance the 3D morphology that leverages graphene's outstanding surface area-to-volume ratio, we developed a highly-controlled out-of-plane synthesis of single- to few-layer 3D fuzzy graphene (3DFG) on a 3D Si nanowire (SiNW) mesh template.[73] By varying SiNW and

graphene growth conditions, we can control the size and density of the NW-templated 3DFG (NT-3DFG), thus tuning the physical, electrical, electrochemical and optical properties of this hybrid nanomaterial.

2.3.1 Synthesis of nanowire-templated 3D fuzzy graphene (NT-3DFG)

Synthesis of NT-3DFG hybrid nanomaterial is a three-step process (Figure 2.4)[73]:

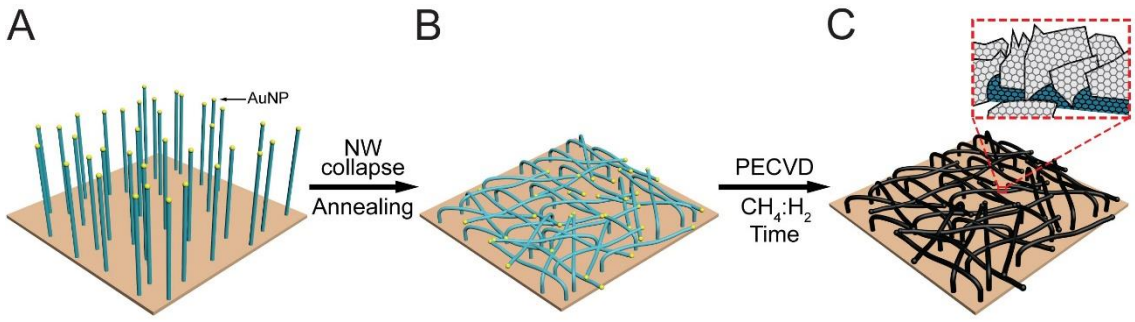

Figure 2.4 Synthesis process schematics of nanowire-templated growth of out-of-plane three-dimensional fuzzy graphene (NT-3DFG).

(A) NWs are synthesized by AuNPs catalyzed vapor-liquid-solid (VLS) process. **(B)** NWs are collapsed using liquid N_2 and annealed with H_2. **(C)** Out-of-plane 3DFG is synthesized on the NW mesh using plasma enhanced chemical vapor deposition (PECVD) process. Inset illustrates the growth of 3D fuzzy graphene flakes on a collapsed NW.

Briefly, SiNWs are synthesized by the Au nanoparticle catalyzed vapor-liquid-solid (VLS) process, followed by formation of an interconnected mesh by collapsing and annealing the SiNWs, and finally, synthesis of 3DFG on the SiNWs mesh through inductively coupled PECVD process.[73] Various synthesis conditions such as CH_4 partial pressure and PECVD process time were explored to demonstrate the tunability of the 3DFG flake size and density.[73] (For more details about NT-3DFG synthesis, see Appendix A).

2.3.2 Characterization of NT-3DFG

Structural characterization of NT-3DFG was performed using SEM, Transmission electron microscopy (TEM) and Raman spectroscopy, whereas electrical and electrochemical characterizations were done by sheet resistance and cyclic voltammetry measurements, respectively.

2.3.2.1 Structural characterization

The out-of-plane growth of 3DFG from the SiNW core was revealed by the SEM and TEM characterizations. Furthermore, the effect of varying PECVD conditions, i.e., CH_4 partial pressure and PECVD process time, on the growth of NT-3DFG was explored. Both SEM and TEM images revealed that increasing the CH_4 partial pressure from 22.7 mTorr to 25 mTorr, as well as increasing the synthesis time from 10 min to 30 min led to increase in the density and size of the graphene flakes (Figure 2.5).

The crystallinity of NT-3DFG was investigated using selected area electron diffraction (SAED). The diffraction patterns indicated that 3DFG is polycrystalline in nature (Figure 2.5B III(inset), Table 2).[109] The inter-planar distances for the 1st and 2nd nearest C-C neighbors were experimentally derived to be 0.119 nm and 0.205 nm. These values agree with the expected inter-planar spacing for the $(11\bar{2}0)$ plane ($d_{11\bar{2}0}$ = 0.123 nm) and the $(10\bar{1}0)$ plane ($d_{10\bar{1}0}$ = 0.213 nm). The distance between individual graphene layers (d_{0002} = 0.350 nm) concurs with the expected value of 0.344 nm indicating the presence of turbostratic graphene.[110-112].

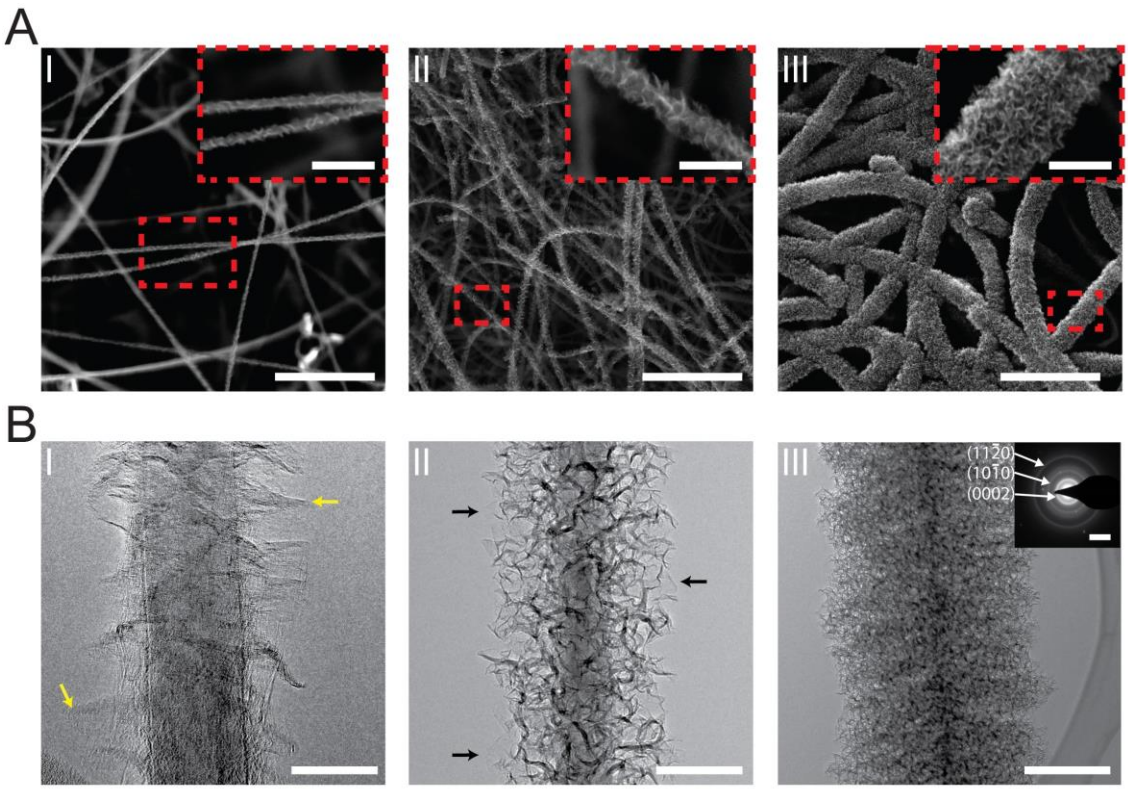

Figure 2.5 Effect of varying PECVD synthesis conditions on NT-3DFG growth.

(A) SEM images of NT-3DFG synthesized under the following conditions: **(I)** 22.7 mTorr CH_4 partial pressure for 10 min. Scale bars: 1 µm, 250 nm (inset); **(II)** 25.0 mTorr CH_4 partial pressure for 10 min. Scale bars: 2 µm, 250 nm (inset); and **(III)** 25.0 mTorr CH_4 partial pressure for 30 min. Scale bars: 2 µm, 250 nm (inset). **(B)** TEM images of NT-3DFG synthesized under: **(I)** 22.7 mTorr CH_4 partial pressure for 10 min. Scale bar: 30 nm; **(II)** 25.0 mTorr CH_4 partial pressure for 10 min. Scale bar: 10 nm; and **(III)** 25.0 mTorr CH_4 partial pressure for 30 min. Scale bar: 500 nm. Inset is a representative SAED pattern. Scale bar: 5 nm^{-1}.

3DFG structure was further investigated using Raman spectroscopy. The presence of characteristic peaks in the Raman spectra, i.e., D, G, and 2D peaks, confirmed the presence of graphene (Figure 2.6A, Table 3). The D and D' peaks are produced due to one-phonon defect-

assisted process, and D+D' peak is produced due to two-phonon defect-assisted process.[113] In the case of 3DFG, the emergence of the D peak, at ca. 1335 cm^{-1}, and the D' peak, as a shoulder to the G peak, is caused by breaks in translational symmetry due to the presence of 3DFG edges, as evident in the SEM and TEM images.[107, 113] The observed broad 2D peak can be fitted with a single Lorentzian, and explained by the presence of juxtaposed single- to few-layer graphene flakes, in the form of high-density 3DFG.[114-115]

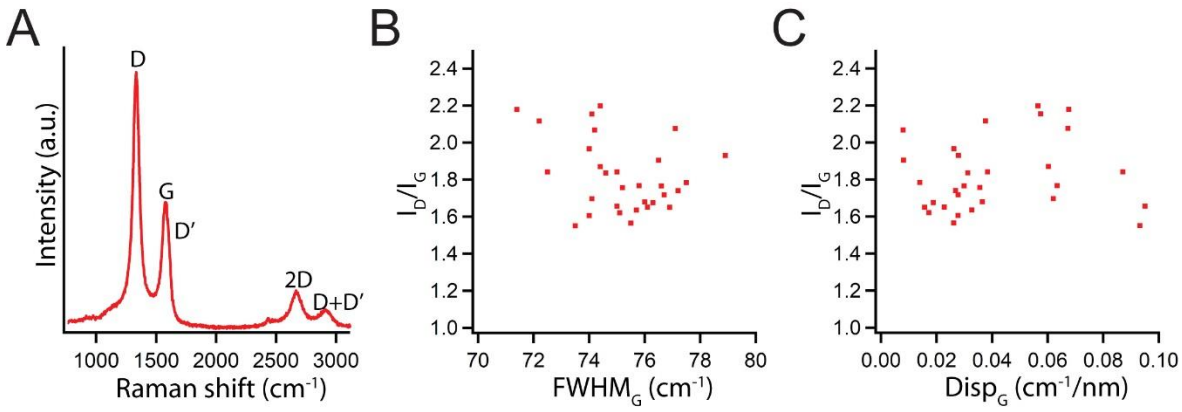

Figure 2.6 Raman spectroscopy of NT-3DFG.

(A) Representative Raman spectra of NT-3DFG synthesized under 25.0 mTorr CH_4 partial pressure for 30 min. Peak intensity ratio of D peak to G peak (I_D/I_G) as a function of **(B)** FWHM of G peak and **(C)** dispersion of G peak.

The appearance of a strong D peak due to edge effects was further verified by dual-wavelength Raman spectroscopy. Increase in both the position of the G peak as a function of excitation wavelength (Disp(G)) and G peak full width at half maximum (FWHM(G)) is observed with an increase in the disorder in the carbon structure.[116] Therefore, a higher I_D/I_G corresponds to higher Disp(G) and FWHM(G) in the case of bulk structural defects.[114-115] The lack of clear correlation between I_D/I_G and FWHM(G) as well as between I_D/I_G and Disp(G) (Figure 2.6B, C,

Table 4) further confirms that the major contribution to the D peak is due to edge defects rather than bulk-structural defects.[114-115, 117] The saturation of Disp(G) at 0.1 cm^{-1}/nm with change in excitation wavelength, is another indication of the presence of sp^2 hybridization and lack of large structural defects.[113-114, 116]

2.3.2.2 Electrical and electrochemical characterization

The electrical property of NT-3DFG was determined by characterizing the sheet resistance of NT-3DFG by the van der Pauw method.[118] The sheet resistance of NT-3DFG decreased with increasing CH_4 partial pressure and PECVD process time (Figure 2.7A). This change in the sheet resistance is attributed to the increasing density of single- to few-layer 3DFG flakes, which leads to the ability to sustain large current densities.[107] The sheet resistance for the 90 min PECVD process was as low as 84 ± 6 Ω $□^{-1}$ (conductivity of 1655 ± 450 S m^{-1}), significantly lower than other polycrystalline graphene films, 3D graphene nanostructures and 3D graphene composites.[119, 78, 102, 120-123] Furthermore, HNO_3 treatment, further reduced the sheet resistance of NT-3DFG to 59 ± 12 Ω $□^{-1}$, (conductivity of 2355 ± 785 S m^{-1}) by increasing carrier concentration.[124]

For electrochemical characterization, cyclic voltammetry measurements were performed in a three-electrode electrochemical cell configuration, with NT-3DFG as the working electrode, Ag/AgCl as the reference electrode and Pt wire as the counter electrode, in presence and absence of a redox probe $[Fe(CN)_6]^{3-}$ (Figure 2.7B, C). NT-3DFG performance was compared to the standard Au working electrode. The increase in the faradaic redox peak currents for NT-3DFG compared to planar Au working electrode (Figure 2.7B I) can be attributed to the increase in the electrochemically active surface area due to the presence of 3DFG.[125]

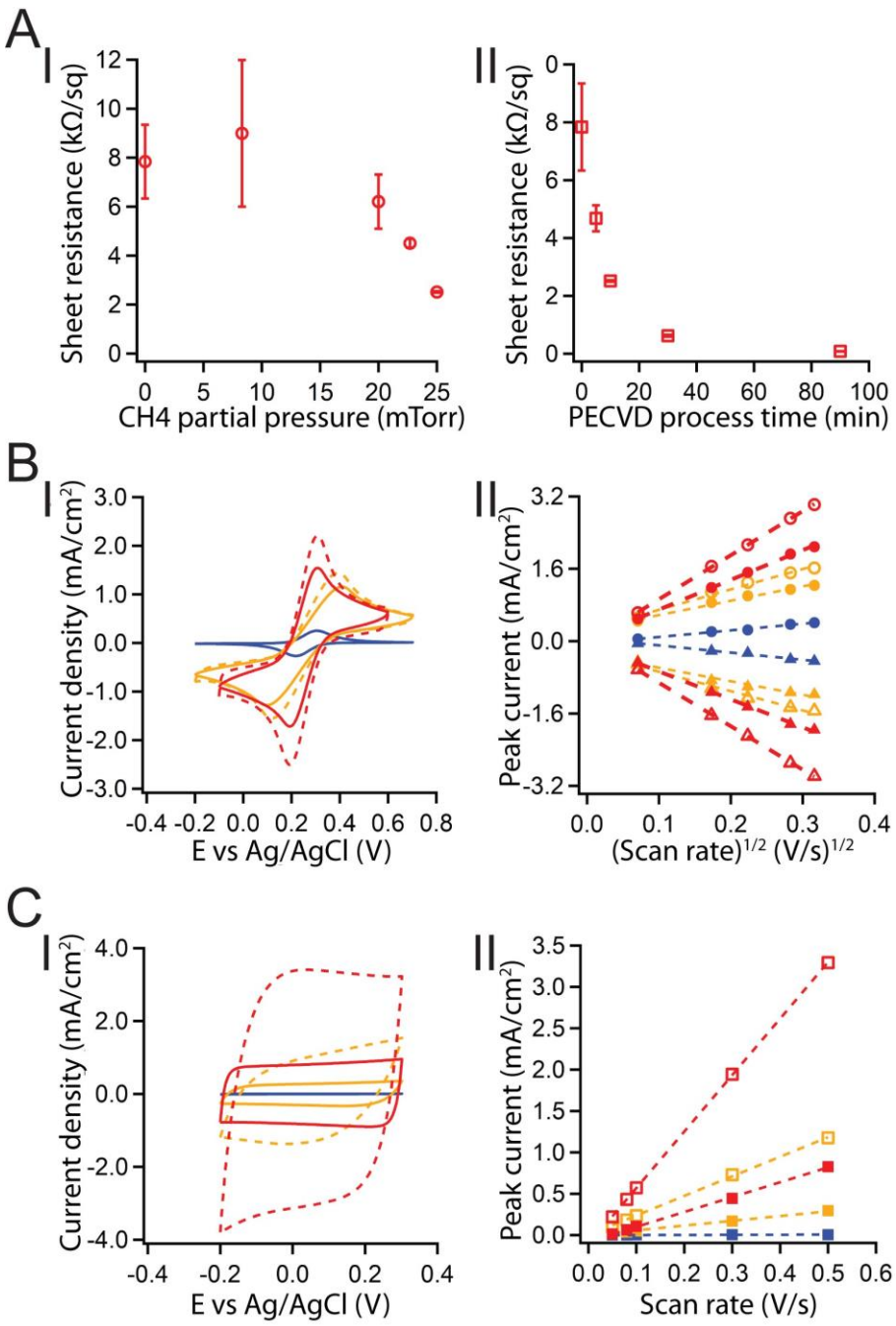

Figure 2.7 Electrical and electrochemical characterization of NT-3DFG.

(A) Sheet resistance of NT-3DFG synthesized under **(I)** varying CH_4 partial pressure for 10 min, and **(II)** under 25.0 mTorr CH_4 partial pressure with varying PECVD process times. **(B)** Cyclic voltammetry characterization. **(I)** Representative cyclic voltammograms (n=3) acquired with 5.00

Figure 2.7 continued: mM $[Fe(CN)_6]^{3-}$ in 1 M KCl at a scan rate of 50 mV s^{-1}. Blue, yellow and red colors denote Au working electrode, NT-3DFG synthesized under 25.0 mTorr CH_4 partial pressure for 30 min and 90 min, respectively. Dashed lines denote NT-3DFG after 2 hours of HNO_3 treatment. Inset presents the cyclic voltammetry setup with representative NT-3DFG working electrode (WE), Ag/AgCl reference electrode (RE) and Pt wire counter electrode (CE). **(II)** Peak current as a function of square root of scan rate (anodic and cathodic peak currents are denoted by circles and triangles, respectively). Closed and open circles-and-triangles denote NT-3DFG before and after 2 hours of HNO_3 treatment, respectively. **(C)** Double layer capacitance characterization. **(I)** Representative cyclic voltammograms (n=3) acquired with 1 M KCl at scan rate of 500 mV s^{-1}. Blue, yellow and red colors denote Au working electrode, NT-3DFG synthesized under 25.0 mTorr CH_4 partial pressure for 30 min and 90 min, respectively. Dashed lines denote NT-3DFG after 2 hours of HNO_3 treatment. **(II)** Current density as a function of scan rate. Blue, yellow and red colors denote Au working electrode, NT-3DFG synthesized under 25.0 mTorr CH_4 partial pressure for 30 min and 90 min, respectively. Closed and open squares denote NT-3DFG before and after 2 hours of HNO_3 treatment, respectively.

Treating NT-3DFG meshes with HNO_3 further increases the peak currents due to change in the surface wettability from super-hydrophobic to hydrophilic, thus increasing the accessible surface area. Both anodic and cathodic faradaic peak currents increase linearly with increasing square-root of scan rate and increasing $[Fe(CN)_6]^{3-}$ concentration (Figure 2.7B I). These results are in good agreement with the Randles-Sevčik model and establish that diffusion is the sole means of mass transport for NT-3DFG electrodes.[125] Increase in the slope of the peak current versus square root of scan rate curve further supports the increase in electrochemically active surface area (90 min NT-3DFG > 30 min NT-3DFG > Au) (Figure 2.7B II).[125] Faradaic peak separation for 90

min NT-3DFG (ca. 0.12 V) is smaller than that observed for 30 min NT-3DFG (ca. 0.30 V). This is attributed to faster electron transfer rates in 90 min NT-3DFG compared to 30 min NT-3DFG.[126]

To determine the double-layer capacitance, CV was performed in the 1 M KCl electrolyte solution. The double-layer capacitance was calculated as the change in current density with respect to the scan rate (Figure 2.7C).[127] The significantly higher capacitance of NT-3DFG (0.56 ± 0.01 mF cm^{-2} and 1.85 ± 0.02 mF cm^{-2} for 30 min and 90 min NT-3DFG, respectively) compared to that of Au working electrode (0.009 ± 0.001 mF cm^{-2}) can be explained by the remarkably high surface area of NT-3DFG (calculated specific electrochemical surface area of 117 ± 13 m^2 g^{-1} and 340 ± 42 m^2 g^{-1} for 30 min and 90 min NT-3DFG, respectively). HNO_3 treatment significantly increased the double-layer capacitance of NT-3DFG to 2.25 ± 0.07 mF cm^{-2} and 6.50 ± 0.10 mF cm^{-2} for 30 min and 90 min NT-3DFG, respectively, due to enhanced wettability and pseudocapacitance.[128] These values correspond to specific electrochemical surface area of 472 ± 53 m^2 g^{-1} and 1017 ± 127 m^2 g^{-1} for 30 min and 90 min NT-3DFG, respectively, significantly higher than other 3D carbon-based electrode materials such as graphene foam,[102] 3D macroporous chemically modified graphene electrodes,[120] graphene aerogel,[121] and carbon nanotube (CNT)-based platforms such as composites, graphene-SWCNT gels, films and electrodes.[123, 129-131]

2.4 Conclusions

This work demonstrated that graphene's properties can be further enhanced by developing hybrid nanomaterials and tailoring the morphology, size and density of the graphene flakes. The extremely high surface area, and outstanding electrical and electrochemical properties makes graphene a very promising candidate for tissue engineering, biosensors and bioelectronics applications, such as engineering of scaffolds for tissue regeneration, and development of devices for monitoring and modulating electrical and chemical activity of the cells.

Chapter 3- Biocompatibility of nanomaterials

3.1 Introduction

The outstanding and tunable properties of nanomaterials make them great candidates for a range of biomedical applications, including imaging, diagnostics, targeted drug delivery, biosensing etc. However, before these nanomaterials can be interfaced with the biological systems, one crucial parameter to consider and evaluate is their biocompatibility.

3.2 Toxicity of monolayer graphene

Since the discovery of planar monolayer graphene,[74] there has been an immense interest in its use for various applications including bio-interfaces due to its outstanding electrical conductivity (charge carrier mobility up to 200,000 $cm^2\ V^{-1}\ s^{-1}$), mechanical flexibility, and high transparency of up to 97.7%.[75, 132] Despite the outstanding properties, the prospective use of graphene in a biological context requires interaction of graphene with cells and tissues to be minimally toxic. The potential toxicity of graphene in biological systems has generated growing debate in recent years due to mixed findings.[133-134] In the case of cytotoxicity, hemolytic activity on red blood cells and generation of oxidative species in adherent skin fibroblasts due to graphene sheets was reported.[135] Cytotoxic effect of graphene on phaeochromocytoma (PC-12) cells was also demonstrated.[136] High toxicity of pristine graphene was also reported on monkey renal cells, macrophages and red blood cells due to high oxidative stress, which was averted by surface functionalization of graphene by carboxyl groups.[137-138] Modification and functionalization of graphene and its derivatives has been done to inhibit acute and chronic toxicity.[134, 139] On the contrary, there have been reports that suggest that graphene is biocompatible with fibroblast cells.[135, 140] Graphene was also found to promote growth, proliferation, and adhesion of

mammalian colorectal adenocarcinoma HT-29 cells, human osteoblasts, and mesenchymal stromal cells.[141-142] Graphene has also been shown to promote differentiation and growth of neurons.[143-145]

One of the major reasons behind mixed findings is the material preparation, i.e., the synthesis and the transfer processes of graphene. Graphene preparation can influence its physicochemical properties, such as size distribution (and lateral dimension), surface chemistry (i.e. surface functional groups and surface charge) and purity. These properties can affect the graphene-cell interactions.[95] Other factors that can explain the contradictory findings are: first, the type of assay used, e.g. the most commonly used viability assay, the MTT assay, has been shown to indicate a false biocompatibility as graphene reacted with MTT to form purple formazon, a result that would indicate viable cells even though there were no cells in this control sample;[135] and second, most of the studies focus on the viability assays, however, these assays are not sufficient indicators of cell health, i.e. whether the cell is under stress. The key limitation in previous studies is the lack of investigation of the graphene effect on cell stress using reliable and sensitive intracellular indicators under physiological conditions. We overcome this limitation by assessing the effect of graphene on cell stress using three highly sensitive indicators: mitochondrial membrane potential (MMP), mitochondrial morphology, and autophagy levels.

3.2.1 Effect of graphene on cell viability

To access graphene's toxicity, effect of monolayer graphene was accessed on the viability of monkey renal fibroblast (Cos-7), primary E18 rat hippocampal neurons, and human embryonic stem cells-derived cardiomyocytes (hESC-CM).[15, 132]

The monolayer graphene samples were synthesized using Cu catalyzed-low pressure chemical vapor deposition (LPCVD) process and were transferred to glass coverslips.

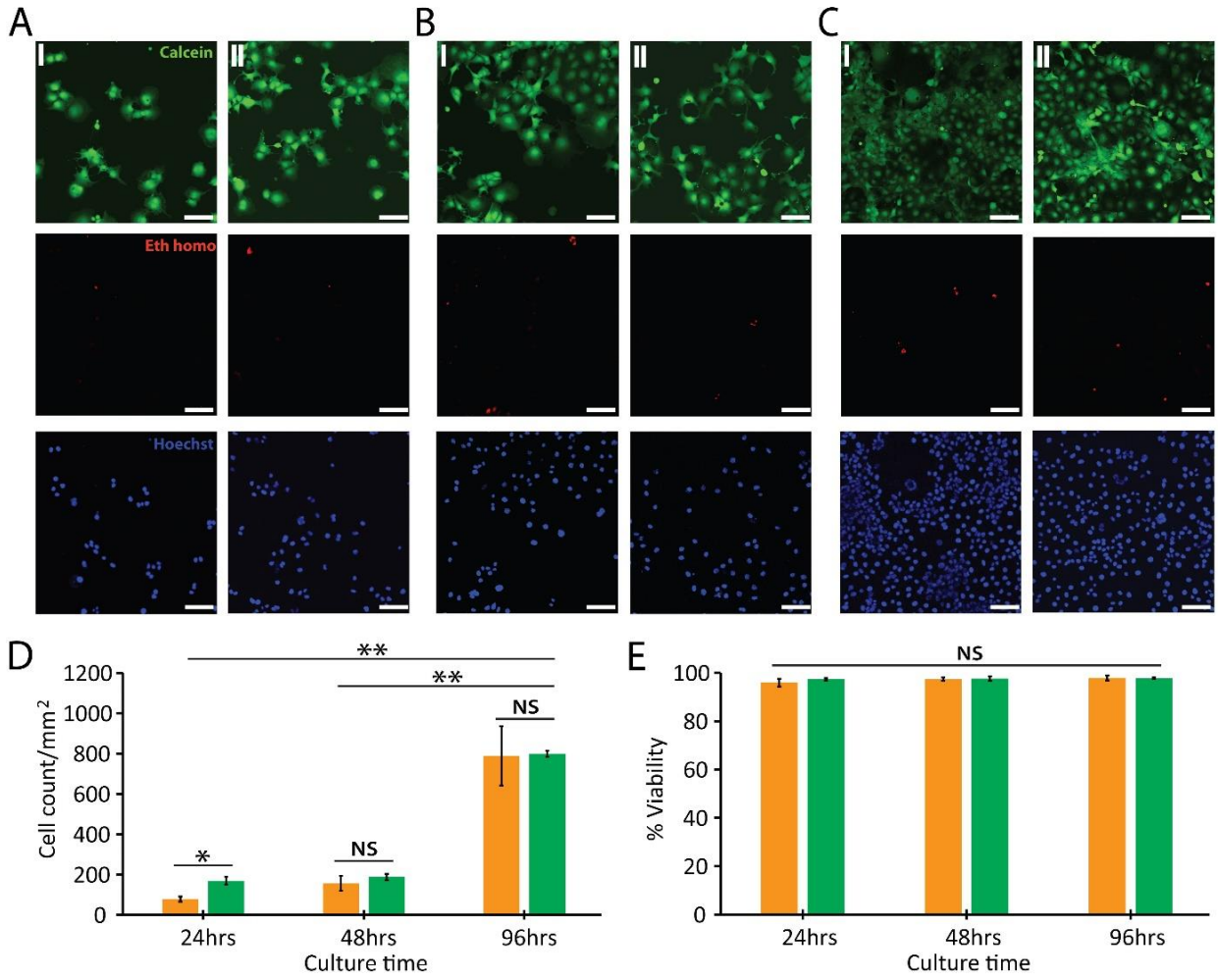

Figure 3.1 Effect of graphene on Cos-7 cells viability.

Live-dead assay performed on Cos-7 cells cultured for **(A)** 24 hr, **(B)** 48 hr and **(C)** 96 hr, on (I) glass and (II) graphene substrates. Green, red and blue denote live cells, dead cells and cell nuclei, respectively. Scale bars: 100 µm. Quantification of **(D)** cell number and **(E)** % viability of Cos-7 cells cultured on glass (orange) and graphene (green) substrates for 24, 48 and 96 hr, respectively. (*) and (**) denote statistically significant difference with $p<0.05$ and $p<0.005$, respectively. NS denotes no statistically significant difference. Results are presented as mean ± SD (n=4).

Optical, Raman and SEM characterizations were performed to check graphene's integrity, quality and absence of any impurities. Cellular viability was assessed by a calcein acetoxymethyl and ethidium homodimer based Live/Dead assay, which was preferred over the commonly used 3-(4,5-Dimethylthiazol-2-yl)-2,5-Diphenyltetrazolium Bromide (MTT) assay because graphene was previously shown to reduce MTT salt thus interfere with the assay results.[135]

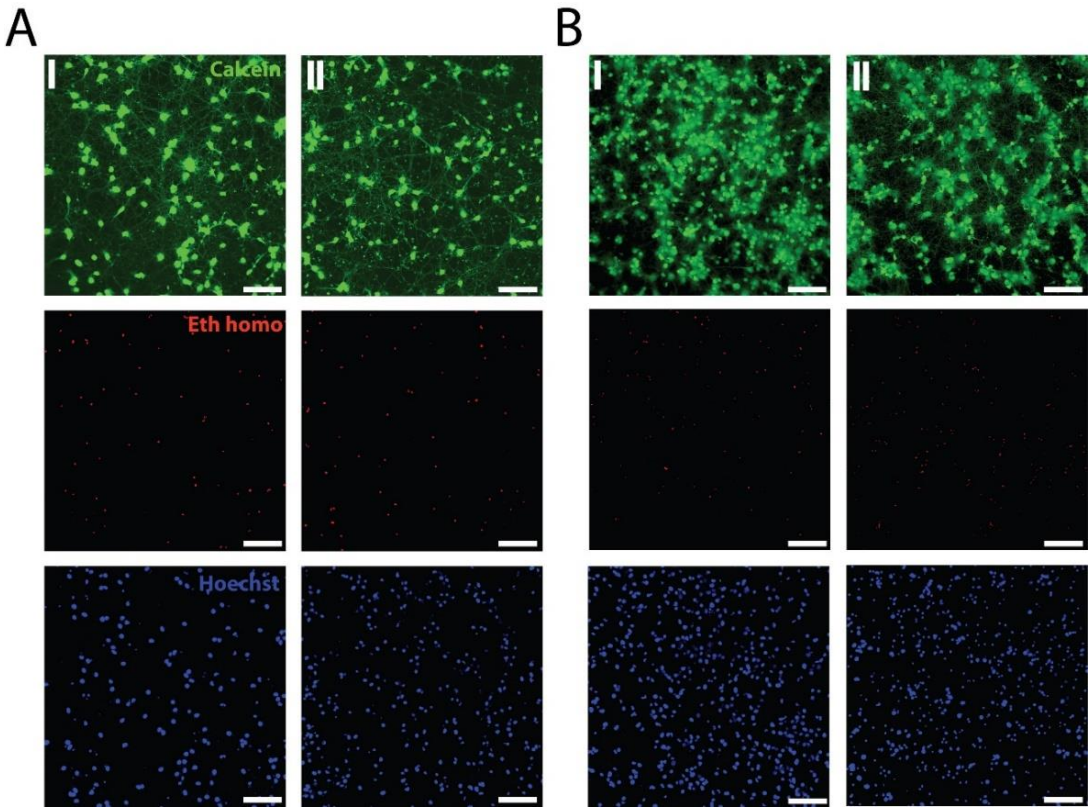

Figure 3.2 Effect of graphene on cultured hippocampal neurons viability.

Live-dead assay performed on neurons at **(A)** 6 DIV and **(B)** 9 DIV, cultured on **(I)** glass and **(II)** graphene substrates. Green, red and blue denote live cells, dead cells and cell nuclei, respectively. Scale bars: 100 µm.

Graphene substrates had no detectable cytotoxic effects on the cell viability as evident from the fluorescent images and the viability quantification of the Cos-7 cells (Figure 3.1). Graphene

substrates further promoted healthy proliferation and confluency of the Cos-7 cells (Figure 3.1D). After 24 hours of incubation, the cell count on graphene was seen to be significantly higher than on the glass cover slip ($p<0.05$). This can be attributed to high interaction of the fibroblasts secreted-ECM proteins with graphene due to hydrophobic interactions, therefore, promoting high cell adhesion with the underlying substrate.[146]

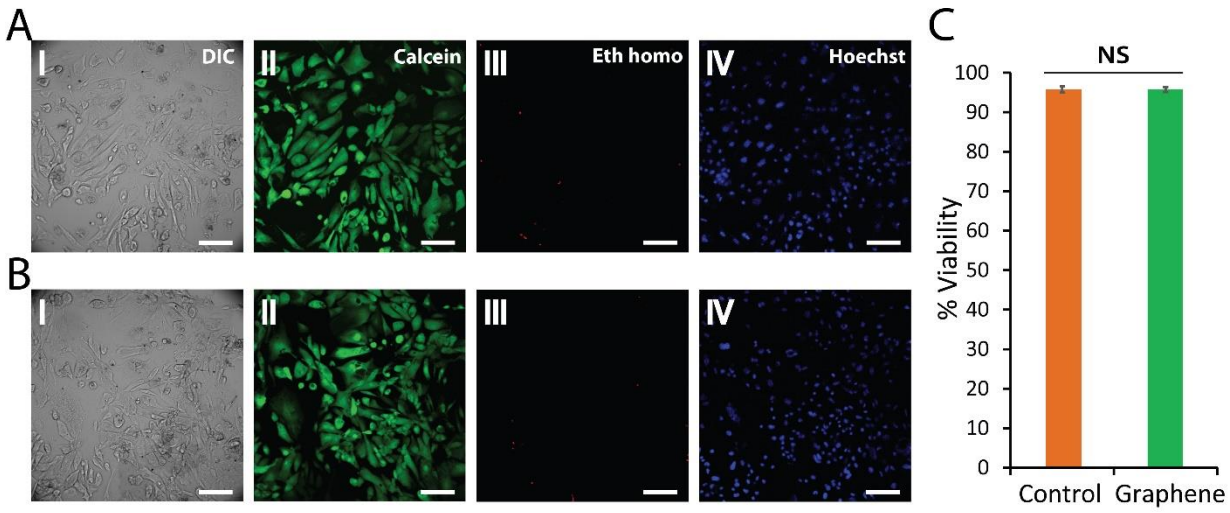

Figure 3.3 Effect of graphene on cardiomyocytes viability.

Live/Dead assay performed on hESC-CMs cultured on **(A)** glass control and **(B)** graphene substrates for 10 days. **(I)** represents DIC images, **(II-IV)** represent live cells, dead cells and cell nuclei, respectively. Scale bars: 100 μm. **(C)** Quantification of %viability of hESC-CMs cultured on glass (orange) and graphene (green) substrates. NS denotes no statistically significant difference. Results are presented as mean ± SD (n=3).

Effect of graphene on the viability of excitable cells, i.e., neurons (Figure 3.2) and human embryonic stem cells-derived cardiomyocytes (hESC-CMs) (Figure 3.3), was also assessed. No significant difference in the %viability of cells cultured on monolayer graphene vs glass control, confirmed biocompatibility of monolayer graphene.

3.2.2 Effect of graphene on cell stress- mitochondria

To further investigate the effect of graphene on cellular physiology and stress, the mitochondrial membrane potential (MMP) of both non-excitable and excitable cells was examined.

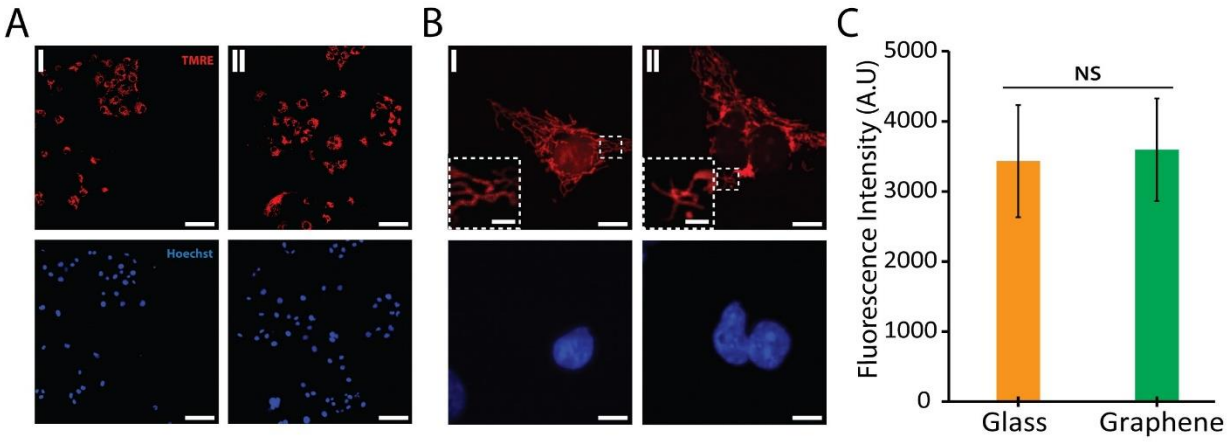

Figure 3.4 Effect of graphene on mitochondrial potential and morphology in Cos-7 cells. **(A-C)** TMRE assay performed on Cos-7 cells cultured on **(I)** glass and **(II)** graphene substrates. **(A)** Confocal images of the cells labelled with TMRE for mitochondria (red) and Hoechst for nuclei (blue). Scale bars: 100 µm. **(B)** High magnification single cell confocal images representing mitochondrial morphology. Insets: Expanded view of the marked white dashed area. Scale bars: 10 µm, 2.5 µm (insets). **(C)** Relative fluorescence readout of the TMRE-labeled cells cultured on glass (orange) and graphene (green) substrates. NS denotes no statistically significant difference. Results are presented as mean ± SD (n=3, 50 cells).

MMP plays an important role in maintaining the proton gradient across the mitochondrial membrane, which is essential for the electron transfer chain.[147] MMP is one of the most reliable and sensitive intracellular indicators of cell health or injury.[147] The depolarization of the mitochondrial membrane is one of the key events associated with cellular stress.[148] Disruptions of

the MMP may cause severe physiological consequences, including decrease in ATP synthesis, increase in reactive oxygen species generation, and the redistribution of pro-apoptotic mitochondrial factors leading to apoptosis of the cell.[148-149] Tetramethylrhodamine ethyl ester (TMRE) is a quantitative fluorescence marker for the activity of mitochondria.

The higher the concentration of dye inside the mitochondria, the higher the TMRE fluorescence. This fluorescence determines the actual MMP.[147] In normal cells, because of the electrochemical potential gradient, the dye concentrates in the mitochondrial matrix, where it forms red fluorescent aggregates as observed in the cells cultured on control substrates (Figure 3.4A 1). On inducing stress to the cells, the dye no longer accumulates in the mitochondria due to loss in membrane potential as observed in the cells treated with ethanol (Figure 3.5).

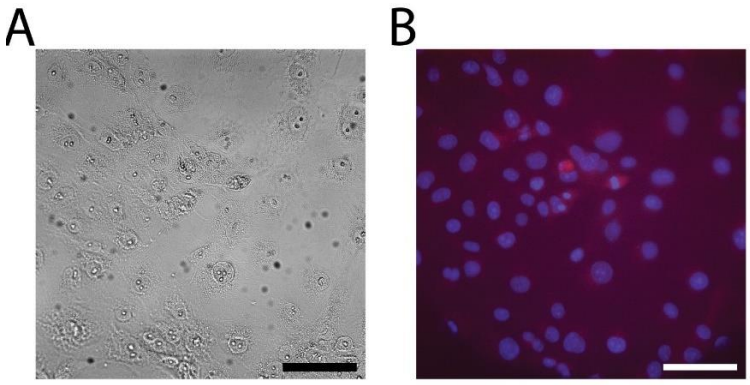

Figure 3.5 Loss of mitochondrial membrane potential in cells under stress.

(A) DIC and **(B)** fluorescence images of Cos-7 cells treated with ethanol. Scale bars: 100 µm.

No significant difference in the fluorescence intensity of TMRE dye in cells cultured on graphene as compared to cells cultured on glass (Figure 3.4), indicates that graphene does not affect the MMP. Similar observations were made for cultured hippocampal neurons (Figure 3.6), indicating that graphene does not induce stress in both neuronal and non-neuronal cells.

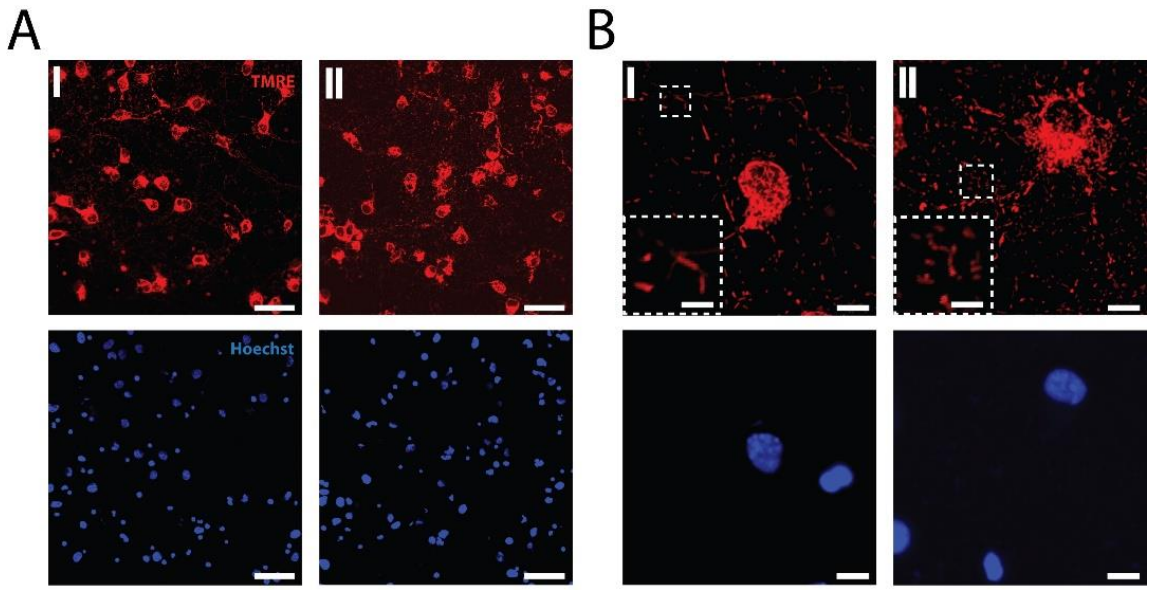

Figure 3.6 Effect of graphene on mitochondrial potential and morphology in neurons. TMRE assay performed on neurons at 6 DIV, cultured on **(I)** glass and **(II)** graphene substrates. **(A)** Confocal images of the cells labelled with TMRE for mitochondria (red) and Hoechst for nuclei (blue). Scale bars: 100 µm. **(B)** High magnification single cell confocal images representing mitochondrial morphology. Insets: Expanded view of the marked white dashed area. Scale bars: 10 µm, 2.5 µm (insets).

Mitochondrial morphology provides another reliable and sensitive indicator for cell stress. Decrease in connectivity and formation of short, round mitochondria are observed under conditions that compromise mitochondrial function.[150] These shifts from highly branched tubular to fragmented morphologies of mitochondria are regulated by the rates of fission and fusion events, which get disrupted when the cell is under stress.[150] The similar appearances of mitochondria with tubular morphology in the cells cultured on both glass and graphene substrates (Figure 3.4, Figure 3.6) further confirms that graphene does not induce cell stress.

3.2.3 Effect of graphene on cell stress-autophagy

To further examine the effect of graphene on cell stress, we checked the level of autophagy, a tightly regulated cellular pathway for the intracellular degradation of cytoplasmic organelles or cytosolic components. The level of autophagy provides another reliable and sensitive indicator of cell stress.[151]

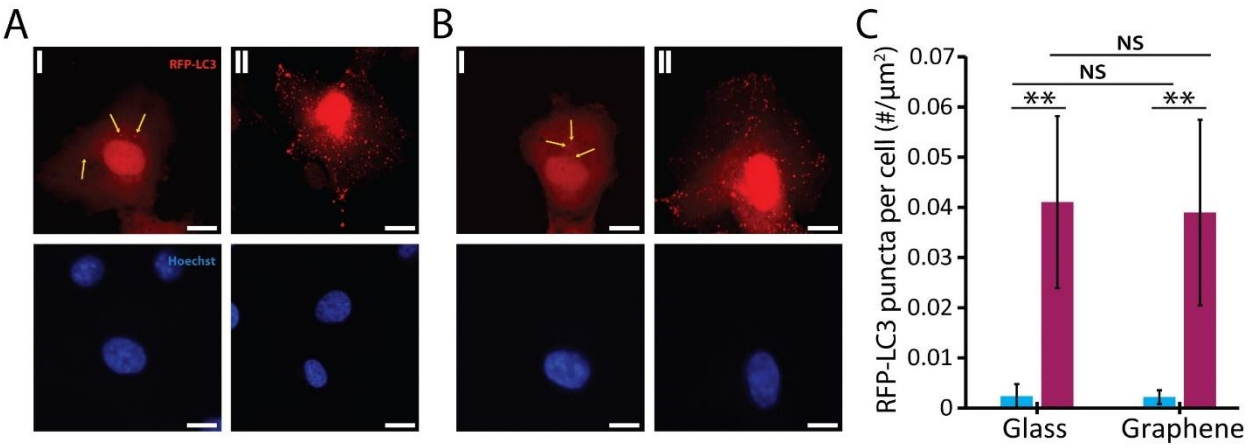

Figure 3.7 Effect of graphene on autophagy levels in Cos-7 cells.

High magnification single cell confocal images of the Cos-7 cells cultured on **(A)** glass and **(B)** graphene substrates labelled with RFP-LC3 for autophagosomes (red) and Hoechst for nuclei (blue), cultured in **(I)** presence of serum (i.e. normal) and **(II)** absence of serum (i.e. starvation) in the medium. Yellow arrows point to autophagosome puncta. Scale bars: 10 µm. **(C)** Relative RFP-LC3 puncta per cell normalized by the cell area for the cells cultured on glass and graphene substrates, under normal (cyan) and starvation (magenta) conditions. (**) denotes statistically significant difference with $p<0.005$. NS denotes no statistically significant difference. Results are presented as mean ± SD (n=4, 50 cells).

During autophagy, a cytosolic form of microtubule-associated protein 1 light chain 3 (LC3) called LC3-I, binds to phosphatidylethanolamine to form LC3-phosphatidylethanolamine

conjugate (LC3-II), which translocates rapidly to double-membraned vesicles called autophagosomes.[151] Therefore, fluorescently labelled-LC3 is commonly used as a marker of autophagosomes.[151-152] To determine the autophagy levels in the cells cultured on graphene, we transfected the cells with red fluorescent protein fused LC3 (RFP-LC3) plasmid DNA using electroporation.

Under normal conditions, RFP-LC3 has a diffused distribution throughout the nucleus and cytoplasm with small number of autophagosome punctae[153] as observed in the cells cultured on both glass cover slips and graphene (Figure 3.7A I, Figure 3.7B I). However, stress conditions, such as nutrient deprivation, induce high levels of autophagy which leads to a significant increase in autophagosome vesicles,[153] as observed in Figure 3.7A II, B II. To quantify the relative autophagy levels in the cells cultured under different conditions, we counted the autophagosome puncta per cell, as recommended in ref [153] (Figure 3.7C). The diffused RFP signals throughout the cytoplasm and nucleus with significantly low number of autophagosome puncta in the cells cultured on graphene substrates compared to cells under nutrient starvation ($p<0.005$), validates that graphene does not induce cell stress.

3.3 Effect of 3D graphene on cell viability and stress

Even though graphene has been shown to be biocompatible with both non-neuronal and neuronal cells, it is crucial to investigate the effects of out-of-plane graphene on cell behavior owing to the differences in physical properties of the nanomaterials. Previously, the presence of sharp edges in the vertical graphene-based substrate was demonstrated to damage the cell membrane of the bacteria upon direct contact thus leading to bacterial inactivation.[154] Therefore, to evaluate the toxicity of NT-3DFG on mammalian cells, hESC-CMs were interfaced with NT-3DFG meshes with different graphene flake sizes and densities for 7 days.

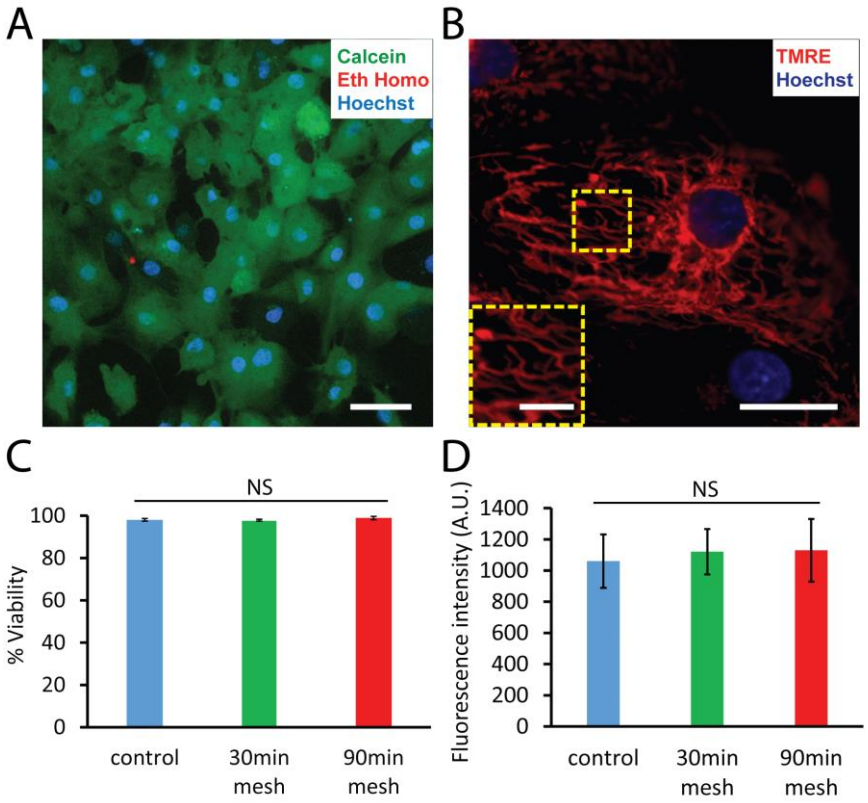

Figure 3.8 Effect of NT-3DFG on cell viability and stress of human embryonic stem cells derived cardiomyocytes.

(A) Live-dead assay performed on CMs cultured on NT-3DFG substrates. Green, red and blue denote live cells, dead cells and cell nuclei, respectively. Scale bar: 50 µm. **(B)** High magnification single cell confocal image of CM labelled with TMRE for mitochondria (red) and Hoechst for nuclei (blue). Inset: Expanded view of the marked white dashed area. Scale bars: 20 µm, 5 µm (inset). **(C)** % Viability and **(D)** Relative fluorescence readout of the TMRE-labeled cells cultured on glass (blue), 30min grown NT-3DFG substrates (green) and 90min grown NT-3DFG substrates (red). NS denotes no statistically significant difference. Results are presented as mean ± SD (n=3, 50 cells).

Live/dead assay was performed to investigate the effect on cell viability, and TMRE-based mitochondrial assay was performed to investigate the effect on cell stress. NT-3DFG did not have any negative effect on the cell viability as evident in the fluorescent images (Figure 3.8A) and % viability quantification (Figure 3.8C). The similar mitochondrial membrane potential and mitochondrial morphology in the cells cultured on different types of NT-3DFG meshes and glass control, confirmed that NT-3DFG does not induce cell stress (Figure 3.8B, D).

3.4 Conclusions

In conclusion, we have demonstrated that both monolayer graphene and 3D fuzzy graphene promote cell adhesion and cell proliferation of both non-excitable and excitable cells. In addition, graphene does not affect the MMP, the mitochondrial morphology, or the autophagy levels, indicating no detectable adverse effect on the cell stress. The cellular biocompatibility of graphene highlights the potential of graphene to be used in biomedical applications by providing long-term and stable cellular interfaces, especially in the field of bioelectronics to study neural and cardiac electrophysiology.

Chapter 4- Monolayer graphene-based transparent MEAs for electrical and optical recordings

4.1 Introduction

Recently, MEAs have been gaining tremendous popularity in the field of cardiac and neural electrophysiology because of their well-established microfabrication methods, consolidated transduction principle,[155] and the possibility to enable long-term and multi-site recordings at sub-msec temporal resolution.[41, 156] However, achieving high spatial resolution still remains a challenge since decreasing the geometric area of a recording site causes an increase in the impedance thus significantly reducing the SNR of the recorded signal.[66-70] Optical indicators, on the other hand, provide sub-cellular spatial resolution but are limited by the temporal resolution either due to kinetics of the chemical reporters or the standard acquisition systems, especially during investigation of a 3D tissue.[15-16, 41]

Complementing electrical recording with optical imaging using fluorescent indicators such as Ca^{2+} sensitive dyes can leverage the temporal resolution and spatial advantages of both the techniques. Commonly used metal based MEAs have high opacity which hinders simultaneous optical and electrical recordings. Previously, indium tin oxide (ITO)[157] and bilayer nanomesh[158]-based electrodes have been developed as transparent platforms, however, they are either limited by the brittle nature of the electrode material or limited transparency over a wide spectral range. Therefore, developing a platform that allows simultaneous electrical recordings and optical measurements over a wide visible spectral range will enable measurements at high spatial and temporal resolution, and will potentially enable optical stimulation of the cells at electrode-cell interface using optogenetics.[159]

The high transparency of up to 97.5% of monolayer graphene over a wide spectral range makes it a perfect candidate to develop transparent electrodes, thus allowing simultaneous electrical recordings and optical measurements.[15] Leveraging on graphene's high transparency, we have developed a graphene-based transparent and biocompatible platform to simultaneously perform Ca^{2+} imaging and electrical recordings in human embryonic stem cells derived cardiomyocytes (hESC-CMs).

4.2 Monolayer graphene MEA fabrication

The graphene based electrical and optical recording platform is illustrated in Figure 4.1.

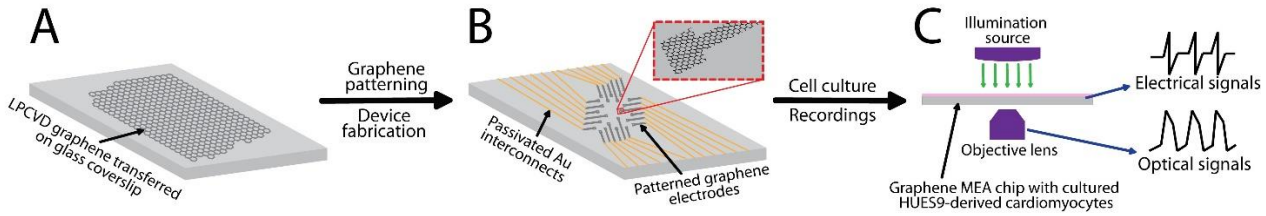

Figure 4.1 Schematics of graphene microelectrode array (MEA) fabrication and recording. **(A)** LPCVD synthesized monolayer graphene transferred on glass coverslip. **(B)** Fabricated graphene MEA. **(C)** Simultaneous optical and electrical recordings from human embryonic stem cells-derived cardiomyocytes (hESC-CMs) cultured on graphene MEA.

First, monolayer graphene was synthesized using low pressure chemical vapor deposition (LPCVD) and transferred to a glass coverslip or a Si/285nm SiO_2 substrate (Figure 4.1A). Second, the samples were annealed under reducing environment to enhance adhesion between graphene sheet and the substrate. Third, the devices were fabricated by top-down patterning of graphene sheet into electrodes with 50 µm x 50 µm recording sites, followed by patterning and evaporating Au interconnects, and passivating the Au interconnects and graphene lines with SU8 polymer (Figure 4.1B). For control, Au MEAs were fabricated with the same design and dimensions as the

graphene MEAs. Prior to passivation, graphene electrodes were treated with 69% HNO_3 acid for 2 h to enhance graphene's electrochemical properties. Fourth, the surfaces of the devices were coated with fibronectin, and the fibronectin-conditioned hESC-CMs were seeded on the devices. Finally, simultaneous electrical and optical recordings were obtained from the spontaneously beating hESC-CMs (Figure 4.1C). (For details regarding graphene MEA fabrication, and electrical and optical recordings from cells, please see Appendices C and D).

4.3 MEA characterization

The optical image confirmed high continuity of graphene film with minimal micro-tears (Figure 4.2A). The 32-electrode Au and graphene MEA devices were fabricated on both glass coverslips and Si/285nm SiO_2 substrates. Figure 4.2B shows an optical image of a graphene MEA fabricated on a glass coverslip, demonstrating the transparency of the center region with 32 graphene electrodes (cyan dashed box). The optical images of the graphene MEA fabricated on glass coverslip (Figure 4.2C, D), show the patterned passivated graphene electrodes.

The Raman spectra (Figure 4.2E) confirms the patterning of graphene electrodes with no damage to the film during the fabrication process, and the presence of a sharp G peak at 1590 ± 2 cm^{-1}, a symmetric 2D peak at 2690 ± 2 cm^{-1} with full width at half-maximum (fwhm) of 36 ± 4 cm^{-1}, and no significant D peak at 1364 ± 4 cm^{-1}, indicates presence of defect-free monolayer graphene. The presence of monolayer and high transparency of graphene was further confirmed by UV-vis spectroscopy that shows ca 97.7% transmittance (Figure 4.2F).[87] The dip in the transmittance spectra at 250 nm is observed due to the presence of benzene rings in the graphene sheet.[94]

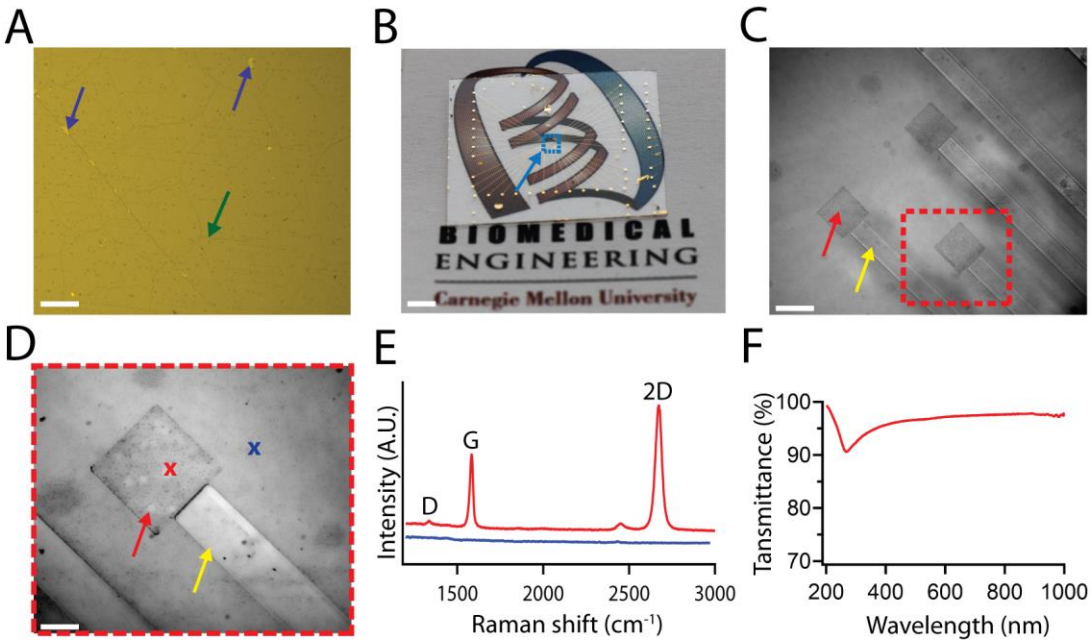

Figure 4.2 Characterization of graphene MEA.

(A) DIC image of LPCVD synthesized monolayer graphene transferred on Si/285 nm SiO_2 substrate. Purple and green arrows indicate tears and grain boundary in the graphene film, respectively. Scale bar: 100 µm. **(B)** Image of a graphene MEA fabricated on a glass coverslip. Cyan arrow marks the area with graphene electrodes (cyan dashed box). Scale bar: 2 mm. **(C)** DIC image of graphene electrodes fabricated on glass cover slip. Scale bar: 50 µm. **(D)** Expanded view of the marked red dashed box. Scale bar: 20 µm. Red and yellow arrows indicate exposed and passivated graphene, respectively. **(E)** Raman spectra acquired from graphene electrode (red) and non-electrode (blue) regions. **(F)** Representative transmittance spectra of monolayer graphene transferred to a quartz substrate.

To investigate the electrochemical properties of the electrodes, cyclic voltammetry (CV) and electrochemical impedance spectroscopy (EIS) characterizations were performed in a three-electrode electrochemical cell. To test the functionality of graphene electrodes, CV was performed at varying scan rates and compared to Au electrodes. A conductive electrode enables

electrochemical oxidation and reduction of a redox probe or analyte.[125] Absence of graphene electrodes resulted with no current recorded, indicating that the Au interconnects are properly passivated (Figure 4.3A, purple curve). The 50 µm x 50 µm graphene electrodes resolved the reduction and oxidation peaks of ferrocene methanol (FcMeOH) similar to that of Au electrodes indicating that graphene is electrochemically active (Figure 4.3A).[125]

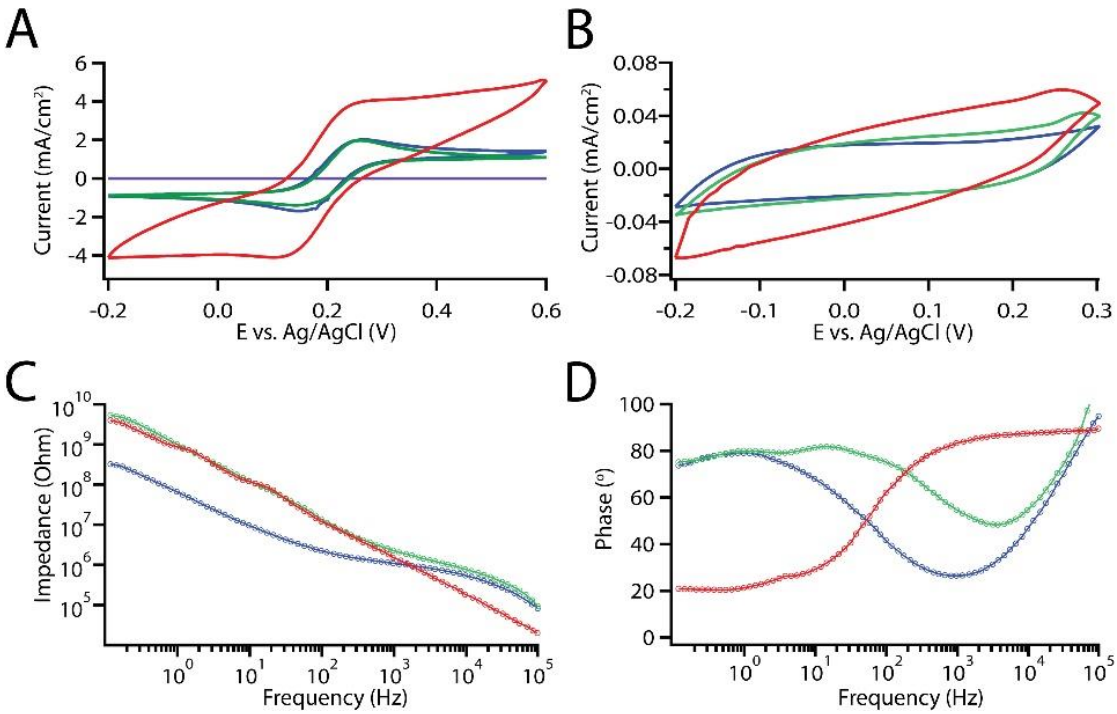

Figure 4.3 Electrochemical characterization of graphene MEAs.

(A) Cyclic voltammograms of 50 µm x 50 µm electrodes acquired with 5 mM FcMeOH in 1M KCl at 500 mV/s. **(B)** Cyclic voltammograms acquired with 1 M KCl at 800 mV/s. **(C)** Impedance versus frequency plots for 50 µm x 50 µm electrodes. **(D)** Phase versus frequency plots for 50 µm x 50 µm electrodes. Purple, green, blue and red traces denote no graphene control, graphene electrode, Au electrode, and HNO_3 treated graphene electrode, respectively.

Interfacing electrodes with the electrolyte leads to a formation of an electrical double layer that behaves as a capacitor.[125] Sweeping the potential across the working electrode with respect to the reference electrode leads to the capacitive currents, as observed for both graphene and Au electrodes (Figure 4.3B). Treatment of graphene with HNO_3 acid enhanced the faradaic and capacitive currents (Figure 4.3A, B) due to the increase in charge carriers and oxide containing species on the surface of graphene leading to pseudo-capacitance.[124, 128]

To further characterize the impedance of the electrodes EIS was performed. The Au and graphene electrodes showed impedances of 1.2 ± 0.2 MΩ and 2.1 ± 0.3 MΩ, respectively, measured at 1 kHz (Figure 4.3C). The impedance of the graphene electrodes dropped down to 1.5 ± 0.2 MΩ after HNO_3 acid treatment, comparable to the Au electrodes. This reduction in impedance can be explained by the increase in the charge carriers due to p-type doping introduced by HNO_3.[124] The phase plots indicate that Au electrodes exhibit more resistive characteristics at high frequencies and more capacitive characteristics at lower frequencies.[160] Graphene electrodes show a deviation in the capacitive properties compared to Au electrodes which might be attributed to quantum capacitance of graphene.[161-162] The HNO_3 acid treatment enhanced the capacitive characteristics of graphene, which is in line with the increase in capacitive currents in the CV curves performed with 1M KCl.

4.4 Optical and Electrical recordings

The Au and graphene electrodes were then interfaced with hESC-CMs for simultaneous electrical and Ca^{2+} imaging. The cells cultured on the MEA chips spread out uniformly as evident by the immunofluorescent and DIC images (Figure 4.4). The immunostaining of alpha-actinin bands confirms the presence of CMs.[163]

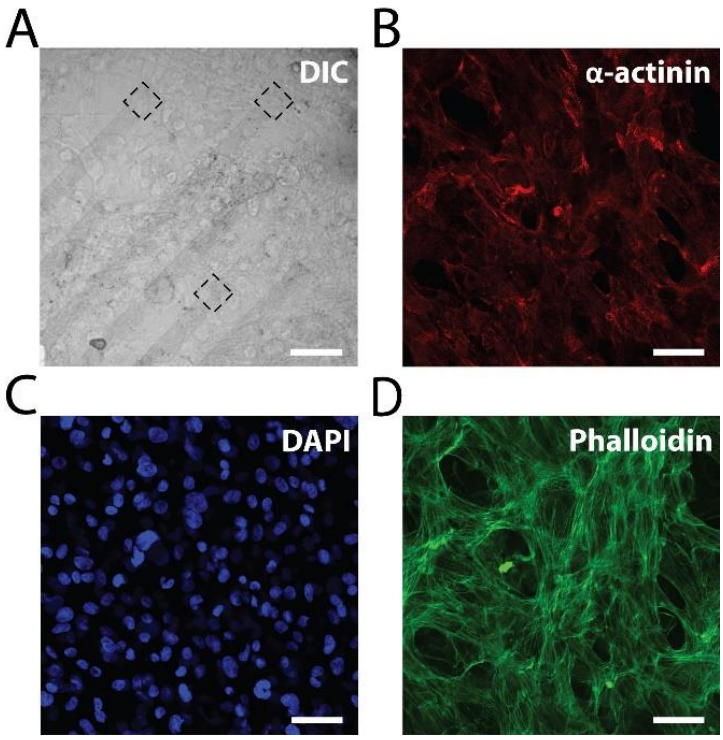

Figure 4.4 Immunofluorescence of hESC-CMs on graphene MEA.

(A) DIC image of hESC-CMs cultured on graphene MEA. The dashed black boxes denote graphene electrodes. Scale bar: 100 µm. **(B-D)** Confocal images of hESC-CMs cultured on graphene MEA. Red, blue and green channels represent α-actinin, nucleus and actin, respectively. Scale bars: 100 µm.

Both Au and graphene-based electrodes recorded the field potentials with spike frequency of 1.1-1.4 Hz at high SNR of >14 (Figure 4.5A, B). The high temporal resolution of the electrical recordings provides information about the Na^+ current (upstroke), K^+ current (repolarization) and Ca^{2+} current (plateau phase) across the cell membrane with recorded field potential amplitude (FPA) of 815 ± 12 µV and FPD of 217 ± 9 ms (n=70 peaks) (Figure 4.5A III, B III). The values for beating frequency, field potential duration (FPD) and FPA are in line with the previously reported values.[157, 164-165]

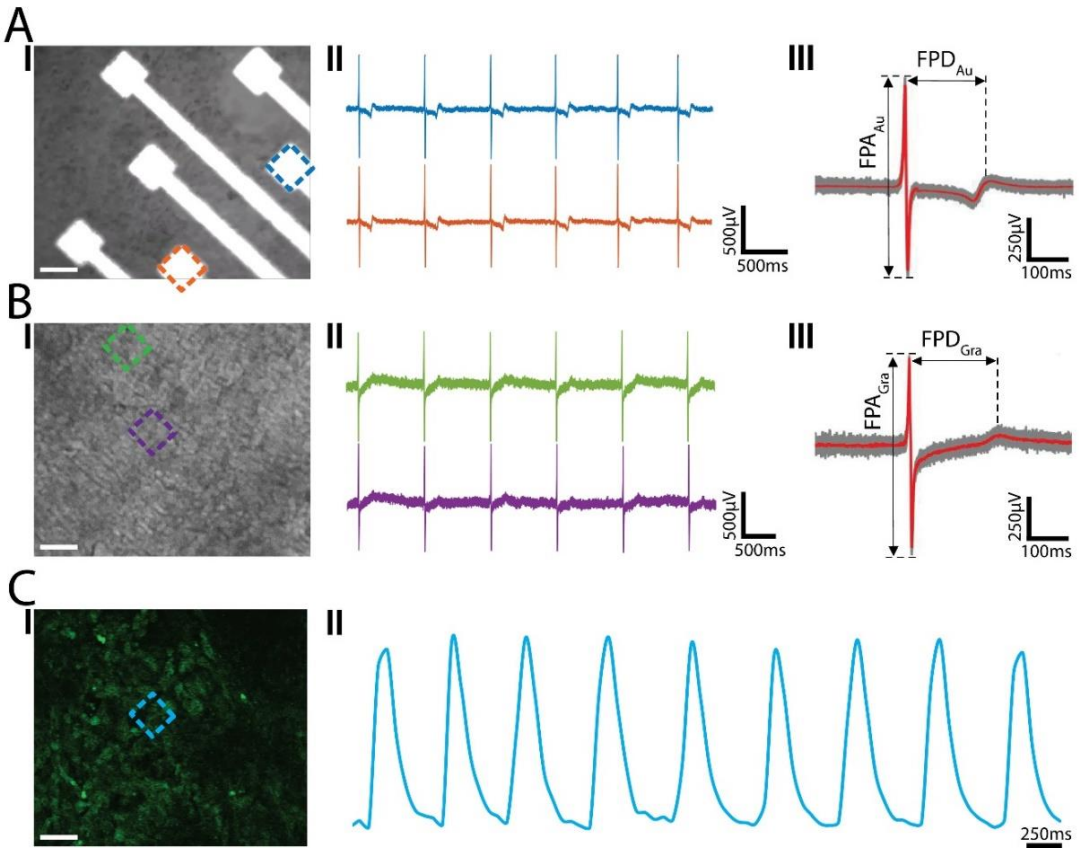

Figure 4.5 Electrical and optical recordings using graphene MEA.

(A) Electrical recordings using Au MEA. **(I)** Optical image of hESC-CMs cultured on Au MEA. Scale bar: 50 µm. **(II)** Representative recorded field potential traces using Au electrodes marked in (I). **(III)** Averaged peak (red trace) and raw data (grey traces, 87 peaks). **(B)** Electrical recordings using graphene MEA. **(I)** Optical image of hESC-CMs cultured on graphene MEA. Scale bar: 50 µm. **(II)** Representative recorded field potential traces using graphene electrodes marked in (I). **(III)** Averaged peak (red trace) and raw data (grey traces, 70 peaks). FPA and FPD denote field potential amplitude and field potential duration, respectively. **(C)** Ca^{2+} fluorescence signal recordings. **(I)** Confocal image of hESC-CMs loaded with Fluo-4 dye, cultured on graphene electrodes. Scale bar: 50 µm. **(II)** Fluorescence intensity as function of time at the electrode region marked in (I).

As evident from the fluorescent imaging, high opacity of the Au microelectrodes hinders the imaging of the cells interfaced with the electrodes (Figure 4.5, Figure 4.6).

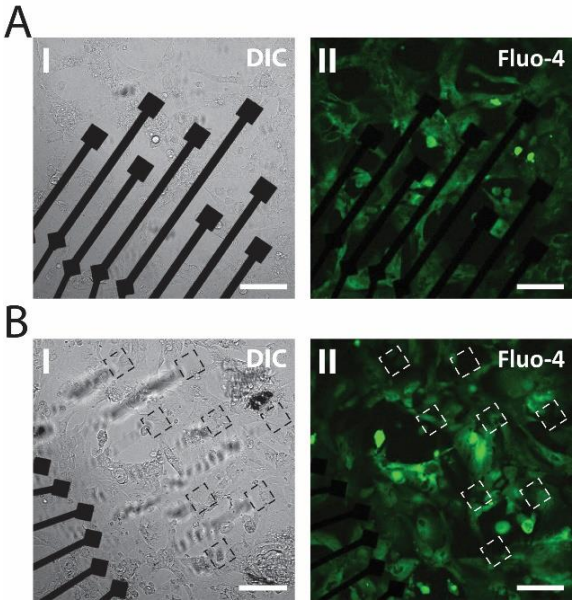

Figure 4.6 Ca^{2+} imaging of hESC-CMs through Au and graphene MEAs.

(I) DIC and (II) confocal images of Fluo-4 loaded cells cultured on **(A)** Au MEA and **(B)** graphene MEA. The dashed boxes in (B) denote graphene electrodes. Scale bars: 100 µm.

The high transparency of graphene electrodes enabled simultaneous Ca^{2+} imaging from the cells at the cell-electrode interface (Figure 4.5C). The Ca^{2+} spike frequency extracted from the time lapse imaging of Ca^{2+} sensitive dye (Fluo-4) labeled cells matches the electrical spike frequency recorded using the electrodes. This shows the ease of performing simultaneous recordings, thus allowing integration of the advantages of both modes of recording, leading to high spatial and temporal resolution.

4.4.1 Graphene MEA for investigating the effect of drugs on cardiomyocytes

To further validate the recorded electrical signals and check if graphene MEA platform can be used to detect changes in electrophysiology, the cells were treated with a standard drug,

isoproterenol that stimulates the β-adrenergic receptors leading to an increase in beat frequency and a decrease in FPD.[166]

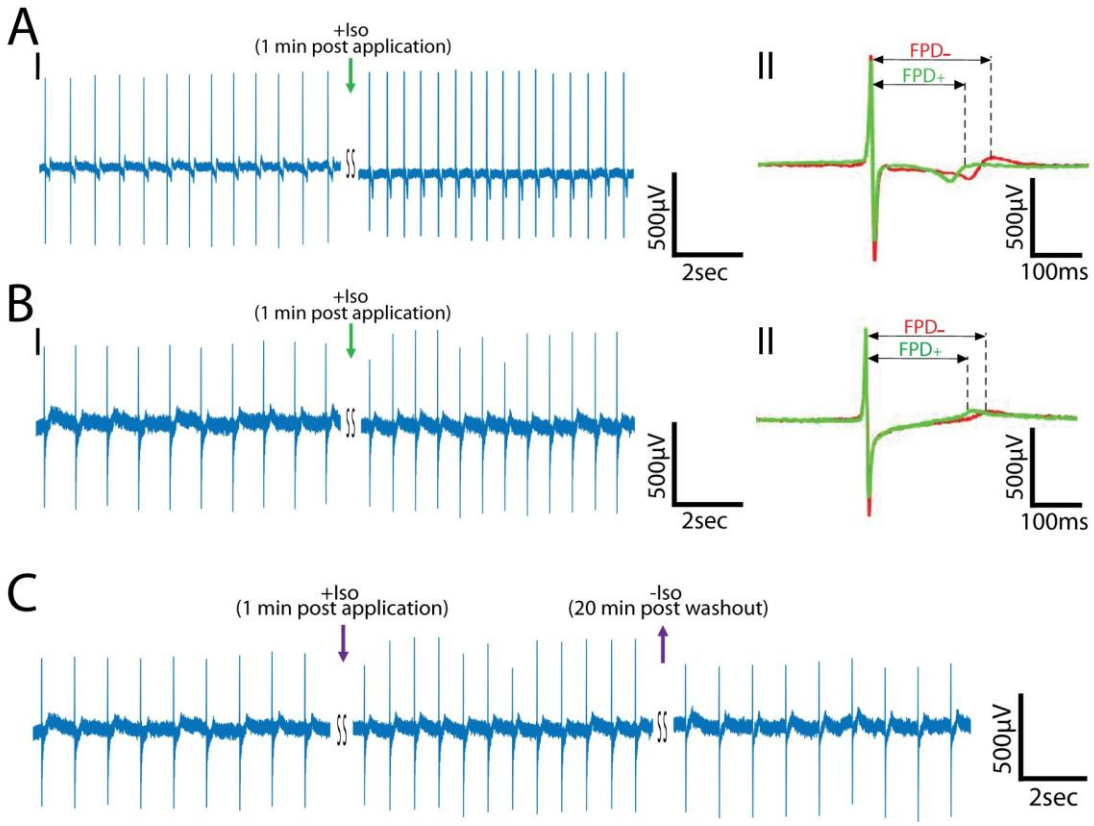

Figure 4.7 Effect of β-adrenergic receptor agonist on recorded electrical signals.

(A) Representative recorded field potential using Au MEA. **(I)** Trace before and after application of the β-adrenergic receptor agonist, isoproterenol. **(II)** Averaged trace (87 peaks) before (red) and after (green) isoproterenol application. **(B)** Representative recorded field potential using graphene MEA. **(I)** Trace before and after application of isoproterenol. **(II)** Averaged trace (70 peaks) before (red) and after (green) isoproterenol application. **(C)** Representative recorded field potential trace using graphene electrode showing reversibility of drug effect. Arrows denote addition and washout of isoproterenol.

A 1.3 fold increase in the peak frequency from 1.4 Hz to 1.8 Hz in case of Au electrodes, and 1.2 fold increase from 1.1 Hz to 1.3 Hz in case of graphene electrodes was observed post drug treatment (Figure 4.7A I, B I). The beat frequency returned to its original value post washout of isoproterenol (Figure 4.7C), suggesting feasibility of performing multiple assays on the same electrode-cell setup.

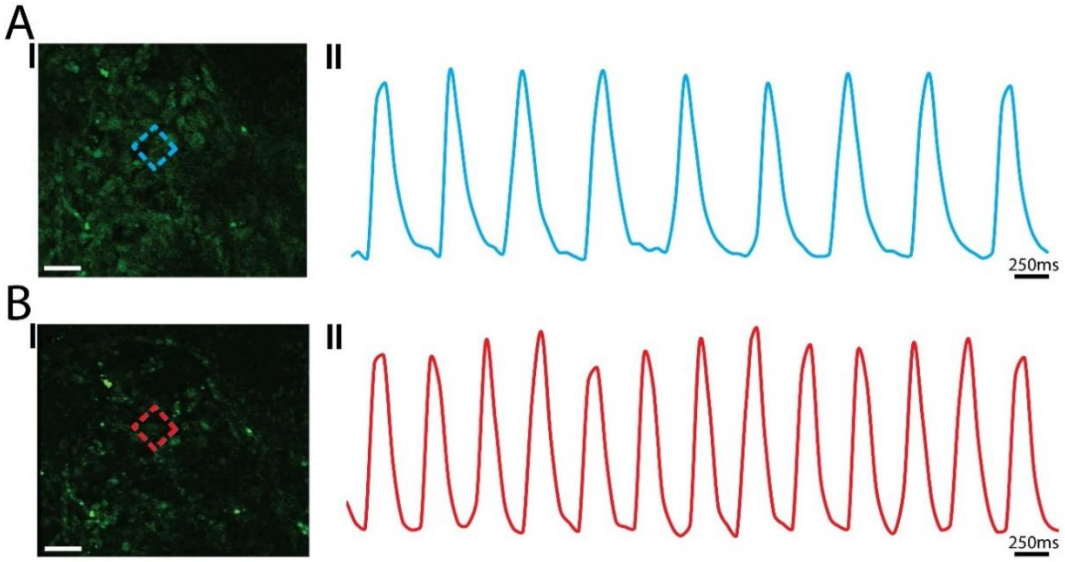

Figure 4.8 Effect of β-adrenergic receptor agonist on the Ca^{2+} fluorescence signals.
Ca^{2+} signals recorded from hESC-CMs cultured on graphene MEA, **(A)** before and **(B)** after application of isoproterenol. (I) Confocal image of hESC-CMs loaded with Ca^{2+} sensitive dye (Fluo-4), cultured on graphene electrodes. Scale bars: 50 µm. (II) Fluorescence intensity as function of time at the electrode region marked in (I).

The increase in the beat frequency was further supported by the simultaneous Ca^{2+} imaging performed on the cells interfaced with graphene electrodes (Figure 4.8). The addition of the drug also led to 0.9 fold decrease in FPD from 215 ± 9 msec to 187 ± 3 msec for Au electrodes (n=350

peaks across 5 channels), and 0.9 fold decrease from 215 ± 7 msec to 195 ± 6 msec for graphene electrodes (n=350 peaks across 5 channels) (Figure 4.9).

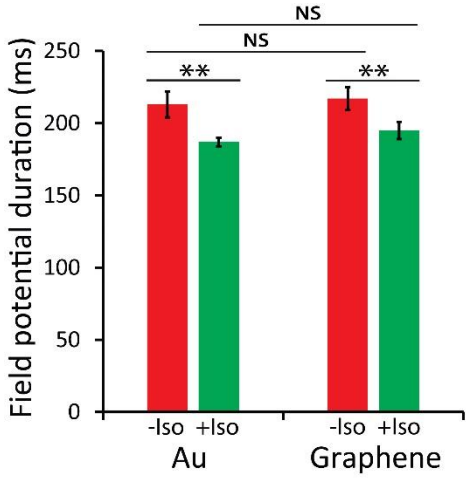

Figure 4.9 Effect of β-adrenergic receptor agonist on field potential duration.

The field potential duration of hESC-CM recorded using Au and graphene MEAs, before (red) and after (green) application of isoproterenol. (**) denotes statistically significant difference with $p<0.005$. NS denotes no statistically significant difference. Results are presented as mean ± SD (n=350 peaks across 5 channels).

4.5 Conclusions

In this work we developed a transparent biocompatible graphene-based platform that enables simultaneous electrical and optical recordings without affecting either of the recording modes. The high temporal resolution of the electrical recording provides information about all three ionic currents involved in action potential (i.e. Na^+, K^+ and Ca^{2+}), whereas high spatial resolution of the Ca^{2+} imaging provides information at a single cell level. The HNO_3 acid treatment of graphene led to electrode impedance reduction to values similar to Au electrodes, thus enabling recording of electrical signals at high SNR of ca. 14. This further indicates the flexibility and ease of surface

modification of graphene electrodes to enhance their electrochemical properties. The fabrication protocol suggested in this work can be easily extended to dense arrays of graphene electrodes to enable recording and studying of larger cellular networks. The biocompatibility of graphene demonstrated in this work and previous studies indicates the potential of graphene-based devices for long term stable tissue interfaces. The major advantage of the presented platform is the high transparency of the electrodes, which provides the flexibility to perform simultaneous optical studies for both electrophysiology applications such as Ca^{2+} imaging, and non-electrophysiology applications such as optogenetic manipulation of the cells,[159] optical coherence tomography (OCT) imaging,[167] monitoring biochemical activity of the cells using fluorescently labeled dyes and proteins,[168-170] and further investigation of the tissue health[132] at the electrode-cell interface over time. The developed platform will set the ground for further investigations of the relationship between electrical signals and reported diseases such as Alzheimer, Parkinson's disease and arrhythmias.

Chapter 5- 3D fuzzy graphene-based ultra-microelectrodes for sub-cellular electrical recordings

5.1 Introduction

The microelectrode array (MEA) technology has enabled investigation of network dynamics of excitable cells at high temporal resolution.[16-17] However, one of the biggest challenges in the field is to achieve sub-cellular spatial resolution since scaling down the geometric size of microelectrodes leads to an increase in the electrode impedance which significantly affects the recording capabilities of MEAs.[16, 41] Sub-cellular spatial resolution is crucial to enable high precision and accuracy of the cell under investigation, avoid averaging of signals from multiple cells, and enable investigation of sub-cellular events such as distribution of ion channels and propagation of electrical activity within a single cell.[16, 171-173] Recent works related to development of mesh electronics[171] and ultracompliant nanoelectronic probes[173] have demonstrated that reducing the geometric size of the electrodes enable fabrication on flexible probes with smaller footprint, thus leading to seamless integration with tissues and minimize mechanical mismatch and immune response. These studies suggest that further scaling down of the electrode size will improve interfaces between electronics and excitable tissues.[171-175] Furthermore, smaller footprint will enable increasing the density of recording sites thus enabling investigation of dense cellular networks.[171, 173, 176]

Reducing the impedance by surface modification of the electrodes has led to an improvement in the performance of the MEAs. Porous structure of Pt black coatings has led to reduction in impedance of metal electrodes.[177-180] Various Au nanostructures have also been reported such as deposition of nanoflake,[181-182] and fuzzy Au[183] structures. The rough surface of

these nanostructures increases the net surface area, thus reducing the impedance of the microelectrodes. To increase the effective surface area, the microelectrodes have also been modified with carbon nanotubes (CNTs) by direct synthesis[184] and electrodeposition of CNTs[185] on the electrode surface. Electrodeposition of iridium oxide films and conductive polymers such as poly(3,4- ethylene dioxythiophene) (PEDOT) and polypyrrole to the MEAs have also been demonstrated to reduce the impedance of the electrodes.[186-189] In addition, the use of PEDOT/CNT composites[190] and polypyrrole/graphene oxide composites[191] has shown to increase charge injection capacity of the microelectrodes (>200 mC/cm^2) by two orders of magnitude when compared with planar Pt electrodes (1.4 mC/cm^2). Even though the surface modifications improve the sensitivity of the MEAs by reducing the surface impedance and increasing the signal-to-noise ratio (SNR), the electrodes' geometry of tens of microns limits the capability for recording signals from subcellular structures, such as single axon and dendrites.[70] Additionally, poor adhesion of surface coatings suffer from delamination problems thus limiting long-term stable interfaces of the electrodes with cells and tissues.[192-193]

To address these limitations, we have developed microelectrodes using out-of-plane grown graphene. The extremely high surface area of three-dimensional fuzzy graphene (3DFG) and nanowire-templated 3DFG (NT-3DFG) enables scaling down the geometric size of the microelectrodes to sub-cellular scale.

5.2 3DFG and NT-3DFG MEA fabrication

The design of the 3DFG-based MEA is illustrated in Figure 5.1. The fabrication of 3DFG and NT3DFG MEAs was optimized using standard microfabrication techniques. Briefly, Pt interconnects and contact pads were patterned on Si/SiO_2 chips using photolithography and e-beam evaporation of Pt. Pt was chosen over Au because of higher melting point of Pt to avoid any breaks

in lines during the fuzzy graphene synthesis in the PECVD system. For NT-3DFG MEAs, 2 nm thick Au films were patterned in the sensing areas of the MEA chip. Si nanowires (SiNWs) were synthesized using Au-catalyzed vapor-liquid-solid (VLS) method. 3DFG was synthesized using plasma enhanced chemical vapor deposition (PECVD) process with growth times of 30 min and 90 min to investigate the effect of flake size and density on the performance of the electrodes.

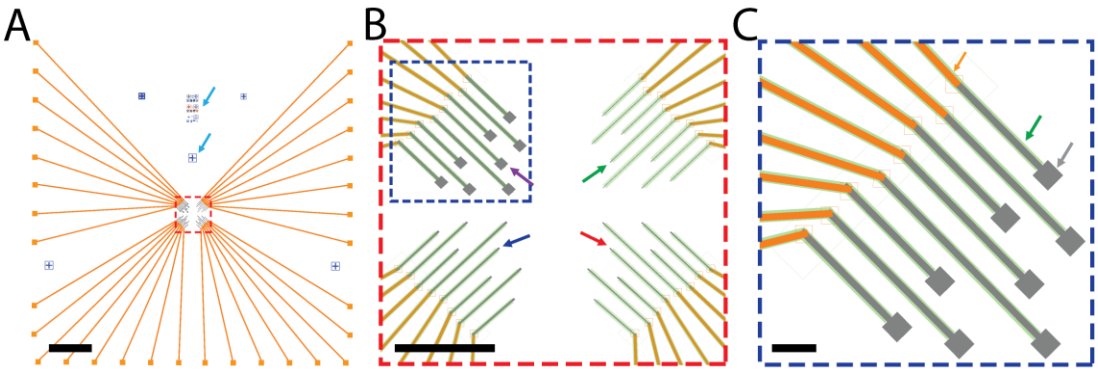

Figure 5.1 3DFG-based 32-channel MEA design with varying electrode geometric sizes. **(A)** Illustration of a 32-channel 3DFG MEA. Blue arrows indicate alignment marks. Orange lines and squares indicate Pt interconnects and contact pads, respectively. The 1.5 mm x 1.5 mm region in the center marked by the red dashed box represents 3DFG electrodes. Scale bar: 2 mm. **(B)** Expanded view of the marked dashed red box in (A). The purple, blue, red and green arrows denote 50 µm, 10 µm, 5 µm and 2 µm 3DFG electrodes, respectively. Scale bar: 500 µm. **(C)** Expanded view of the marked dashed blue box in (B). The orange, green and grey arrows denote passivated Pt lines, passivated 3DFG lines and exposed 3DFG electrodes, respectively. Scale bar: 100 µm.

Since synthesis of 3DFG is a substrate-independent process, 3DFG grows on the entire chip. Therefore, top down patterning of 3DFG is required to fabricate 3DFG and NT-3DFG electrodes. Top-down patterning usually uses resist or metal-based hard masks to protect the underlying

material in the regions of interest and the rest is etched using wet (acids/solvents) or dry (gas/plasma) techniques. Unlike monolayer graphene, the out-of-plane topography of 3DFG makes the patterning challenging. To address the rough surface of 3DFG, 100 nm of SiO_2 was deposited using PECVD system. PECVD deposition leads to conformal coating of SiO_2 on the 3DFG flakes thus enabling smooth coating of photoresists during the subsequent photolithography processes. Furthermore, SiO_2 layer prevents the flakes from physical damages from the subsequent steps. Next, Cr is patterned on top of SiO_2-coated 3DFG using photolithography and e-beam evaporation. Using Cr as the hard mask, SiO_2 and 3DFG from the non-electrode regions are etched off by CHF_3-based and O_2-based reactive ion etching (RIE) processes, respectively. Post-patterning, the Cr and SiO_2 layers present on top of the 3DFG electrode regions are then etched off using Cr etchant and buffered oxide etchant, respectively. In the final step, the non-sensing regions, i.e., Pt lines (Figure 5.1C, orange arrow) and 3DFG lines (Figure 5.1C, green arrow), are passivated with SU8 polymer, thus exposing only the 3DFG or NT-3DFG ends to the solution (Figure 5.1C, grey arrow). (For more details regarding 3DFG and NT-3DFG MEA fabrication, please see Appendix C)

5.3 MEA characterization

5.3.1 Structural

The structure and integrity of 3DFG and NT-3DFG post-fabrication was investigated by performing scanning electrode microscopy (SEM) and Raman spectroscopy characterization. The out-of-plane morphology of graphene flakes, as observed in the SEM images of 3DFG (Figure 5.2A) and NT-3DFG (Figure 5.2C) electrodes, confirmed that the fabrication process did not damage the flakes. The presence of graphene was confirmed by the presence of characteristic peaks in the Raman spectra, i.e., D, G, and 2D peaks (Figure 5.2B, D).[113] The D and D' peaks are

produced due to one-phonon defect-assisted process, and D+D' peak is produced due to two-phonon defect-assisted process.[113]

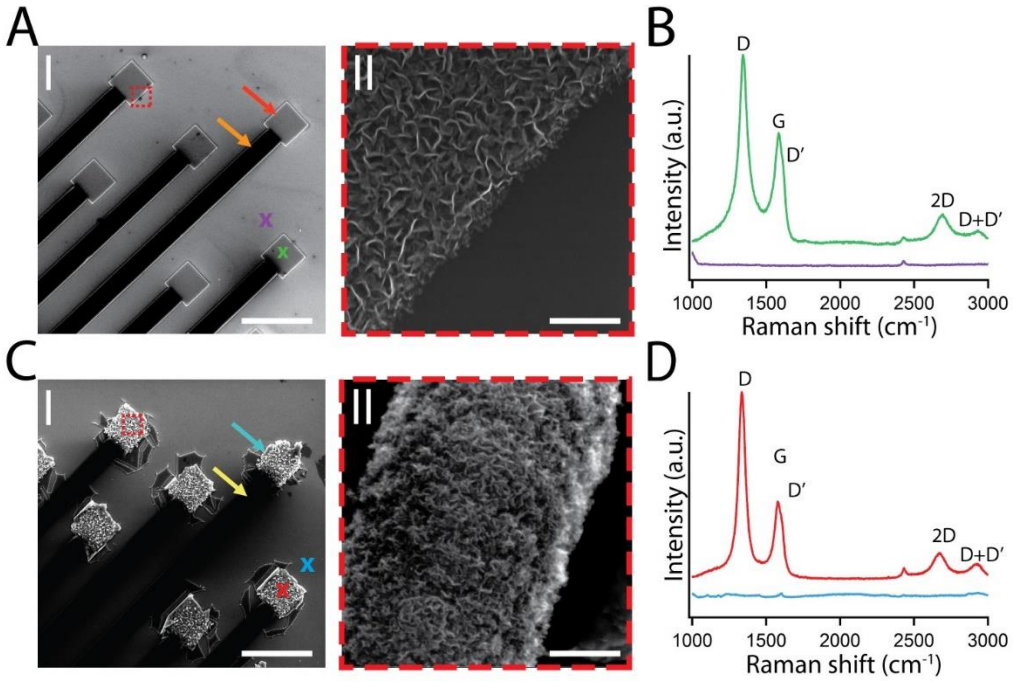

Figure 5.2 SEM characterization of 3DFG and NT-3DFG MEAs.

(A) (I) SEM image of 50 µm 3DFG MEA. Orange and red arrows denote passivated and exposed 3DFG electrode, respectively. Scale bar: 100µm. **(II)** Expanded view of the red dashed box marked in (I). Scale bar: 500µm. **(B)** Raman spectra acquired from the points marked in (A). **(C) (I)** SEM image of 50 µm NT-3DFG MEA. Yellow and cyan arrows denote passivated 3DFG and exposed NT-3DFG electrode, respectively. Scale bar: 100µm. **(II)** Expanded view of the red dashed box marked in (I). Scale bar: 500µm. **(D)** Raman spectra acquired from the points marked in (C).

In the case of 3DFG, the emergence of the D peak, at ca. 1335 cm^{-1}, and the D' peak, as a shoulder to the G peak, is caused by breaks in translational symmetry due to the presence of 3DFG edges, as evident in the SEM images (Figure 5.2A, C).[107, 113] The observed broad 2D peak can be

fitted with a single Lorentzian. This confirms the presence of juxtaposed single- to few-layer graphene flakes, in the form of high-density 3DFG.[114-115]. Furthermore, the absence of these peaks in the spectra acquired from the non-electrode regions confirmed successful patterning of 3DFG (Figure 5.2B, D).

5.3.2 Electrochemical

The electrochemical performance of the 3DFG and NT-3DFG electrodes was investigated using cyclic voltammetry (CV) and electrochemical impedance spectroscopy (EIS).

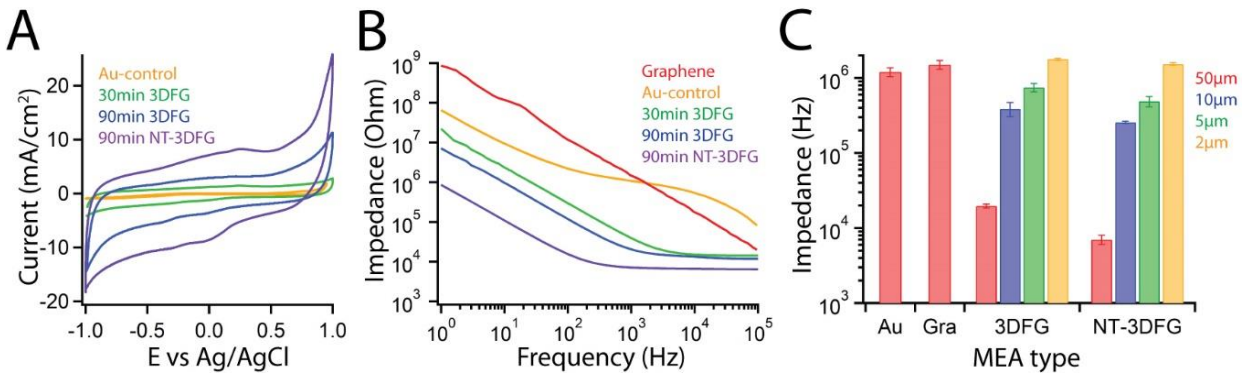

Figure 5.3 Electrochemical characterization.

(A) Cyclic voltammograms of 50 µm x 50 µm Au (orange), 30 min 3DFG (green), 90 min 3DFG (blue) and 90 min NT-3DFG (purple) electrodes acquired in 1 M KCl at 500 mV/s. **(B)** Impedance versus frequency plots for 50 µm x 50 µm monolayer graphene (red), Au (orange), 30 min 3DFG (green), 90 min 3DFG (blue) and 90 min NT-3DFG (purple) electrodes acquired in 1X PBS. **(C)** Impedance values at 1 kHz for Au, monolayer graphene, 3DFG and NT-3DFG electrodes. Red, blue, green and orange bars denote 50, 10, 5 and 2 µm electrode geometric sizes, respectively (n=5-8 electrodes for each electrode type).

The characterizations were performed using a three-electrode setup with Pt wire and Ag/AgCl as counter and reference electrodes, respectively. The 3DFG, NT-3DFG and Au-control

electrodes were used as working electrodes. To compare the electrochemically active surface area of different types of electrodes, capacitive currents were characterized by conducting CV with 1 M KCl electrolyte solution. The area under the CV curves provides information about the charge storage of an electrode ($charge = \frac{Area\ under\ curve}{scan\ rate}$), where area under the curve is the product of capacitive current and voltage. Since capacitance is related to the charge as per the equation: $Charge = capactiance \times voltage$, therefore capacitance of an electrode is directly proportional to the capacitive current.

Prior to exploring different electrode geometric sizes, the effect of 3DFG flake size and density was investigated on the electrochemical performance of 50 µm x 50 µm 3DFG and NT-3DFG MEAs. The flake size and density was controlled by changing the 3DFG synthesis time.[73] The high surface area of 30 min 3DFG electrodes led to ca. 40 folds higher capacitance compared to planar Au electrodes as observed in the CV characterization (Figure 5.3A). 90 min 3DFG, that had bigger flake size and more density and thus higher surface area, led to ca. 100 folds higher capacitance. Synthesizing 3DFG on a NW template in case of NT-3DFG further enhanced the net surface area of the electrode thus leading to ca.200 folds increase in the capacitance (Figure 5.3B). Since capacitance is directly proportional to the electrochemical surface area of an electrode,[127, 194] the CV curves suggest 200 folds higher electrochemical surface area of NT-3DFG microelectrodes compared to planar Au electrode of similar geometric area.

To characterize the impedance of the electrodes, EIS was performed in 1X phosphate buffer saline (PBS) solution. The frequency was scanned from 0.1 Hz to 100,000 Hz with V_{DC} of 0 V and V_{AC} of 10 mV, and impedance values at 1 kHz were noted. Increase in the surface area of 3DFG and NT-3DFG electrodes led to reduction in the electrode impedance, as evident by the EIS

characterization. Extremely high surface area of 90 min NT-3DFG electrodes led to ca. 200 folds reduction in the impedance compared to planar graphene and Au electrodes of similar geometrical surface area. Therefore, different geometric sizes of NT-3DFG electrodes ranging from 50 µm to 2 µm were fabricated and characterized using EIS. The 2 µm NT-3DFG electrodes showed similar impedance values as that of 50 µm planar graphene electrode (Figure 5.3C). The high surface area of NT-3DFG thus enabled scaling down of the geometric area of the electrode by 625 folds.

5.4 Electrical recordings using varying size NT-3DFG electrodes

The recording capabilities of NT-3DFG microelectrodes and ultra-microelectrodes were investigated by interfacing the human embryonic stem cells derived cardiomyocytes (hESC-CMs) with the NT-3DFG MEA chips with varying size electrodes ranging from 50 µm to 2 µm.

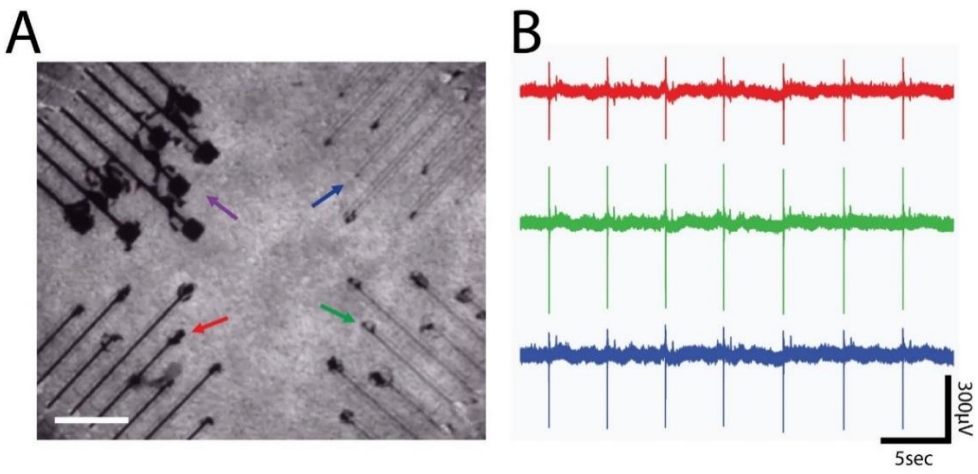

Figure 5.4 Electrical recordings using NT-3DFG electrodes.

(A) DIC image of hESC-CMs interfaced with NT-3DFG electrodes of varying geometric sizes. Purple, red, green and blue arrows denote 50, 10, 5 and 2 µm electrodes. Scale bar: 200 µm. **(B)** Representative recorded field potential traces using 10 µm (red), 5 µm (green) and 2 µm (blue) NT-3DFG electrodes.

NT-3DFG electrodes of 2, 5, 10 and 50 µm geometric area led to recording of field potentials with amplitude of 400-800 µV and high signal-to-noise ratio (SNR) of >10 (Figure 5.4).

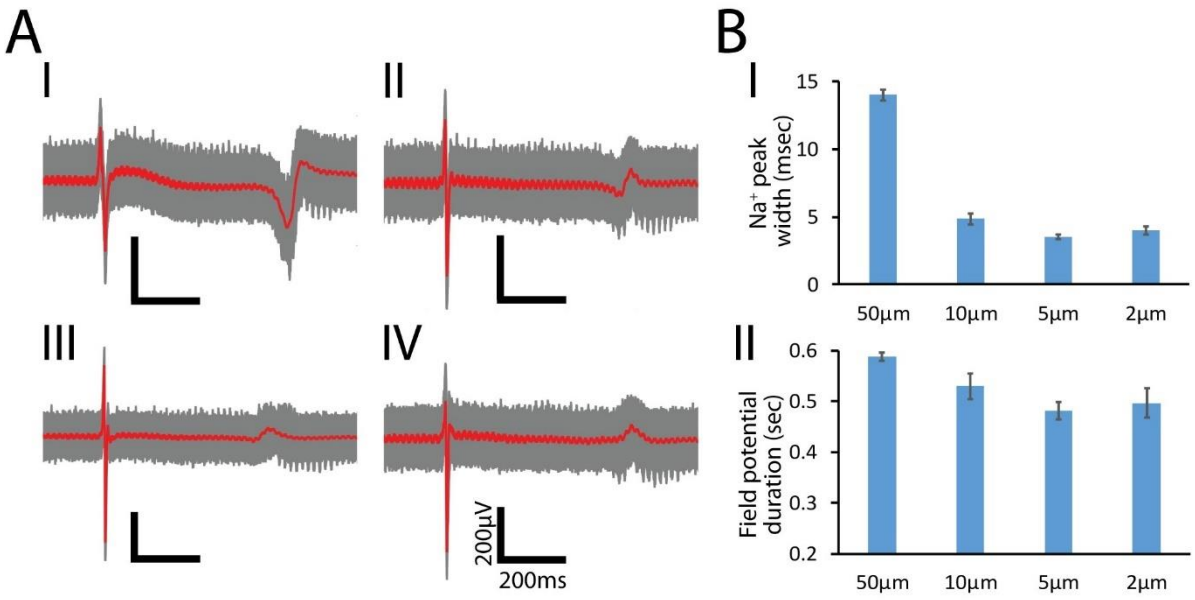

Figure 5.5 Extracellular field potential waveform analysis of signals recorded using NT-3DFG electrodes.

(A) Averaged peak (red trace) and raw data (grey traces, 60 peaks) of field potentials recorded using **(I)** 50, **(II)** 10, **(III)** 5 and **(IV)** 2 µm electrodes. **(B)** Na^+ peak width and **(C)** field potential duration as a function of electrode geometric sizes.

Additional analysis was done on the extracellular field potential waveforms. The field potentials recorded using ultra-microelectrodes of 10 µm and lower geometric sizes had significantly lower field potential duration (FPD) and Na^+ peak width compared to 50 µm electrodes (Figure 5.5). The wider FPD and Na^+ peak width in case of 50 µm electrodes is attributed to the averaging of the signals either from multiple cells or due to propagation of signals within the same cell, as opposed to the ultra-microelectrodes. These results highlight the

importance of using ultra-microelectrodes that enables higher spatial resolution and avoid averaging of signals which cannot be achieved with electrodes similar to or bigger than a cell.

5.5 Conclusions

This work demonstrates for the first time, recording of the electrical activity of excitable cells using ultra-microelectrodes ranging from 10 µm down to 2 µm, without the need of any surface coatings. The extremely high surface area-to-volume ratio of NT-3DFG enables fabrication of ultra-microelectrodes, as small as an axon, thus opening up possibilities to probe at sub-cellular scale and investigate activities such as distribution of ion channels and propagation of electrical activity within a single cell, which is not feasible with the current MEA technology. In addition, the ultra-microelectrodes are crucial for (i) improvement in precision and accuracy of cellular recordings, (ii) fabrication of high density electrode arrays to study network dynamics of dense cellular networks, (iii) prevention of signal averaging due to action potential propagation within and between cells, and (iv) minimizing the foreign body response in an *in vivo* environment.

Chapter 6- Non-genetic optical modulation of neuronal activity using nanowire-templated 3D fuzzy graphene

6.1 Introduction

The ability to modulate electrical activity of excitable cells has revolutionized our understanding of cellular functions, and has led to development of therapeutic platforms for various disorders, such as cardiac arrhythmia, epilepsy and Parkinson's disease.[38, 159, 180, 182, 195] Standard methods to modulate cellular activity of excitable cells use electrodes that inject charges to depolarize the cell membrane thus stimulating the cells.[195] However, the traditional bulky and rigid electrodes used for electrical stimulation are limited by inability to target single cells, poor precision and specificity, and high invasiveness that can induce severe inflammation in target tissue.[174, 196-199] The development of optogenetics has revolutionized our ability to control the activity in excitable cells and tissues. Optogenetics, which expresses microorganisms-derived light-gated ion channels in mammalian cells, enables modulation of electrical activity of cellular networks at high spatial and temporal resolution with single cell precision.[159] However, optogenetics require genetic manipulation of the cells that limits the clinical translation to humans and regulatory approval.[200-201]

Non-genetic photo-stimulation of cells and tissues can address the limitations of both electrical and optogenetics methods. A study in 2005 demonstrated a breakthrough technique that used infrared (IR) laser pulses to stimulate nerves and muscles *in vivo*.[202] Later, another study investigated the mechanism of IR stimulation in artificial lipid bilayers, cultured mammalian cells, and Na^+ and K^+ voltage-gated channels expressing *Xenopus laevis* oocytes.[203] The work demonstrated that IR radiation increases the temperature near the cell membrane that leads to

increase in its electric capacitance. The rate of change of capacitance leads to a capacitive current as per the equations:

$$Q = C_m \times V$$

$$i_C = \frac{dQ}{dt} = C_m \frac{dV}{dt} + V \frac{dC_m}{dt}.$$

where, i_C, Q, C_m and V represent capacitive current, transmembrane charge difference, membrane capacitance and membrane potential, respectively.

The capacitive current depolarizes the cell membrane and if the cell reaches its excitation voltage threshold it elicits an action potential.[203] This method thus enables modulation of neuronal activity without the need of genetic modifications. However, the use of IR for photothermal stimulation is limited by the absorption of the laser by the bulk medium that leads to poor spatial resolution and precision and the need of high laser energy.[201] More recently, photothermal stimulation using Au and Si-based nanomaterials have been shown to produce a more localized heating effect thus enabling modulation of cellular activity at sub-cellular spatial resolution and high precision with lower laser power compared to bare IR stimulation.[200, 204-206] However, these platforms are still limited by (i) need for relatively high laser power, (ii) low thermal conversion efficiency, (iii) limited photo-absorbance and absorption wavelengths or (iv) unproven long-term stability.

To address these challenges, we developed nanowire-templated three-dimensional fuzzy graphene (NT-3DFG) based hybrid-nanomaterial platform for photothermal modulation of neuronal activity. The few microns dimension of NT-3DFG enables high precision and spatial resolution. The relatively higher photo-absorbance and photo-thermal conversion efficiency of NT-3DFG compared to Au and Si-based nanomaterials allows stimulation at significantly lower

laser energies. In addition, the high absorbance of NT-3DFGs across the entire visible-near infrared (IR) spectra provides flexibility to stimulate the cells using different wavelengths.

6.2 NT-3DFG synthesis and characterization

NT-3DFG was synthesized as previously described in Chapter 2. Briefly, Si nanowires (SiNWs) were synthesized using Au-catalyzed vapor-liquid-solid (VLS) process on Si/SiO_2 chips. Post synthesis of SiNW, 3DFG was synthesized using plasma enhanced chemical vapor deposition (PECVD) process (Figure 6.1A). Sample preparation for structural, optical and photothermal characterization was performed by sonicating as-grown NT-3DFG samples in isopropyl alcohol (IPA) using a bath sonicator. The solution with isolated wires were then drop-casted on either quartz or Si/SiO_2 substrates depending on the application, and the IPA was allowed to evaporate. For cellular work, the as-grown samples were treated with HNO_3 to render the surface hydrophilic, followed by sterilization by 70% ethanol treatment and UV exposure. The wires were then functionalized with lysine-phenylalanine based peptide $(KF)_4$ since KF self-assembles on graphene surface[207] and renders the surface positive, thus facilitating adhesion of NT-3DFGs to the cell membrane. The wire suspensions were created via sonication in either 1X phosphate buffer saline (PBS) solution or cell culture media, and were added to the cells. (For more details, see Appendix E).

6.2.1 Structural and chemical characterization

The out-of-plane morphology of graphene flakes from the SiNW core was confirmed by the scanning electron microscopy (SEM) and transmission electron microscopy (TEM) imaging (Figure 6.1). High resolution TEM images also confirmed presence of single-to-few layer graphene flakes at the edges of NT-3DFG (Figure 6.1D-F).

The crystallinity of NT-3DFG was investigated using selected area electron diffraction (SAED). The diffraction patterns indicated that 3DFG is polycrystalline in nature (Figure 6.1 F (inset), Table 5).[109]

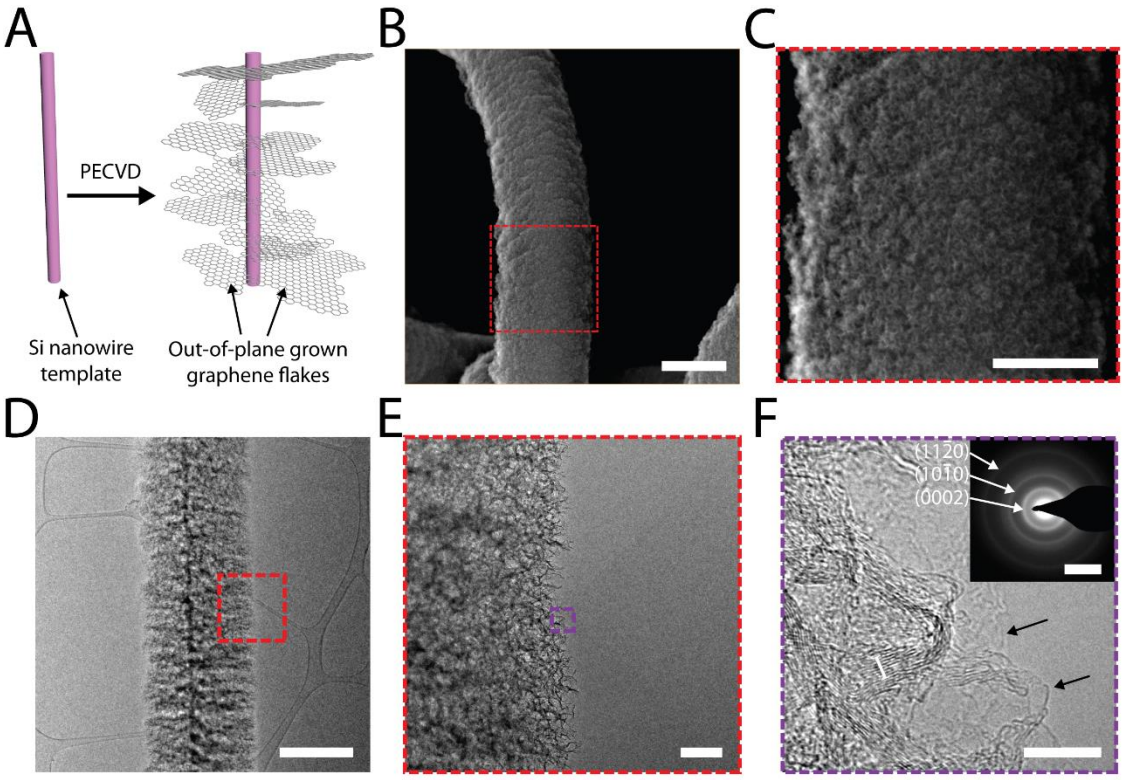

Figure 6.1 Highly controlled out-of-plane growth of single-to-few layers three-dimensional (3D) graphene flakes on a Si nanowire (SiNW).

(A) Schematics of NW-templated 3D fuzzy graphene (NT-3DFG). **(B)** SEM image of NT-3DFG. Scale bar: 1 µm. **(C)** Expanded view of the marked red dashed box in B. Scale bar: 500 nm. **(D)** High resolution-TEM image of NT-3DFG. Scale bar: 1 µm. (E) Expanded view of the marked red dashed box in (D). Scale bar: 100 nm. (F) Expanded view of the marked purple dashed box in (E). Black arrows indicate presence of single layer graphene. Inset is the representative SAED of an isolated NT-3DFG. Scale bars: 10 nm, 5 nm-1 (inset).

The inter-planar distances for the 1st and 2nd nearest C-C neighbors were experimentally derived to be 0.123 nm and 0.212 nm. These values agree with the expected inter-planar spacing for the $(11\bar{2}0)$ plane ($d_{11\bar{2}0}$ = 0.123 nm) and the $(10\bar{1}0)$ plane ($d_{10\bar{1}0}$ = 0.213 nm). The distance between individual graphene layers (d_{0002} = 0.360 nm) concurs with the expected value of 0.344 nm indicating the presence of turbostratic graphene.[110-112]

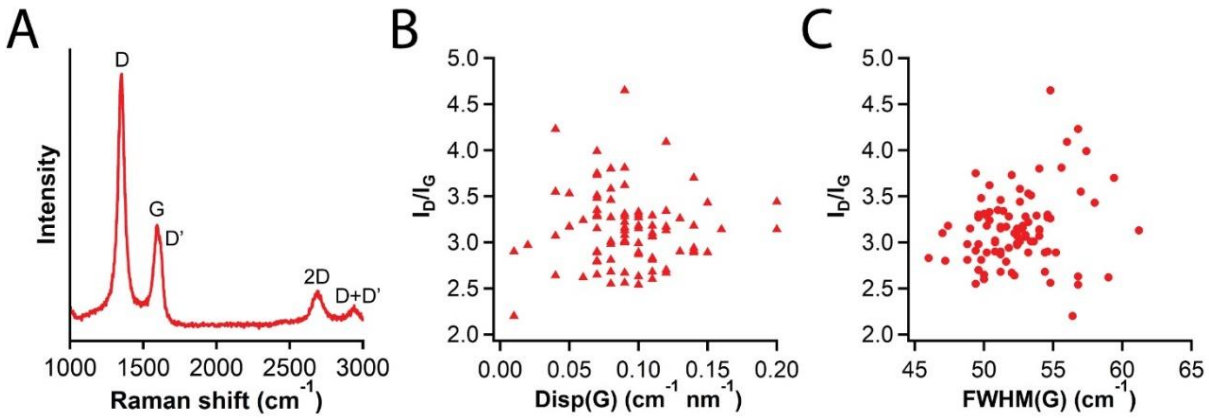

Figure 6.2 Raman spectroscopy of NT-3DFG.

(A) Representative Raman spectrum of a drop casted NT-3DFG (n=90 independent NT-3DFGs). **(B)** Peak intensity ratio of D peak to G peak (I_D/I_G) as a function of dispersion of G peak. **(C)** I_D/I_G as a function of FWHM of G peak (n=90 independent NT-3DFGs).

The presence of characteristic peaks in the Raman spectra, i.e., D, G, and 2D peaks, confirmed the presence of graphene (Figure 6.2A, Table 6). The D and D' peaks are produced due to one-phonon defect-assisted process, and D+D' peak is produced due to two-phonon defect-assisted process.[113] In the case of 3DFG, the emergence of the D peak, at ca. 1335 cm^{-1}, and the D' peak, as a shoulder to the G peak, is caused by breaks in translational symmetry due to the presence of 3DFG edges, as evident in the SEM and TEM images (Figure 6.1).[107, 113] The observed broad 2D peak can be fitted with a single Lorentzian, and explained by the presence of juxtaposed

single- to few-layer graphene flakes, in the form of high-density 3DFG.[114-115] The appearance of a strong D peak due to edge effects was further verified by dual-wavelength Raman spectroscopy. Increase in both the position of the G peak as a function of excitation wavelength (Disp(G)) and G peak full width at half maximum (FWHM(G)) is observed with an increase in the disorder in the carbon structure.[116] Therefore, a higher I_D/I_G corresponds to higher Disp(G) and FWHM(G) in the case of bulk structural defects.[114-115] The lack of clear correlation between I_D/I_G and FWHM(G) as well as between I_D/I_G and Disp(G) (Figure 6.2B, C, Table 7) further confirms that the major contribution to the D peak is due to edge defects rather than bulk-structural defects.[114-115, 117] The saturation of Disp(G) at 0.2 cm^{-1}/nm with change in excitation wavelength, is another indication of the presence of sp^2 hybridization and lack of large structural defects.

Surface chemistry of the pristine as well as surface-modified NT-3DFGs was investigated using X-ray photoelectron spectroscopy (XPS) characterization (Figure 6.3, Table 8, Table 9). XPS was performed on pristine NT-3DFG (Figure 6.3A I, B), HNO_3-treated NT-3DFG (Figure 6.3A II, C), and HNO_3-treated and KF modified NT-3DFG (Figure 6.3A III, D). Presence of a prominent sp^2 hybridized C1s peak at ca. 284 eV in all three conditions (Figure 6.3B I, C I, D I) corroborates the presence of sp^2 C lattice of graphene.[208-209] The peak at ca. 290 eV is attributed to $\pi \rightarrow \pi^*$ shake up satellite feature.[210] The peak at ca. 288 in C1s spectra is due to presence of O-C=O and/or N-C=O.[211-212] which is attributed to the formation of carboxylic groups due to nitric treatment[213] and amide bonds in peptides.[214] The peak at ca. 532.5 eV in the O1s spectra (Figure 6.3B II, C II, D II) is due to presence of C=O bonds.[214-215] The low intensity of O1s peak in case of pristine sample (Figure 6.3A I) might be attributed to adsorption of organic contaminants.[216]

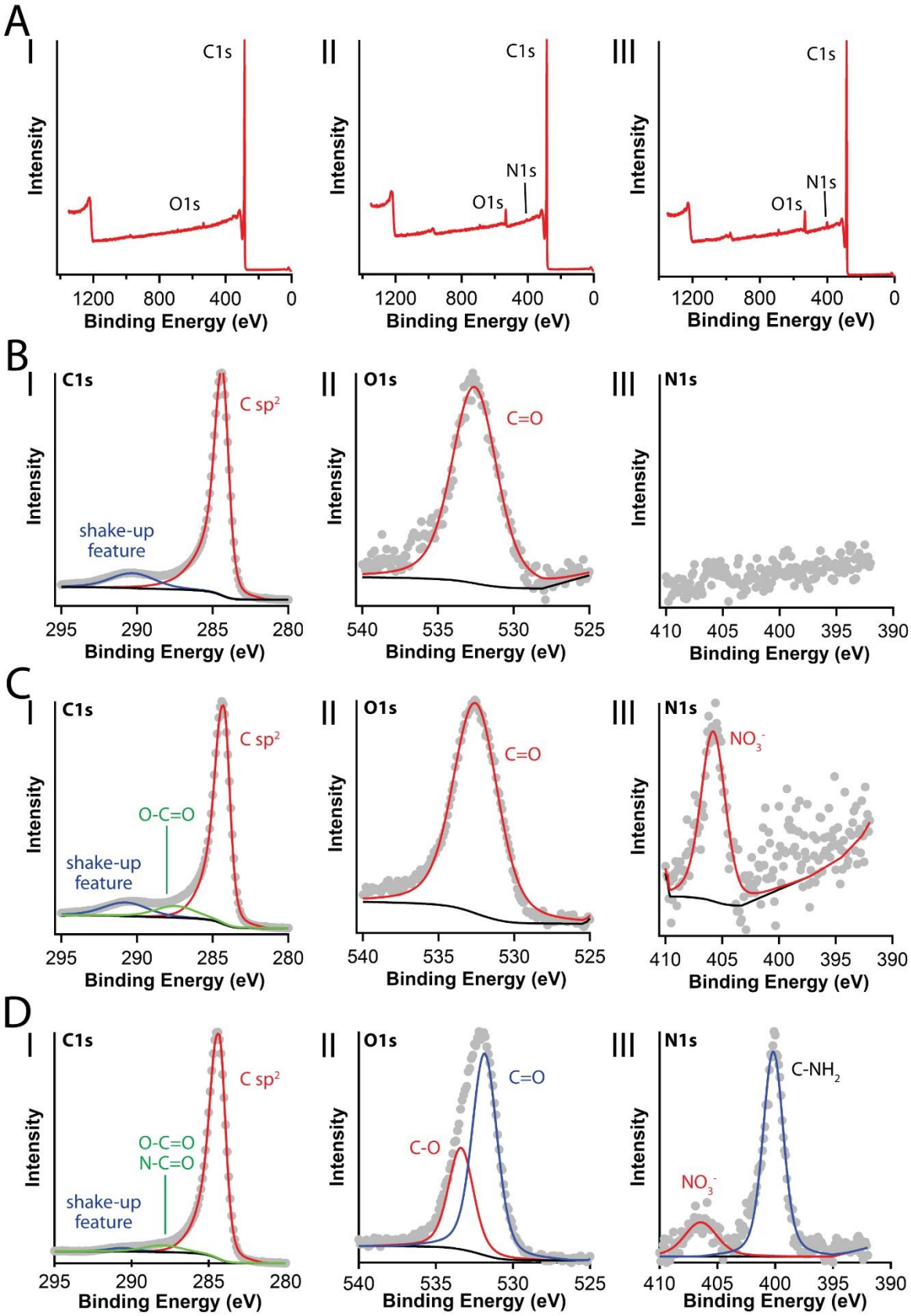
A
I
C1s
O1s
Intensity
1200 800 400 0
Binding Energy (eV)
II
C1s
N1s
O1s
Intensity
1200 800 400 0
Binding Energy (eV)
III
C1s
N1s
O1s
Intensity
1200 800 400 0
Binding Energy (eV)
B
I
C1s
C sp²
shake-up feature
Intensity
295 290 285 280
Binding Energy (eV)
II
O1s
C=O
Intensity
540 535 530 525
Binding Energy (eV)
III
N1s
Intensity
410 405 400 395 390
Binding Energy (eV)
C
I
C1s
C sp²
O-C=O
shake-up feature
Intensity
295 290 285 280
Binding Energy (eV)
II
O1s
C=O
Intensity
540 535 530 525
Binding Energy (eV)
III
N1s
NO3-
Intensity
410 405 400 395 390
Binding Energy (eV)
D
I
C1s
C sp²
O-C=O
N-C=O
shake-up feature
Intensity
295 290 285 280
Binding Energy (eV)
II
O1s
C=O
C-O
Intensity
540 535 530 525
Binding Energy (eV)
III
N1s
C-NH2
NO3-
Intensity
410 405 400 395 390
Binding Energy (eV)

Figure 6.3 NT-3DFG surface modification analysis.

(A) Representative X-ray photoelectron spectroscopy (XPS) survey of (I) pristine NT-3DFG, (II) HNO_3-treated NT-3DFG, and (III) HNO_3-treated and lysine-phenylalanine based peptide $(KF)_4$-modified NT-3DFG. **(B-D)** Representative (I) C1s, (II) O1s and (III) N1s spectra of **(B)**, pristine NT-3DFG, **(C)** HNO_3-treated NT-3DFG, and **(D)** HNO_3-treated and $(KF)_4$ modified NT-3DFG. Solid grey circles denote raw data. Data was acquired for n=3 independent samples for each condition.

The increase in the C=O peak intensity in the case of nitric-treated and KF modified NT-3DFG samples (Figure 6.3A II, III) can be attributed to presence of carboxylic groups[213] due to HNO_3 treatment[213] or peptide backbone.[214] The peak at ca 533 eV(Figure 6.3D II) can be attributed to C-OH group due to peptide modification.[214] The peak at ca. 406 eV in the N1s spectra of both nitric treated NT-3DFG (Figure 6.3C III) and KF modified NT-3DFG (Figure 6.3D III) samples is due to NO_3^- groups which can be attributed to the treatment with HNO_3-acid.[124, 217-218] The amide peak at ca. 400 eV in the N1s spectra for KF-modified NT-3DFG samples (Figure 6.3D III) confirms the presence of peptides on the NT-3DFG surface.[211-212, 214]

6.2.2 Optical and photothermal characterization

The effect of 3DFG flakes on the optical properties of NT-3DFG was investigated by extinction characterization. The polarization-resolved bright-field extinction measurements were performed on isolated NT-3DFG drop-casted on a quartz substrate, using a supercontinuum laser source. The average extinction spectra, plotted as $(1-\mathrm{T})\times 100\%$, where T is the measured transmittance, reveal broadband extinction spectra of the NT-3DFGs (Figure 6.4A). Moreover, the presence of 3DFG flakes led to 4 folds increase in the extinction compared to bare SiNW.[219] We

note that the % values in the extinction spectra depict the lower end since the laser spot used for the measurements is significantly larger than the diameter of the NT-3DFG.

To determine the local temperature change near the NT-3DFG as a result of laser illumination, photothermal characterization was performed using pipette resistance method[200, 220] as illustrated in Figure 6.4B. (For more details regarding photothermal characterization, please see Appendix E).

Briefly, NT-3DFGs were drop-casted on quartz substrates and immersed in 1X PBS solution. A pipette connected to a patch clamp amplifier, was brought in close proximity to a single NT-3DFG (~1-2 μm). Ionic currents through the pipette were recorded in a voltage-clamp mode, and the laser pulses with varying laser powers and pulse durations were applied to the NT-3DFG. In case of a photothermal response, the mobility of ions near the wire changes, that leads to changes in ionic currents recorded by the pipette.[200] The changes in the ionic currents are then used to measure the temperature change using a calibration curve (Figure 6.4C). The calibration curve was generated by exposing the pipette to the PBS solution at varying temperatures ranging from 25 ^{o}C to 50 ^{o}C, and simultaneously recording the current through the pipette in a voltage-clamp mode.

Illumination of laser pulses on isolated NT-3DFGs led to a photothermal response (Figure 6.4D-F). The local temperature change increased from 1.7±0.4 K to 6.1±1.1 K with increase in laser power from 2 mW to 10 mW (Figure 6.4D). The temperature change showed sub-msec temporal response (Figure 6.4E). The presence of fuzzy graphene on SiNW led to a ca. 6-fold increase in temperature change with 2.5-fold less laser power, compared to bare SiNW (Figure 6.4F).

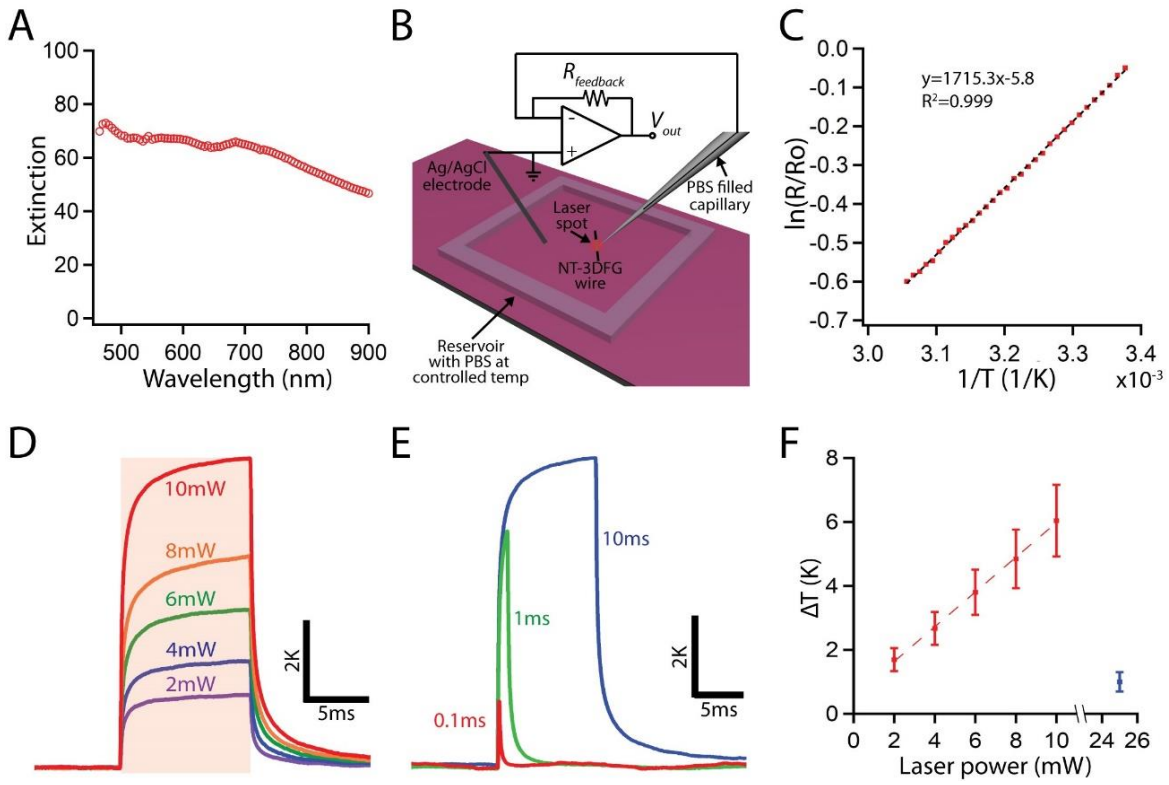

Figure 6.4 Optical and photothermal characterization of NT-3DFG.

(A) Mean extinction spectrum of isolated NT-3DFG as a function of wavelength (n=6). **(B)** Schematic illustrating photothermal characterization of a drop-casted NT-3DFG. **(C)** Calibration curve for a 1.9 MΩ pipette. **(D)** Representative temperature changes due to the photothermal effect of an isolated NT-3DFG as a function of laser power (635 nm laser, 20 µm spot size, 10 msec pulse width). Temperature values were averaged from 10 traces (n=10 isolated wires). The shaded region represents the duration of the laser pulse. **(E)** Representative temperature changes due to the photothermal effect of an isolated NT-3DFG as a function of laser pulse duration (635 nm laser, 20 µm spot size, 10 mW power). Temperature values were averaged from 10 traces (n=10 isolated wires). **(F)** Temperature change as a function of laser power for NT-3DFG (red) and bare Si nanowires (blue). Results are presented as mean ± SD (n=10 isolated wires, 10 measurements per wire).

This enhanced performance of NT-3DFG could be attributed to high absorbance and high photo-thermal conversion efficiency of the hybrid-nanomaterial.

6.3 Photothermal stimulation

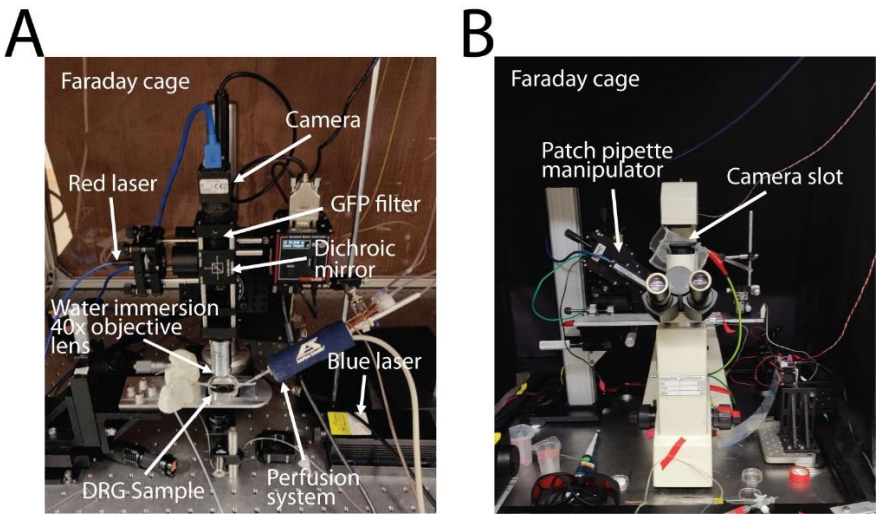

Figure 6.5 Photothermal stimulation: microscope setups.

(A) Custom-built single-photon microscope for photothermal characterization of NT-3DFGs, and Ca^{2+} imaging of neurons during photo-stimulation. **(B)** Custom-built microscope setup for patch-clamp measurements of neurons during photothermal stimulation.

Post photothermal characterization, NT-3DFGs were used for photothermal stimulation of cells. Custom-built setups were used to perform either patch clamp measurements or Ca^{2+} imaging of the cells during photo-stimulation (Figure 6.5). The KF-modified NT-3DFG suspension was added to the primary culture of neonatal rat dorsal root ganglia (DRG). Cells were incubated for at least 2 hours to ensure adhesion of wires on the cell membrane and photothermal stimulation was performed (Figure 6.6A, B).

6.3.1 Modulation of electrical activity

Illuminating the cell-wire interface with laser pulses led to depolarization of the cell membrane as observed in the patch clamp measurements. The membrane potential was progressively depolarized with increase in the laser energy, i.e., either by increasing the laser power from 1.45 mW to 3.02 mW and keeping pulse duration fixed at 1.2 msec (Figure 6.6C) or by increasing the laser pulse duration from 0.4 msec to 1.6 msec and keeping the laser power fixed at 2.28 mW. (Figure 6.6D). The laser energy of ca 3.6 µJ induced enough depolarization of the cell membrane to reach the threshold potential thus leading to an action potential. These energy values are significantly smaller than what has been demonstrated with other Si and Au-based nanomaterials.[204, 206, 220]

The laser energy required to elicit an action potential was further reduced by applying laser pulses of few-to-10s of µsec pulse duration, for e.g. 20 µsec laser led to an action potential using ~100 nJ laser energy, and 2 µsec laser led to action potential using ~20 nJ laser energy, as compared to 1 msec pulses that needed ~2.7 µJ laser energy (Figure 6.6E). This could be explained by the dependence of the membrane depolarization on the rate of capacitance change (dC_m/dt).[201] Greater the value of dC_m/dt, larger is the capacitive current. Higher current leads to more membrane depolarization, thus making it easier to reach the excitation threshold. Use of ultra-short pulses significantly increases the dC_m/dt,[201] thus, enabling stimulation at much lower energies in the range of 10s-to-100s of nanojoules, i.e. orders of magnitude lower compared to laser pulses of few msec durations.

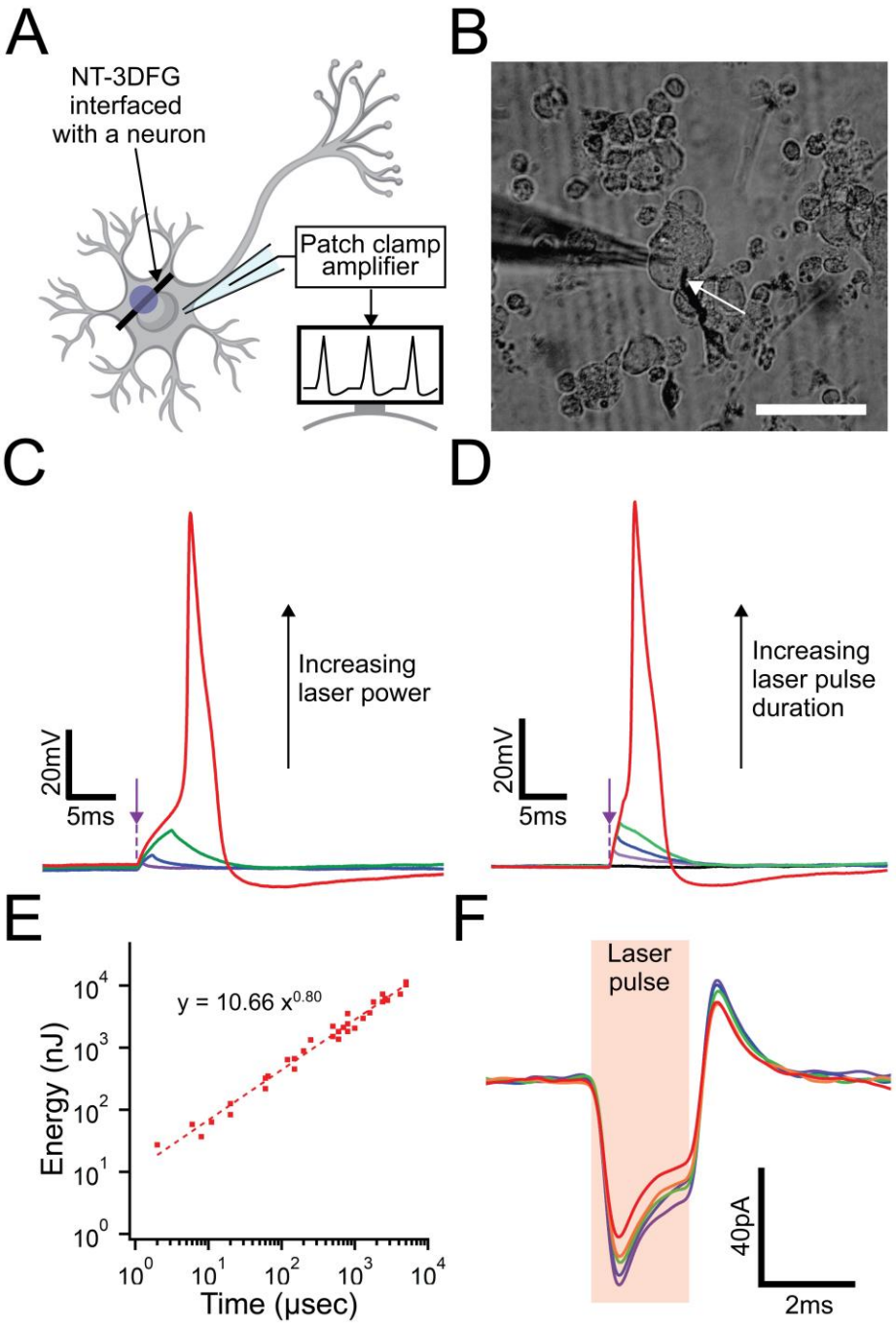

Figure 6.6 Photothermal stimulation of dorsal root ganglia (DRG) neurons with NT-3DFG

(A) Schematics illustrating a NT-3DFG interfaced with a DRG neuron for photothermal stimulation. Purple spot indicates laser illumination area. **(B)** Bright field image of a DRG neuron interfaced with a NT-3DFG. White arrow indicates the laser pulse illumination point.

Figure 6.6 continued: Scale bar, 50 µm. **(C)** Representative recorded membrane potential of a DRG neuron. The DRG neuron was illuminated by 405 nm laser with 1.2 msec pulse duration and varying powers of 1.45 mW (1.74 µJ, violet), 1.73 mW (2.08 µJ, blue), 2.28 mW (2.73 µJ, green), and 3.02 mW (3.62 µJ, red) The purple arrow indicates the applied laser pulse starting point. **(D)** Representative recorded membrane potential of a DRG neuron. The DRG neuron was illuminated by 405 nm laser of 2.28 mW power and varying pulse durations of 0 msec (0 µJ, black), 0.4 msec (0.91 µJ, violet), 0.8 msec (1.82 µJ, blue), 1.2 msec (2.74 µJ, green), and 1.6 msec (3.65 µJ, red). The purple arrow indicates the applied laser pulse starting point. **(E)** Laser energy required for photothermal stimulation of neurons as a function of laser pulse duration (n=12 DRG neurons). **(F)** Representative recorded capacitive current transients in response to laser pulses with pulse duration of 2 msec and laser power of 1.73 mW (3.46 µJ). Neurons were patch clamped in a whole cell voltage clamp mode with holding potentials of -150 (violet), -140 (blue), -130 (green), -120 (orange) and -110 (red) mV (n=3 DRG neurons).

Recently, a study demonstrated that for a pure opto-capacitance based stimulation of cells, the energy needed to reach membrane threshold potential (E_{Th}) and the laser pulse duration (Δt) follow a power law relationship, i.e., $E_{Th} = a \times \Delta t^{b}$.[201] Similar observation was made for the NT-3DFG based photo-stimulation with a=10.66 and b=0.8 (Figure 6.6E). This confirms the opto-capacitive mechanism of the stimulation, i.e., stimulation occurred due to changes in membrane capacitance instead of activation of other channels such as temperature-sensitive TRPV1 and mechano-sensitive channels.[201] Additionally, the coefficient of the fit i.e. a=10.66 (Figure 6.6E) shows 2.5 to 10-folds higher efficiency of NT-3DFG compared to CNT-mesh and graphite-based nanomaterials.[201] Furthermore, the voltage-clamp recordings clearly show generation of capacitive

currents upon laser illumination on the NT-3DFG-neuron interface (Figure 6.6F) corroborating the opto-capacitive nature of the stimulation.

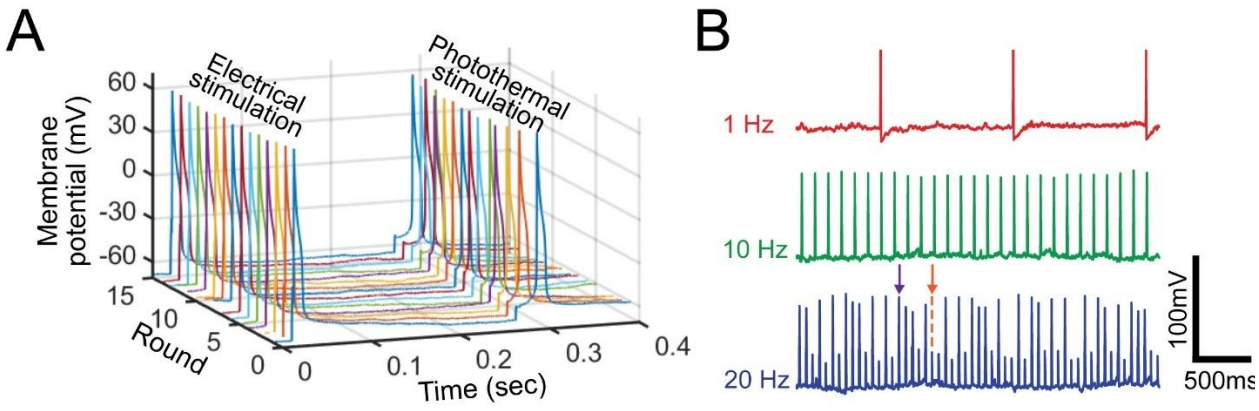

Figure 6.7 Highly controlled photothermal stimulation of neurons.

(A) Representative recorded membrane potential of a repetitively stimulated DRG neuron. **(B)** Representative recorded membrane potential of a DRG neuron exposed to trains of laser pulses at different frequencies (n=3 DRG neurons). A 405 nm laser with pulse of 3.02 mW power and 0.7 msec pulse duration (2.11 µJ) was used. The purple and orange arrows indicate an action potential and a subthreshold depolarization, respectively.

To investigate the reproducibility of the photothermal stimulation technique, we illuminated the same NT-3DFG-cell interface multiple times. Figure 6.7A shows the response of the neuron upon electrical stimulation using patch clamp (left curves) and photothermal stimulation using 405 nm laser (right curves). The cell elicited action potential for every round showing high reproducibility. Furthermore, the laser pulses were applied with varying frequencies of 1, 10 and 20 Hz for 10 sec each. Figure 6.7B shows the action potentials elicited as a result of the laser pulses. 10 pulses of 1 Hz laser and 100 pulses of 10 Hz laser led to full action potentials post each laser pulse. At 20 Hz, action potential generation became less efficient as evident by the

presence of sub-threshold signals (Figure 6.7B, orange arrow). At higher frequencies, the efficiency of the action potential is limited by the intrinsic ion channel kinetics.[203, 221]

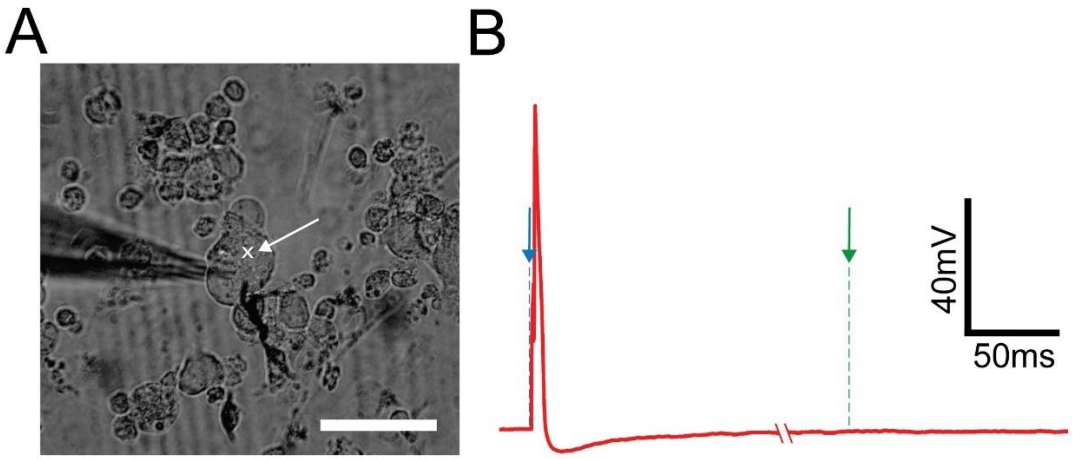

Figure 6.8 Control experiment with an off-NT-3DFG illumination.

(A) Bright field image of a DRG neuron interfaced with NT-3DFG. White arrow indicates the point where the laser pulse was applied. Scale bar: 50 µm. **(B)** Representative intracellular electrical recordings of DRG neurons illuminated by 405 nm laser with 1.2 msec pulse duration and 3.02 mW applied power (3.62 µJ). Blue and green arrows represent the time points when the electrical and the optical stimulation pulses were applied, respectively.

To check if the observed electrical behavior is due to the temperature change generated by the NT-3DFG, we performed control experiments where the laser was illuminated on the cell but away from the wire (Figure 6.8A). An electrical stimulation pulse was applied (blue arrow) to show that the cell is functionally active and excitable, and a laser pulse was applied (green arrow) on the same cell with same power and pulse duration as before. No change in the membrane potential confirmed that the stimulation of the cell was due to the photothermal effect of the NT-3DFG.

6.3.2 Effect of photothermal stimulation on the cell viability

To investigate the effect of laser pulses on the cell viability, the DRG neurons were loaded with calcein dye that labels the live cells green, and were imaged using blue laser and GFP filter. The cells were interfaced with NT-3DFGs and 1 msec laser pulses of varying laser power ranging from 4 mW to 25 mW were applied to the cell-wire interface (Figure 6.9A). The cell was imaged before and after 10 iterations of pulses at 4, 6, 8, 10 and 25 mW power.

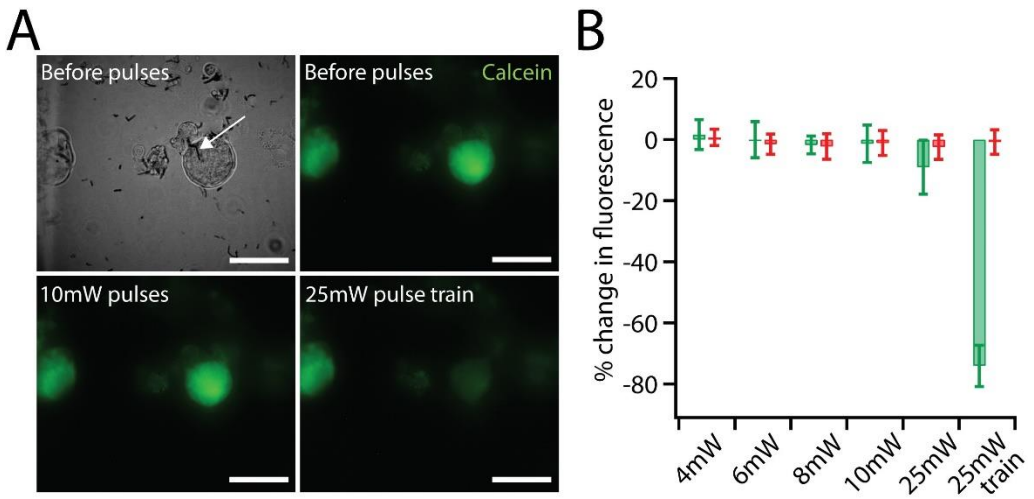

Figure 6.9 Photothermal stimulation with NT-3DFG does not affect cellular viability.

(A) Bright field and fluorescence images of calcein loaded DRG neurons before and after 10 pulses of 635 nm laser with varying laser power of 4 mW (4 µJ), 6 mW (6 µJ), 8 mW (8 µJ), 10 mW (10 µJ), and 25 mW (25 µJ). 10 pulses of 1 msec duration at 1 Hz were applied for each power. 25 mW train refers to 1000-2500 pulses of 1 msec duration at 500 Hz. White arrow indicates the NT-3DFG illuminated by the laser. Red arrow indicates the neighboring cell not illuminated by the laser. Scale bars: 50 µm. **(B)** Change in fluorescence of targeted cells (green) and neighboring cells (red) as a function of laser power. Results are presented as mean ± SD (n = 9 DRG neurons).

No significant fluorescence change was observed for laser powers from 4 to 25 mW. As a control, the cells were then exposed to 1000-2500 pulses at 500 Hz frequency to induce cell death, indicated by the significant loss in fluorescence ($p<0.005$) (Figure 6.9B). No change in the fluorescence of the neighboring cells confirmed that the fluorescence change of the cell under stimulation was not due to bleaching of the dye (Figure 6.9B). The quantification clearly shows that 1 msec laser pulses with power of 25 mW (energy of 25 μJ) or less does not induce cell death. The maximum energy used for photothermal stimulation of neurons was 6 μJ, significantly lower than the energy needed to kill the cells. This assay confirms the safety of the photothermal stimulation of neurons using NT-3DFG.

6.3.3 Multi-cell dynamics via calcium imaging

The effect of photothermal stimulation on the calcium dynamics of neurons was also investigated. Calcium is a ubiquitous second messenger, that plays an essential role in the signal transduction of excitable cells.[222] Calcium ions enter the excitable cells during an action potential firing, therefore, the electrical activity of neurons can also be assessed by monitoring the calcium flow across the cell membrane.[222] In addition, calcium imaging enables investigation of cellular activity at a network scale,[222] which is immensely challenging using the patch clamp technique. The cells were loaded with calcium indicator dye, Cal-520, and the calcium dynamics was observed via fluorescence imaging using a custom-built single photon microscope. (For more details, see Appendix E).

6.3.3.1 2D neuronal culture

Stimulation of neurons leads to influx of calcium ions through ion channels on the cell membrane.[200, 204, 220] To investigate the effect of photo-stimulation on the calcium dynamics of DRG neurons NT-3DFGs were interfaced with the cells loaded with calcium indicator dye, Cal

520. The illumination of the wire-cell interface with a laser of 4 mW power and 1 msec pulse width led to an influx of calcium, as evident from the increase in fluorescence of the calcium indicator (Figure 6.10). Furthermore, the stimulation led to the propagation of the calcium activity from the cell under stimulation to the neighboring cells as observed by the delay in the fluorescence change response of the neighboring glial and neuronal cells (Figure 6.10B). The propagation of the calcium activity could be explained by the intercellular junctions and diffusion of chemical messengers.[223-225] This experiment confirmed that the photo-stimulation of neurons using NT-3DFG can enable modulation of the calcium dynamics at a single cell as well as network level.

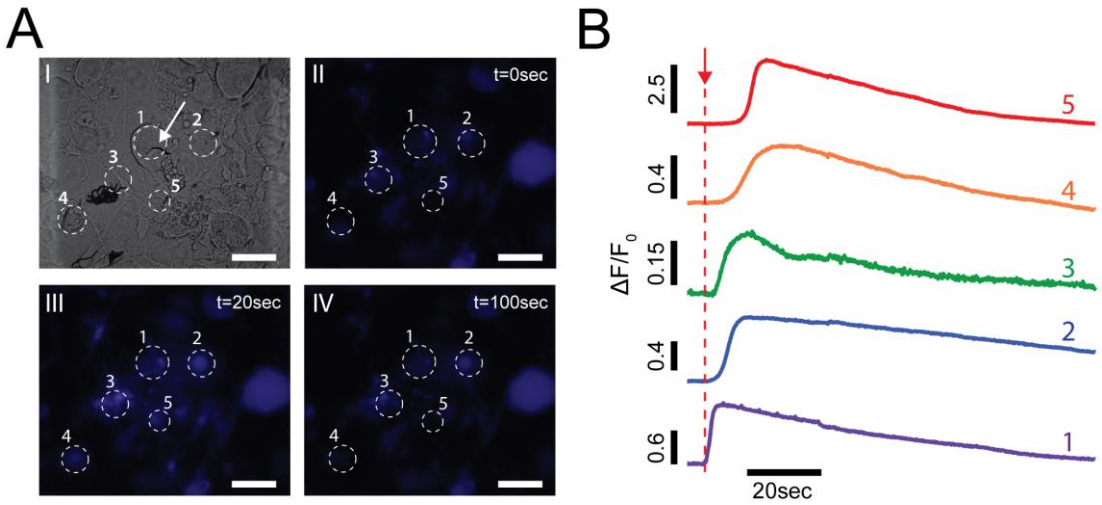

Figure 6.10 Photothermal stimulation of a 2D network of DRG cells.

(A) Representative bright field (I) and time-series fluorescent images (II-IV) of cells loaded with calcium indicator dye (Cal 520) (n=15 neurons). 635 nm laser with pulse of 4 mW power and 1 msec pulse duration (4 µJ) was applied at t=5 sec. White arrow indicates the NT-3DFG illuminated by the laser pulse. Scale bars: 50 µm. **(B)** Normalized calcium fluorescence intensity curves of the cells marked in A. Red arrow represents applied laser pulse starting point (t=5 sec).

As a control, laser was illuminated away from the wire with the same laser power and pulse duration that led to stimulation before, and the fluorescence imaging was performed to monitor

the calcium flux. No change in fluorescence of the calcium indicator was observed even after multiple pulses (Figure 6.11) thus confirming that the calcium influx was triggered by the photothermal effect of the NT-3DFG.

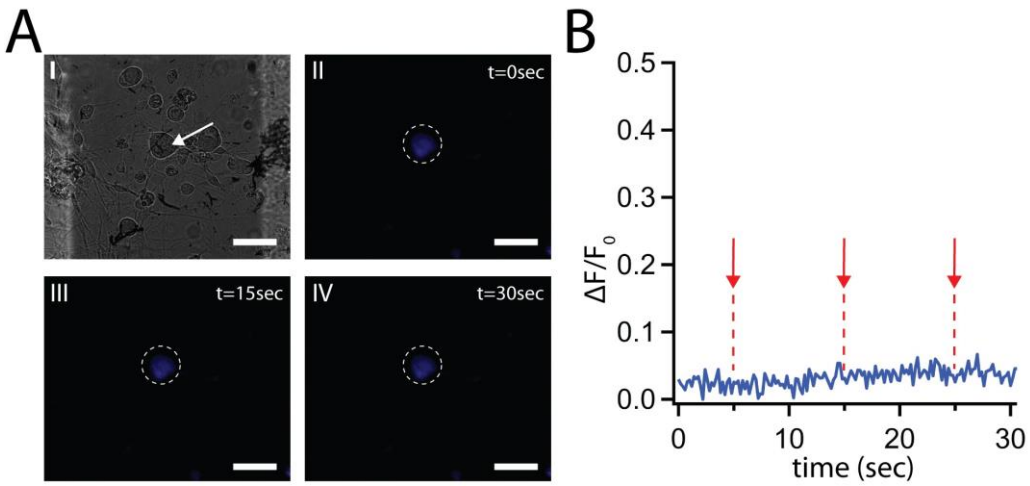

Figure 6.11 Control experiment with an off-NT-3DFG illumination.

(A) Bright field (I) and time-series fluorescent images (II-IV) of cells loaded with calcium indicator dye (Cal 520). 635 nm laser pulses of 4 mW power and 1 msec pulse duration (4 µJ) were applied at t=5, 15 and 25 sec. White arrow indicates the point illuminated by the laser pulse. Scale bars: 50 µm. **(B)** Normalized calcium fluorescence intensity curve of the cell marked in a. Red arrows represent the applied laser pulses starting point (t=5, 15 and 25 sec).

6.3.3.2 3D neuronal network

Modulating activity of neurons in their 3D microenvironment is crucial since cells cultured in 3D represent more *in vivo*-like behavior in terms of morphology[226-227], cell survival[228], and electrophysiological characteristics such as synapse formation, membrane resting potential, maximum depolarization slope, and action potential duration.[229-231] The inability of 2D cell culture models to recapitulate *in vivo*-like cytoarchitectural organization and inter-cellular connections has impeded their use, especially for disease modeling and therapeutic applications.[232-233] Recently,

complex 3D arrangements of cells resembling human tissue, spheroids and organoids, have been developed that has opened up opportunities to allow better understanding of cellular physiology both in healthy and diseased states.[232-235] However, there is still a need to develop a minimally invasive and biocompatible platform that can allow precise modulation of the cellular activity in their 3D microenvironment. Therefore, to bridge the gap we explored the possibility to stimulate 3D neuronal micro-tissues using NT-3DFG.

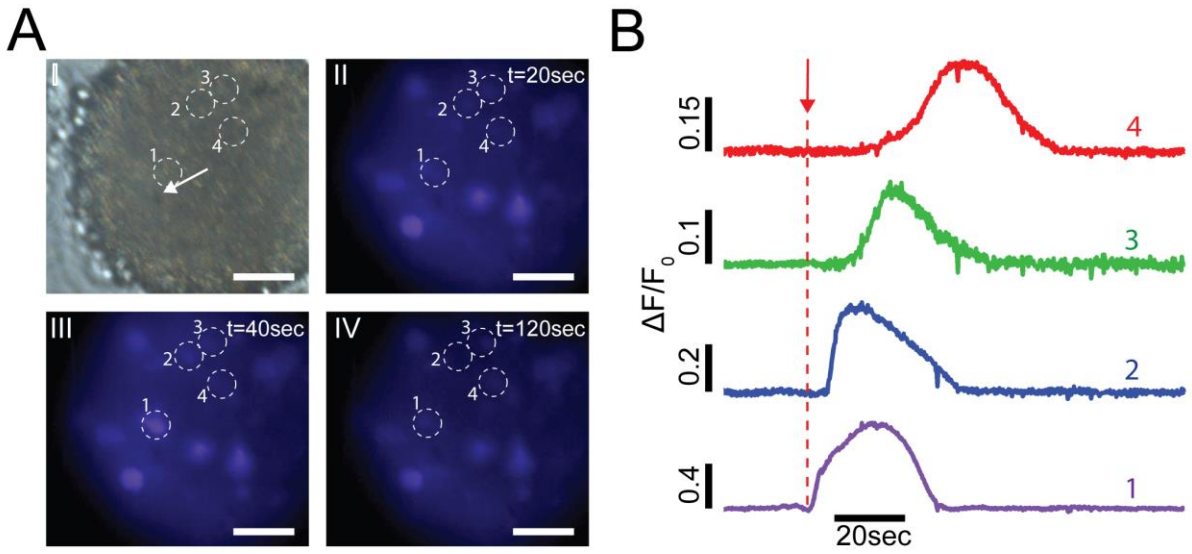

Figure 6.12 Photothermal stimulation of 3D cortical spheroids.

(A) Representative bright field (I) and time-series fluorescent images (II-IV) of a cortical spheroid loaded with calcium indicator dye (Cal 520) (n=8 tissues). 635 nm laser with pulse of 6 mW power and 1 msec pulse duration (6 µJ) was applied at t=25 sec. White arrow represents the NT-3DFG illuminated by the laser pulse. Scale bars: 50 µm. **(B)** Normalized calcium fluorescence intensity curves of the cells marked in A. Red arrow represents the applied laser pulse starting point (t=25 sec).

Cortical spheroids were formed by seeding embryonic rat derived cortical neurons in agarose-based micromolds. The tissues were cultured for 3-4 weeks to allow for compaction and

maturation of the neurons. The spheroids were then interfaced with dispersed NT-3DFGs and the calcium dynamics of the neuronal network was investigated (Figure 6.12A). Illuminating the wire-spheroid interface with laser pulses of 4-6 mW power and 1 msec pulse width led to influx of calcium in the neuronal cells. The signal propagated to the neighboring cells as observed by the change in fluorescence intensity of the cells (Figure 6.12B). The calcium transients of these spheroids is similar to what has been observed in the literature.[236-239]

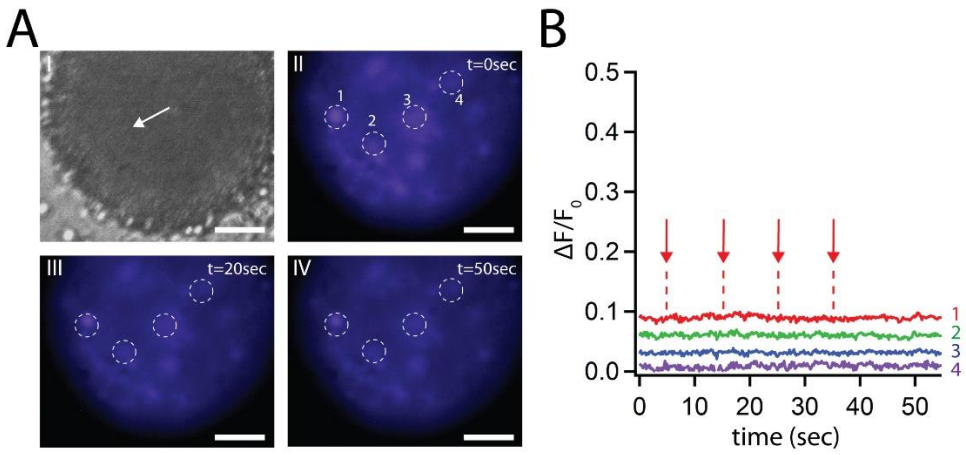

Figure 6.13 Control experiment with an off-NT-3DFG illumination.

(A) Bright field (I) and time-series fluorescent images (II-IV) of cells loaded with calcium indicator dye (Cal 520). 635 nm laser pulses of 6 mW power and 1 msec pulse duration (6 µJ) were applied at t=5, 15, 25 and 35 sec. White arrow indicates the point illuminated by the laser pulse. Scale bars: 50 µm. **(B)** Normalized fluorescence intensity curve of the cell marked in a. Red arrows represent the applied laser pulses starting point (t=5, 15, 25 and 35 sec). The curves were offset along y-axis to avoid overlap.

As a control, the laser pulses were applied away from the wire, and no fluorescence change was observed (Figure 6.13). These experiments demonstrate that NT-3DFG based photothermal

platform enables precise modulation of the cellular activity at a single cell as well as network level, both in 2D and 3D microenvironment.

6.4 Conclusions

In conclusion, this work demonstrates the possibility to modulate the neuronal activity both in 2D and 3D without the need of any genetic modification, and at high spatial and temporal resolution, not achievable through electrical or optogenetic approaches. The unique and extraordinary optical properties and photothermal conversion efficiency of NT-3DFG hybrid nanomaterial enables photo-stimulation with laser energies orders of magnitude lower than other nanomaterials. The high biocompatibility and easy-to-use setup of this method opens up opportunities to study neural functions both in healthy and diseased state, and enable therapeutic platforms for various neurological disorders, such as epilepsy and Parkinson disease.

Chapter 7- Conclusions and future outlook

This thesis enabled development of unique nanomaterial-based interfaces with excitable cells to investigate and modulate their activity. Use of an extraordinary carbon-based nanomaterial, graphene, and engineering its physical, chemical and electrical properties allowed us to push the limits of the current optical and bioelectronics platforms in terms of stable and biocompatible interfaces that enable recording and stimulation with more precision, sub-msec temporal and sub-cellular (few microns) spatial resolutions.

In this thesis, bottom-up techniques were developed and optimized to synthesize graphene with different morphologies. This enabled tailoring of the physical, chemical, electrical and optical properties of graphene, and development of different graphene-based platforms for different applications. Low pressure chemical vapor deposition (LPCVD) process was optimized to achieve high quality, continuous centimetre-scale and defect-free monolayer graphene with high transparency of ca. 97.5%.[132, 240] Plasma enhanced chemical vapor deposition (PECVD) process was optimized to obtain highly controlled synthesis of out-of-plane single-to-few layer graphene flakes on a 3D Si nanowire (SiNW) mesh template, thus leveraging graphene's outstanding surface area-to-volume ratio.[73]

To address the growing debate in research community regarding toxicity of various nanomaterials, especially graphene, a highly sensitive and reliable methodology to assess the biocompatibility of nanomaterials was developed. One of the key limitations in previous studies is the lack of investigation of the graphene effect on cell stress using reliable and sensitive intracellular indicators under physiological conditions. This limitation was addressed by assessing the effect of graphene on cell stress using three highly sensitive indicators: mitochondrial membrane potential (MMP), mitochondrial morphology, and autophagy levels. The results

indicated that graphene promotes proliferation of fibroblast cells and maturation of excitable cells. In addition, similar MMP, mitochondrial potential and autophagy levels in the cells cultured on graphene and glass control further confirmed high biocompatibility of graphene-based substrates.[15, 132]

The high transparency of monolayer graphene was leveraged to develop transparent MEAs. One of the biggest challenges of current MEA technology is inability to achieve sub-cellular spatial resolution since decreasing the geometric area of a recording site causes an increase in the impedance thus significantly reducing the signal-to-noise ratio (SNR) of the recorded signal. Whereas, optical indicators that can provide sub-cellular spatial resolution, are limited by the temporal resolution either due to kinetics of the chemical reporters or the standard acquisition systems, especially during investigation of a 3D tissue. Therefore, developing transparent electrodes enabled combining electrical recording and optical imaging using fluorescent-based calcium indicators thus leveraging the high temporal resolution and spatial advantages of both the techniques.

Extremely high surface area-to-volume ratio of nanowire-templated 3D fuzzy graphene (NT-3DFG) was leveraged to develop ultra-microelectrodes. Fabricating functional electrodes with smaller footprint is crucial to improve precision and accuracy of cellular recordings and enable fabrication of high-density electrode arrays to study network dynamics of dense cellular networks. Current MEA technology is limited by the significant increase in the electrode impedance upon scaling down of electrode size. To address the challenge, a unique NT-3DFG-based MEA platform was developed that enabled recording of the electrical activity of excitable cells using ultra-microelectrodes ranging from 10 µm down to 2 µm, without the need of any surface coatings. Developing ultra-microelectrodes, as small as an axon, further opens-up possibilities to probe at

sub-cellular scale and investigate activities such as distribution of ion channels and propagation of electrical activity within a single cell, which is not feasible with the current MEA technology.

Finally, NT-3DFG based photothermal stimulation platform was developed where NT-3DFG's unique and extraordinary optical properties and photothermal conversion efficiency was leveraged to modulate electrical activity of the excitable cells. This platform allows non-genetic modulation of cells, unlike optogenetics. Furthermore, it enables stimulation with high spatial and temporal resolution and significantly lower laser energies compared to optogenetics and other nanomaterials that are currently being explored for photothermal stimulation.

All the techniques developed in this thesis allows for the development of next generation platforms to better investigate and modulate the electrical activity of excitable cells. Extensive research has been done in understanding the neurological disorders using electrophysiology tools since these disorders have been linked with the impaired electrical activity in the cellular networks.[20, 32] In addition, the biologists have found that many inherited metabolic diseases affecting the nervous systems are due to defective or deficient enzymes within intracellular organelles, and abnormal protein trafficking and localization.[241-243] The high transparency of monolayer graphene-based MEA platform developed in this thesis can enable investigation of the interplay between biochemical activities such as organelle function and protein trafficking, and electrical activities such as firing frequency, signal amplitude and electrical signal propagation. This information will provide more insight and a better understanding of the pathophysiology of various diseases that could not be deciphered by either electrophysiological investigation or biochemical assays alone.

The small footprint of the NT-3DFG electrodes can be leveraged to develop high density electrode arrays with sub-cellular pitch between electrodes, thus allowing investigation of activity

within as well as across cells. Enabling recordings from dense cellular networks with high precision will enable pin-pointing the exact location of the cells responsible for neurological diseases such as Parkinson's disease. This will not only allow better understanding of the affected circuitry but will also enable more precise target sites for delivering therapeutics thus maximizing the therapeutic effects on the affected area and minimizing the side effects on the normal cells. Furthermore, combining the electrical recording as well as photo-stimulation capabilities of NT-3DFG in the same platform will make it a more powerful tool, thus enabling high density input/output (I/O) interfaces with the cells. This platform will enable a logic-gated feedback loop such that the sensors sense the chemical molecules or electrical activity of the surrounding cells to diagnose a disease progression, and accordingly trigger photo-stimulation to modulate the activity.

In tissue engineering, stimulation of electrical activity of cells has been shown to play a crucial role in the maturation and regeneration of excitable tissues.[38-39, 244] Advances in bioprinting is revolutionizing the field of tissue engineering by enabling printing of tailorable biocompatible scaffolds using components of extracellular matrix.[245-246] The high biocompatibility and small size of NT-3DFGs allow easy integration with such 3D printed scaffolds thus enhancing their functionalities in terms of providing nanotopographical and electrical cues to the cells as well as enable highly controlled stimulation to trigger growth and maturation of cells and tissues.

Another important application is the development of cyborg tissues by integrating NT-3DFG based recording and stimulation platform with neuronal and cardiac organoids. This would enable monitoring and modulation of cellular activity in their 3D microenvironment throughout their development stage. Such platforms will allow better understanding of the tissue development and disease progression which is crucial to develop more efficient therapeutics for various cardiac and neurological disorders.

APPENDIX A: Protocol for nanomaterial synthesis

Monolayer graphene synthesis

1. Cut 2 cm by 6 cm Cu foil (99.8%, Alfa Aesar, uncoated, catalog no. 46365)
2. Sonicate the foil with acetone and isopropyl alcohol (IPA) in an ultrasonic bath for 5 min each followed by N_2 blow dry
3. Treat the foil with a 5.4% w/w HNO_3 solution (CMOS Grade, J.T. Baker, catalog no. JT9606-3) for 30 sec
4. Rinse the foil three times with deionized (DI) water and N_2 blow dry
5. Introduce the foil in the LPCVD system such that the foil sits in the center of the furnace
6. Run the following recipe at 0.5 Torr pressure:
    a. 15 min of ramping up to 1050 °C under 100 sccm Ar
    b. 5 min of stabilization step
    c. 60 min of annealing step under 100 sccm H_2
    d. 8 min of synthesis step under 50 sccm CH_4 (5% in Ar) and 100 sccm H_2
7. Cool down the sample from 1050 °C to 100°C while flowing 100 sccm Ar

Monolayer graphene transfer

1. Cut and tape Cu foil (with graphene) to the glass slide
2. Spin coat PMMA A4 for 45 sec at 4000 rpm on one side
3. Bake the sample after spin-coating for 1 h at 70ºC
4. Cut out the foil from the glass slide
5. Treat the non-coated side with UV/Ozone at 100 ºC for 15 min
6. Float the PMMA-graphene-Cu stack on the Cu etchant (25% $FeCl_3$, 4% HCl, 71% water)

7. While the Cu is etching, clean the transfer substrate with acetone and IPA
8. Treat the substrate with UV/ozone for 10 min at 150 ^{o}C
9. Transfer the PMMA-graphene stack to DI water 3 times
10. Scoop the stack on to the transfer substrate
11. Air dry the sample overnight
12. Bake the sample at 70°C for 1 h
13. Dissolve the PMMA in an acetone bath for 30 mins at 70 °C
14. Rinse the sample with acetone and IPA followed by N_2 blow dry
15. Anneal the sample for 1 h at 300 ^{o}C under 10 sccm H_2 and 300 sccm Ar under ambient pressure

Si nanowire synthesis

1. Cleave (100) Si substrate with a 600 nm wet thermal oxide (p-type, ≤0.005 Ω cm, Nova Electronic Materials Ltd., catalog no. CP02 11208-OX) (Si/600 nm SiO_2) into 2 cm x 1.5 cm or 2 cm x 2 cm chips
2. Clean the substrates with acetone and IPA in an ultrasonic bath for 5 min each, followed by N_2 blow-dry
3. Treat the substrates with UV/ozone for 10 min at 150˚C
4. Functionalize the substrates with 4:1 DI water:poly-L-lysine (PLL) (0.1% w/v, Sigma-Aldrich, catalog no. P8920) for 8 min.
5. Wash the chips gently three times in DI-water
6. Add 30 nm Au nanoparticle (AuNP) solution (Ted Pella, Inc., catalog no. 15706-1) onto the PLL coated substrate for 8 min
7. Wash the chips gently three times in DI-water followed by N_2 blow-dry
8. Introduce the chips into the CVD setup. Once the baseline pressure of $1*10^{-5}$ Torr is reached

a. ramp the temperature to 450°C in 8 min,

b. 5 min stabilization step at 450°C

c. 15 min nucleation step at 450°C under 80 sccm H_2 and 20 sccm SiH_4 (10% in H_2) at 40 Torr

d. 100 min growth step under 60 sccm H_2, 20 sccm SiH_4 and 20 sccm PH_3 (1000 ppm in H_2) at 40 Torr

9. Cool down the samples to room temperature at base pressure.

Si nanowire mesh formation

1. Flow liquid N_2 into the CVD quartz tube with SiNW samples under 200 sccm Ar flow
2. Pump down the system to base pressure of 1e-5 Torr
3. Anneal the mesh for 10 min at 800˚C under 200 sccm H_2 flow at 1.6 Torr
4. Cool down the samples rapidly to room temperature

Nanowire templated 3D fuzzy graphene synthesis

1. Load the SiNW samples (either collapsed or un-collapsed) in the PECVD setup
2. Position the sample at the center of the tube and 4 cm away from the edge of the RF coil
3. Run the following recipe:

    a. temperature ramp up to 800 °C in 13 min

    b. stabilization at 800°C for 5 min under a flow of 100 sccm Ar

    c. synthesis at 800 °C under varying flow rates of CH_4 and varying synthesis time, and exposure to 50 W inductively coupled plasma (generated using a 13.56 MHz RF power supply)

4. Once the synthesis step is done, turn off the plasma and rapidly cool down the sample to 100 ˚C under 100 sccm Ar flow.

APPENDIX B: Protocol for cell-nanomaterial interfaces

Cell culture on graphene-based nanomaterials

Monolayer graphene

1. Anneal the graphene samples at 300 ^{o}C for 60 min under 10 sccm H_2 and 300 sccm Ar at ambient pressure
2. Sterilize the control and graphene samples (n=4 each) in 70% ethanol and at least 2 h UV exposure in the cell culture hood
3. Rinse the samples 3 times with DI water or 1X PBS
4. For **fibroblasts**
    a. Seed the fibroblast cells at a density of 2000 cells/cm^2
    b. Change the media every other day
5. For **cardiomyocytes**
    a. Add 50 µg/mL fibronectin solution (prepared in 1X PBS) to each substrate and incubate at room temperature for 1-3 h
    b. Remove access fibronectin solution and gently rinse the substrates 3 times with 1X PBS (don't let the substrates dry out)
    c. Seed fibronectin-conditioned cardiomyocytes at a density of 400,000 cells/cm^2 in CDM3 media supplemented with 10% FBS and 2 µM thiazovivin
    d. Incubate the samples at 37^{o}C and 5% CO_2 for 7-10 days and replace the media with CDM3 media supplemented with 10% FBS every other day
6. For **neurons**
    a. Add 50 µg/mL poly-D-lysine (PDL) solution prepared in sterile DI water to each substrate and incubate at room temperature for 1-3 h

b. Remove access PDL solution and gently rinse the substrates 3 times with sterile DI water
c. Let the samples dry in the culture hood for 30 min
d. Alternately, substrates can be modified with 50 µg/mL poly-ornithine for 1 h followed by 3 times rinsing with water, and then air dry for 30 min, followed by addition of 20 µg/mL laminin solution and incubation at 37 ^{o}C and 5% CO_2 for another 1 h
e. Seed E18 embryonic hippocampal or cortical neurons at a density of 25000 cells/cm^2 in Neuralbasal media supplemented with 1% glutamax, 1% pen strep and 1X B27
f. Incubate the samples at 37 ^{o}C and 5% CO_2 for at least 7 days and replace 50% of the media with fresh media every other day

3DFG and NT-3DFG

1. Cleave the samples into 1 cm x 0.5 cm dimensions and place 2 samples per well of 24-well plate (since the substrates are hydrophobic, we need to infiltrate them using ethanol)
2. For **fibroblasts**
    a. Add 1 mL ethanol and let it sit for 5 min
    b. Replace 60% ethanol with cell culture media (make sure the sample does not dry out while exchanging the liquid)
    c. Repeat the above step for 5 times to ensure complete removal of ethanol
    d. Add the cells at a density of 2000 cells/cm^2
    e. Change the media every other day
3. For **cardiomyocytes**
    a. Add 1 mL ethanol and let it sit for 5 min
    b. Replace 60% ethanol with 1X PBS and repeat this step for 5 times to ensure complete

removal of ethanol (make sure the sample does not dry out while exchanging the liquid)

c. Remove 600 µL of PBS and add 100 µL of 250 µg/mL fibronectin such that the final concentration is 50 µg/mL
d. Incubate for 1-3 h in the cell culture hood
e. Remove access fibronectin solution and gently rinse the substrates 3 times with 1X PBS (don't let the substrates dry out)
f. Seed fibronectin-conditioned cardiomyocytes at a density of 400,000 cells/cm^2 in CDM3 media supplemented with 10% FBS and 2 µM thiazovivin
g. Incubate the samples at 37^{o}C and 5% CO_2 for 7-10 days and replace the media with CDM3 media supplemented with 10% FBS every other day

4. For **neurons**

a. Add 1 mL ethanol and let it sit for 5 min
b. Replace 60% ethanol with sterile DI water and repeat this step for 5 times to ensure complete removal of ethanol (make sure the sample does not dry out while exchanging the liquid)
c. Remove 600 µL of water and add 100 µL of 250 µg/mL PDL or poly-ornithine such that the final concentration is 50 µg/mL
d. Incubate for 1 h in the cell culture hood
e. Remove the solution and gently clean the substrates 3 times with water
f. Let the samples dry out in the cell culture hood (15-30 min)
g. Add 20 µg/mL laminin solution (prepared in 1X PBS) and incubate at 37^{o}C and 5% CO_2 for another 1 h
h. Remove the solution and gently wash 3 times with PBS

i. Seed E18 embryonic hippocampal or cortical neurons at a density of 25000 cells/cm^2 in Neuralbasal media supplemented with 1% glutamax, 1% pen strep and 1X B27

j. Incubate the samples at 37ºC and 5% CO_2 for at least 7 days and replace 50% of the media with fresh media every other day

Viability assay and quantification

1. Prepare 3-4 samples for each substrate type
2. On the day of assay, transfer the samples to sterile petri dishes or well-plates
3. Add Hoechst 33342 (ThermoFisher, Catalog no. 62249), Calcein AM and Ethidium homodimer (ThermoFisher, catalog no. L3224) dyes at a final concentration of 1 μg/mL, 2 μM and 4 μM, respectively, to each dish/well in sterile conditions
4. Incubate for 15 min at 37ºC and 5% CO_2
5. Gently wash the sample 3 times with 1X PBS
6. Add 1X PBS or Tyrodes buffer in the dish
7. Perform live-cell imaging on a hot plate set to 37 ºC
8. For quantification, compute %viability by:

$$\%Viability = \frac{Total\ cells\ (blue) - Dead\ cells\ (red)}{Total\ cells\ (blue)} X\ 100$$

where blue refers to nuclei stained by Hoechst and red refers to dead cells stained by Ethidium homodimer.

Mitochondrial assay and quantification

1. Prepare 3-4 samples for each substrate type
2. On the day of assay, transfer the sample to a petri dish or a well of a well-plate
3. Add Hoechst 33342 and TMRE dye (ThermoFisher, catalog no. T669) with a final

concentration of 1 µg/mL and 50 nM, respectively

4. Incubate for 20 min at 37ºC and 5% CO_2
5. Gently wash the sample 3 times with 1X PBS
6. Add 1X PBS or Tyrodes buffer in the dish
7. Perform live-cell imaging on a hot plate set to 37 ºC
8. For quantification, calculate the fluorescence intensity of the red channel from at least 50 cells across 3 replicates and compare the intensity with the cells on control substrate. Acquire high magnification single-cell fluorescent images to investigate the mitochondrial morphology
9. Finally, treat the sample with 70% ethanol to induce cell stress and perform imaging with the same laser and camera settings

Autophagy assay and quantification

1. Trypsinize, centrifuge and re-suspend the cells in Resuspension buffer R (Neon kit, ThermoFisher, catalog no. MPK1025)
2. Add 0.25 µg of RFP-LC3 plasmid to 10 µl cell suspension containing ~200,000 cells
3. Electroporate the cells using the Neon Transfection System (ThermoFisher, catalog no. MPK5000) to facilitate transfection
4. Post-transfection, seed the cells on the substrates (n=4 for each substrate type)
5. Incubate at 37ºC and 5% CO_2 for 3 h to allow cell recovery and attachment
6. Following cell attachment, add 2 mL cell culture media
7. For starvation control samples, add serum-free media to the cells; and for transfection control, perform transfection of cells in the absence of the plasmid
8. Incubate the samples for 24-48 h at 37ºC and 5% CO_2
9. Gently wash the cells 3 times with 1X PBS

10. Add fresh media to each sample loaded with Hoechst 33342 dye with a final concentration of 1 µg/mL to stain the nucleus
11. Incubate the samples for 20 min at 37°C and 5% CO_2
12. Gently wash the cells 3 times with 1X PBS and add PBS, Tyrodes buffer or cell culture media for imaging
13. Perform live cell imaging
14. For quantification, count the number of puncta per cell (at least 50 cells across 3 replicates for each condition), and normalize the autophagosome count of each cell by the cell area

Immunostaining

1. Discard the cell culture media and gently wash the cells 3 times with 1X PBS
2. Add 4% paraformaldehyde (Electron Microscopy Sciences, catalog no. 15710) and 0.5% Triton-X 100 (Sigma Aldrich, catalog no. X100) to the samples and incubate for 15 min at room temperature
3. Gently wash the cells 3 times with 1X PBS for 5 min each
4. Add 5% blocking goat serum (ThermoFisher, catalog no. 16210072) and incubate for 30 min
5. Gently wash the cells 3 times with 1X PBS for 5 min each
6. To stain alpha-actinin in cardiomyocytes, add 0.5% anti-alpha actinin antibody (Sigma Aldrich, catalog no. A7811) and incubate for 1 h at room temperature.
7. Gently wash the cells 3 times with 1X PBS for 5 min each
8. Add secondary antibody, goat anti-mouse 555 (ThermoFisher, catalog no. A21422) and incubate for 1 h,
9. Gently wash the cells 3 times with 1X PBS for 5 min each
10. To stain nucleus and actin cytoskeleton staining, add 0.5% DAPI (ThermoFisher, catalog no.

D1306) and 1.5% Alexa Fluor phalloidin 488 (ThermoFisher, catalog no. A12379), respectively, and incubate for 15 min

11. Gently wash the cells 3 times with 1X PBS for 5 min each
12. Add 1X PBS and perform fluorescence imaging

APPENDIX C: Protocol for MEA fabrication

Photolithography and metal patterning

1. Clean Si/SiO_2 substrate by 5 min acetone sonication, IPA rinse and N_2 blow dry
2. Treat the sample with O_2 plasma for 1 min at 100W
3. Spin coat LOR3A photoresist at 600 rpm for 6 sec followed by 4000 rpm for 40 sec
4. Bake at 190 ^oC for 5 min
5. Spin coat Shipley 1805 photoresist at 600 rpm for 6 sec followed by 4000 rpm for 40 sec
6. Bake at 115 ^oC for 5 min
7. Cool to room temperature
8. Using mask aligner and appropriate photomask, expose the sample for 30 sec in vac mode
9. Develop in CD-26 for 0.8 min.
10. Wash with DI water followed by N_2 blow dry
11. Check minimum feature in optical microscope. If underdeveloped, develop for another 0.2 min and recheck in the optical microscope
12. Perform descum step, i.e., O_2 plasma for 1 min at 50W
13. Load the sample in the thermal or e-beam evaporator.
14. Evaporate 10 nm Cr and 100 nm Au or Pt
15. Perform lift off in remover PG at 65^oC for 30-60 min
16. Rinse the sample with acetone and IPA, followed by N_2 blow dry

SU8 passivation

1. Clean the chip with acetone and IPA rinse, followed by N_2 blow dry
2. Spin coat SU8 (SU8 2000.5 for 500 nm, and SU8 2002 for 2 μm) at 600 rpm for 6 sec followed

by 4000 rpm for 40 sec (for 500 nm SU8) or 3000 rpm for 40 sec (for 2 µm SU8)

3. Bake at 65 ^{o}C for 5 min and 95^{o}C for 5 min
4. Align and UV expose using mask aligner for 20 sec with dark field photomask for patterned passivation or bright field photomask for blanket passivation
5. Post bake at 65 ^{o}C for 5 min and 95 ^{o}C for 1 min
6. Develop 1 min in SU8 developer followed by rinsing thoroughly with IPA
7. Inspect the features under optical microscope and develop more if needed
8. Hard bake at 190 ^{o}C for 30 min

Monolayer graphene based MEA

1. Transfer graphene on to the desired MEA substrate using the wet transfer protocol mentioned earlier
2. Perform photolithography with LOR 3A and Shipley S1805 using a bright field photomask such that the LOR-Shipley stack covers the electrode regions
3. Perform reactive ion etching (Plasma Therm 790 RIE) using 14 sccm O_2 and 6 sccm Ar at 20 W power and 10 mTorr pressure for 1 min
4. Strip off the LOR3A/Shipley stack using Remover PG at 65^{o}C for 30-60 min
5. Perform annealing at 300 ^{o}C for 60 min under 10 sccm H_2 and 300 sccm H_2 at ambient pressure
6. Pattern metal lines and contacts (Cr/Au: 10nm/75nm) using photolithography and thermal/e-beam evaporation
7. Passivate the non-electrode region with 500 nm SU8 using the protocol mentioned in the previous section

3DFG and NT-3DFG based MEA

1. Pattern metal lines and contacts on Si/SiO_2 wafer using photolithography and evaporation of 10 nm Cr and 100 nm Pt
2. Cleave the wafer into individual MEA chips
3. For 3DFG MEA, synthesize 3DFG on the chips with Pt lines using the PECVD process
4. For NT-3DFG MEA, pattern 2 nm Au film using photolithography in the sensing regions of the electrodes, followed by SiNW synthesis for 5 min, followed by 3DFG synthesis
5. Deposit 100 nm SiO_2 using Trion PECVD (60 sec at 375 ^oC) on the entire chip; add a control sample to measure the deposited SiO_2 thickness post-deposition using Nanospec/ Ellipsometer
6. Bake the chip at 95^oC for 5 min
7. Perform O_2 plasma treatment for 1 min at 100W
8. Perform photolithography with a dark field mask and expose the electrode regions
9. Develop in CD26 for 1 min and perform O_2 plasma treatment for 1 min at 50W
10. Evaporate 100 nm Cr for hard mask
11. Perform lift-off using PG-Remover at 65 ^oC for 30-60 min
12. Etch the SiO_2 from non-electrode regions using RIE under 22.5 sccm CHF_3 and 16 sccm O_2 at 100mT pressure and 100W power for 5min (etch rate: ~27nm/min)
13. Etch the 3DFG from non-electrode regions using RIE under 16 sccm O_2 and 6 sccm Ar at 10mT pressure and 20W power for 20-60min (20 min etch for 30 min 3DFG and 60 min etch for 90 min 3DFG)
14. Perform Raman characterization to make sure the 3DFG is etched from the non-electrode regions

    If graphene signature is observed, perform the RIE step again prior to the wet etch steps

15. Wet etch Cr for 40 sec using Cr etchant 1020AC (etch rate: ~2.7nm/sec)
16. Wet etch SiO_2 for 60-70 sec using buffer HF (etch rate: ~100nm/min)
17. Treat the chips with HNO_3 (69%) for 2 h
18. Thoroughly rinse the samples with DI water and blow dry them
19. Perform SU8 passivation with 2 µm SU8 (either blanket or patterned) using the protocol described in the previous section

APPENDIX D: Protocol for electrical recording using MEAs

Chip preparation and cell seeding

1. Prepare a reference electrode by dipping one end (few mm) of a Ag wire in bleach for 10 min followed by thorough rinsing with DI water
2. Solder the non-bleached end to the reference pad on the custom-made printed circuit board (PCB) with soldered 36 pin connector (Omnetics, A79024-001), that is compatible with the Intan 32 channel amplifier
3. Tape the MEA chip to the PCB
4. Wire bond the contact pads on the MEA chip to the Au pads on the PCB using a manual wedge wire bonder (West Bond 7476D)
5. Glue a 3D printed PLA based frustum chamber to the center of the chip using PDMS (10:1 PDMS: curing agent) for cell culture
6. Sterilize the chips by adding 70% ethanol to the frustum chamber and exposing the entire chip to UV in the cell culture hood for at least 2 h
7. Rinse the chips 3 times with sterile 1X PBS
8. Add 200 µL of 50 µg/mL fibronectin (prepared in 1X PBS) and incubate for 1-3 h at room temperature in the culture hood
9. Post-incubation, remove the excess fibronectin followed by 3 times 1X PBS wash
10. Seed the fibronectin-conditioned hESC-CMs at a density of 400,000 cells/cm^2 in CDM3 media supplemented with 10% FBS and 2 µM ROCK inhibitor, thiazovivin (Selleck Chemicals, catalog no. S1459)
11. Incubate the chips at 37 ^oC and 5% CO2 for 5-7 days
12. Change the cell culture media every other day with a fresh FBS-supplemented CDM3 media

until the day of recording

Optical and electrical recording

1. At the day of recording, remove the cell culture media from the frustum chamber of each device and gently wash the cells with 1X PBS
2. Add 1X PBS supplemented with 10 µM Fluo-4 AM (ThermoFisher, catalog no. F14217) or 5 µM Cal-520 (AAT Bioquest, catalog no. 21130) to the chamber
3. Incubate for 30 min (for Fluo-4) or 90 min (for Cal-520) at 37^{o}C and 5% CO_2 followed by 30 min incubation at room temperature (for Cal-520 dye)
4. Gently wash the sample 3 times with 1X PBS
5. Add warm Tyrodes buffer in the dish
6. Load the PCB with the MEA chip on to the microscope stage enclosed in a Faraday cage
7. Connect the Omnetics connector on the PCB to a 32-channel Intan amplifier (Make sure to ground yourself while handling the amplifier)
8. Set up the perfusion system with the inline pencil heater (Automate Scientific, Thermoclamp) and a vacuum system
9. Fill in the syringes (held by the bubble stop holder) with Tyrodes buffer and drug-supplemented buffers (label the syringes to avoid confusion)
10. Make sure there are no bubbles in the tubes of the perfusion setup (turn the inline heater control box on only when the liquid is flowing!)
11. Maintain the temperature inside the frustrum chamber by constant perfusion of Tyrode solution maintained at 37^{o}C using the inline heater
12. Dip the Ag/AgCl reference wire (soldered to the PCB) in the frustrum chamber
13. Insert the water dipping objective in the chamber and get the cells in the electrode region in

focus

14. Record the electrical signals using the Intan acquisition system (Intan tech., RHD2000) at an acquisition rate of 20 kHz
15. Simultaneously perform calcium imaging using 488 nm laser
16. Points to consider:
    a. Make sure everything is grounded properly- Faraday cage, Intan acquisition board box, and Thermoclamp pencil
    b. Use a dummy MEA chip to check for baseline noise, prior to using an actual chip with cells
    c. For fluorescence imaging, binning can be used to enhance the signal intensity and reduce the laser power

APPENDIX E: Protocol for photothermal measurements

Photothermal characterization

1. Synthesize 100 min SiNW (non-collapsed) on Si/SiO2 substrates followed by synthesis of 90 min 3DFG
2. Cleave the sample in 5 mm x 5 mm chips
3. Add the sample in a scintillation vial with 100-200 µL of IPA
4. Sonicate for 1-2 sec at power 1 in a bath sonicator
5. Add 1-2 µL of the suspension on a fused silica or quartz substrate
6. Let the IPA evaporate and image under the microscope
7. If the NT-3DFG density is too low, drop-cast more wires
8. Put the NT-3DFG drop-casted sample in a petri dish with 1X PBS
9. Load the sample on the stage of a custom-built microscope setup that is equipped with the external laser source for photo-stimulation
10. Make sure to ground the Faraday cage that encloses the microscope setup
11. Pull pipettes using a pipette puller such that the impedance is ~2MOhm
12. Load the pulled pipette on to the patch clamp probe and attach it to the micro-manipulator
13. Using the micromanipulator get the pipette close to an isolated NT-3DFG while visualizing through the 40X water dipping objective
14. Get the pipette tip 1-2 microns away from the wire
15. Note the temperature of the PBS batch solution using a thermocouple
16. Perform voltage clamp recordings using the patch clamp system at various holding potentials
17. Trigger the laser pulses (with varying pulse durations) using TTL via patch clamp software and apply ~10 repetitions of each type of pulses to enable averaging of the signals

18. Control the power of the laser using the laser control box (use the power meter to characterize the laser power)
19. Once all the measurements are done, insert the same pipette in a petri dish and add 1X PBS at ~50 ^{o}C
20. Monitor the temperature of the PBS solution with a thermocouple while it is dropping down to room temperature and record the resistance value of the pipette at every degree
21. Use the temperature and resistance values to plot the calibration curve that follows the Arrhenius equation ($ln\,(\frac{R}{Ro}) = a \times \frac{1}{T} + c$), where R_o is the pipette resistance at room temperature, R is the resistance measured at a temperature T, and a and c are slope and intercept of the curve, respectively
22. Plot the light-induced current amplitude (ΔI_{light}) vs holding level current (I_o) to determine the contribution from photothermal vs photoelectric effect. The slope is due to photothermal response whereas the y-intercept denotes the photoelectric effect

$$\Delta I_{light}(t) = \left(\frac{R_o}{R(t)} - 1\right) \times I_o + \Delta I_{electric}(t)$$

23. For photothermal effect, use the calibration curve (mentioned in step 21) to calculate the corresponding local temperature change

Photothermal stimulation

Calcium imaging

1. Treat NT-3DFG sample (non-collapsed) with HNO_3 (69% w/w) for 2 h
2. Rinse thoroughly with water
3. Cleave and transfer the sample in a glass vial and sterilize it in 70 % ethanol and UV treatment for 2-12 h

4. Wash thoroughly with sterile DI water or 1X PBS
5. Add 100 µg/mL KF peptide solution and incubate overnight on a shaker
6. Remove the excess solution and add 1X PBS or cell culture media in the vial
7. Sonicate the sample and add the solution to the petri dish with DRG cell culture (2-3 DIV)
8. Check the wire density post 2 h and add more NT-3DFG suspension if needed (it might vary from sample to sample)
9. Incubate the cells with wires at 37 ^{o}C and 5% CO_2 for 2-16 h
10. Incubate the cells with Cal-520 for 90 min at 37^{o}C and 5% CO_2 followed by 30 min incubation at room temperature
11. Gently wash the sample 3 times with 1X PBS
12. Add warm carbogenated Tyrodes buffer in the dish
13. Load the sample on the microscope dish, and make sure the blue laser, bright field and red laser are aligned
14. Perfuse the dish with carbogenated Tyrodes buffer at 22 ^{o}C
15. Note the coordinates of the red laser spot
16. Get the cells in focus using bright field imaging
17. Move the sample such that the cell-NT-3DFG interface aligns with the coordinates of the stimulation laser spot
18. Perform calcium imaging of the cells using blue laser and GFP filter at 5 frames per second (optimize the camera settings prior to stimulation of cells)
19. Apply laser pulses and monitor the calcium activity
20. Modulate the laser power using the laser control box (start with lower laser power and increase if needed)

Patch clamp measurements

1. Prepare the wire suspension and drop-cast them on cells as mentioned in the previous section
2. Pull pipettes of ~3MOhm for whole-cell patch clamping
3. Gently wash the DRG cells with Tyrodes buffer and add few ml of bath solution (132 mM NaCl, 4 mM KCl, 1.8 mM $CaCl_2$, 1.2 mM $MgCl_2$, 10 mM HEPES, and 5 mM D-(+)-glucose, pH 7.4, 300 mOsm)
4. Fill the pulled pipette with internal solution (150 mM KF, 10 mM NaCl, 4.5 mM $MgCl_2$, 2 mM ATP, 9 mM EGTA, and 10 mM HEPES, pH 7.4, 310 mOsm)
5. Mount the pipette to the Ag/AgCl electrode attached to the patch clamp probe
6. Locate a cell with an isolated NT-3DFG on the cell membrane
7. Turn the laser on with a high ND filter (low laser power) to make sure the laser spot is aligned with the cell-wire interface
8. Using the micromanipulators lower the pipette to the cell of interest
9. Once the pipette touches the cell membrane, apply the membrane seal test
10. Apply short suction pulses through the pipette using a syringe to rupture the cell membrane and create a whole-cell patch
11. Record voltage in the current-clamp mode to check the membrane potential
12. Apply electrical pulses to confirm that the cell is a neuron and excitable
13. Apply laser pulses with varying pulse durations and laser powers
    a. power can be adjusted by changing the ND filters
    b. pulse duration can be controlled by software through TTL pulse signals
    c. make sure to start the stimulation experiment with low laser power (1 mW or less) and small pulse duration (10s-100s of μs) and progressively increase the duration and

power until an action potential is observed)

d. perform an electrical stimulation prior to each laser pulse to ensure that the cell is healthy and excitable

14. Perform voltage-clamp recordings to investigate capacitive currents as a result of laser pulses

APPENDIX F: Protocol for 3D microtissues

Casting of agarose microwells

1. Rinse micro-molds (Microtissues®) in DI water.
2. Autoclave the molds and 1g of high quality pure agarose powder for 30 min at dry cycle
3. Add 50 ml of sterile saline [0.9% (w/v) NaCl] to the bottle containing sterilized agarose powder
4. Use microwave oven to boil and completely dissolve the agarose powder. (Stop microwave every 10 seconds and swirl bottle to help dissolve the agarose. Be sure there are no small bits of translucent undissolved agarose)
5. Allow molten agarose to cool to about 60-70^{o}C
6. In a cell culture hood, pipette 500 µl of molten agarose into a 12-series micro-mold. (Avoid creating bubbles while mixing or pipetting agarose)
7. After the agarose has gelled, carefully flex the micro-mold to remove the agarose based microwells
8. Transfer the microwells to a 12 well plate

Cell seeding and microtissues formation

1. Equilibrate the microwells by adding cell culture medium (2.5 ml/well) and incubating for 15 minutes or longer
2. Remove culture medium and replace with fresh medium and repeat the equilibration step once more
3. Prepare the cell suspension either by trypsinization from the culture flask (in case of cardiomyocytes) or dissociation of tissues (in case of neurons)
4. Count the cells and spin them down using centrifuge

5. Calculate the media needed for seeding (190 µL per microwell)
6. Prepare the desired cell density: 81,000 cells/ 190µL for large spheroid micromolds; 256,000 cells/ 190µL for small spheroid micromolds, and 1e6 cells/ 190µL for trough-shaped micromolds
7. Remove the media from the microwells and add the cell suspension gently in the center of the microwell
8. Let the cells settle down for 15 min
9. Add 2.5 mL media in each well of the well plate and incubate at 37ºC with 5% CO_2
10. Replace 50% media every other day

APPENDIX F: Supplementary tables

Table 1. Data summary for the Raman analysis of monolayer graphene (Figure 2.3).

Substrate	Position(G) (cm^{-1})	FWHM(G) (cm^{-1})	Position(2D) (cm^{-1})	FWHM(2D) (cm^{-1})	I_{2D}/I_G	I_D/I_G
Glass coverslip	1572.6 ± 2.4	21.8 ± 2.2	2680.2 ± 4.0	39. 6 ± 3.2	1.90 ± 0.11	0.12 ± 0.01
Si/285nm SiO_2	1580.0 ± 4.0	19.8 ± 3.2	2692.4 ± 6.6	38.0 ± 3.8	1.20 ± 0.09	0.02 ± 0.01

Table 2. Summary of inter-planar spacing determined from SAED patterns of NT-3DFG mesh synthesized under 25.0 mTorr CH_4 partial pressure for 30 min (Figure 2.5)

C-C neighbor	Experiment derived value (nm)	Literature derived value (nm)
1st nearest neighbor	0.119	0.123[247]
2nd nearest neighbor	0.205	0.213[247]
Inter-layer spacing	0.350	0.340[248]

Table 3. Data summary for Raman analysis of NT-3DFG meshes synthesized with varying PECVD conditions (Figure 2.6).

Sample	I_D/I_G	I_{2D}/I_G	Position(D) (cm^{-1})	Position(G) (cm^{-1})	Position(2D) (cm^{-1})	FWHM(G) (cm^{-1})	FWHM(2D) (cm^{-1})
20.0 mtorr	1.11 ±0.12	0.10 ± 0.01	1331.86 ± 1.63	1601.89 ±1.40	2693.47 ±7.44	48.21 ±1.77	139.87 ±21.89
22.7 mTorr	1.64 ±0.22	0.15 ± 0.05	1335.75 ± 1.31	1599.63 ±2.05	2674.38 ±5.45	51.76 ±3.47	97.65 ±8.93
25.0 mTorr	3.43 ±0.51	0.48 ± 0.05	1335.98 ± 1.32	1573.95 ±3.52	2671.85 ±3.64	43.63 ±2.21	92.24 ±6.21

5 min	1.42± 0.12	0.11± 0.02	1346.39± 1.28	1613.40± 1.31	2686.39± 5.25	47.76± 2.48	106.14± 16.07
10 min	3.43± 0.51	0.48± 0.05	1335.98± 1.32	1573.95± 3.52	2671.85± 3.64	43.63± 2.21	92.24± 6.21
30 min	2.67± 0.32	0.40± 0.06	1333.59± 1.89	1568.21± 3.04	2669.06± 2.77	49.39± 1.88	97.67± 3.33
90 min	3.15± 0.27	0.50± 0.03	1335.44± 2.57	1572.35± 3.66	2671.87± 4.39	46.45± 2.11	98.16± 3.15

Table 4. Data summary for dual laser Raman analysis of NT-3DFG synthesized under 25.0 mTorr CH_4 partial pressure for 30 min (Figure 2.6)

Sample	**Region**	**I_D/I_G**	**FWHM(G) (cm^{-1})**	**Disp(G) (cm^{-1} nm^{-1})**
n=1	1	2.38	48.08	0.02
	2	2.65	51.45	0.03
	3	2.35	48.97	0.00
	4	2.48	49.72	0.04
	5	3.13	47.31	0.09
	6	2.55	47.27	0.06
	7	2.76	49.26	0.03
	8	2.82	51.91	0.01
	9	2.47	49.16	0.04
	10	2.15	46.27	0.01
n=2	1	2.33	50.90	0.02
	2	2.52	48.66	0.03
	3	2.32	48.66	0.05
	4	2.21	47.81	0.01
	5	3.01	47.10	0.06
	6	2.76	46.50	0.03
	7	3.25	48.32	0.04
	8	3.16	46.66	0.02
	9	2.36	50.79	0.02
	10	3.12	48.65	0.05
n=3	1	2.79	50.92	0.01
	2	2.51	52.03	0.02

	3	2.73	50.46	0.06
	4	3.27	53.75	0.01
	5	3.00	49.94	0.06
	6	2.46	50.01	0.03
	7	2.73	52.62	0.04
	8	2.62	49.92	0.02
	9	2.80	48.90	0.06
	10	2.35	49.62	0.04

Table 5. Summary of inter-planar spacing determined from SAED patterns of isolated NT-3DFGs synthesized under 25.0 mTorr CH_4 partial pressure for 90 min (Figure 6.1)

C-C neighbor	Experiment derived value (nm)	Literature derived value (nm)
1st nearest neighbor	0.123 ± 0.002	0.123[247]
2nd nearest neighbor	0.212 ± 0.005	0.213[247]
Inter-layer spacing	0.360 ± 0.002	0.340[248]

Table 6. Data summary for Raman analysis of isolated NT-3DFGs synthesized under 25.0 mTorr CH_4 partial pressure for 90 min (Figure 6.2).

Sample	I_D/I_G	I_{2D}/I_G	Position(D) (cm^{-1})	Position(G) (cm^{-1})	Position(2D) (cm^{-1})	FWHM(G) (cm^{-1})	FWHM(2D) (cm^{-1})
90 min NT-3DFG	3.14 ±0.40	0.50 ± 0.05	1347.0 ± 3.0	1585.6 ±4.6	2685.2 ±6.2	52.4 ±5.0	93 ±11.2

Table 7. Data summary for dual laser Raman analysis of isolated NT-3DFGs synthesized under 25.0 mTorr CH_4 partial pressure for 90 min (Figure 6.2)

Sample	NT-3DFG	I_D/I_G	FWHM(G) (cm^{-1})	Disp(G) (cm^{-1} nm^{-1})
N=1	1	3.43	58	0.15
	2	3.06	53	0.11
	3	3.58	52.6	0.08
	4	2.87	51.2	0.1
	5	3.14	54	0.16
	6	2.67	52	0.09
	7	3.34	51.4	0.12
	8	3.33	50.4	0.1
	9	2.89	55.2	0.14
	10	3.1	52.2	0.11
	11	2.65	50	0.07
	12	3.17	51.2	0.05
	13	3.8	54	0.08
	14	2.91	49.4	0.14
	15	3.15	49	0.1
	16	2.54	56.8	0.1
	17	3.27	54.6	0.1
	18	2.67	52	0.12
	19	2.56	54.8	0.09
	20	3.13	61.2	0.09
	21	3.28	53	0.07
	22	3.07	54	0.04
	23	2.81	49.8	0.11
	24	3.16	52.8	0.09
	25	2.89	54.4	0.1
	26	2.98	49.6	0.08
	27	2.8	47.2	0.07
	28	2.98	48.8	0.08
	29	3.73	52	0.07
	30	2.55	49.4	0.08
N=2	1	3.3	54.6	0.1
	2	3.18	52.8	0.11
	3	3.1	47	0.11
	4	2.2	56.4	0.01
	5	2.9	51.2	0.13
	6	3.28	51.8	0.09
	7	3.14	52.6	0.2

	8	2.7	49.6	0.12
	9	2.97	52.4	0.02
	10	2.63	56.8	0.1
	11	3.15	51.2	0.1
	12	3.15	52.4	0.07
	13	3.29	53.8	0.07
	14	3.01	52.6	0.08
	15	3.02	50.8	0.09
	16	4.23	56.8	0.04
	17	2.99	52.4	0.1
	18	3.22	53.2	0.09
	19	2.64	52.2	0.04
	20	2.79	51.6	0.07
	21	2.89	50.2	0.07
	22	3.53	53.2	0.05
	23	3.01	53.4	0.09
	24	2.81	48.8	0.08
	25	3.13	54	0.12
	26	2.9	54.6	0.07
	27	3	50.8	0.09
	28	2.68	51.2	0.08
	29	3.99	57.4	0.07
	30	3.08	53	0.09
N=3	1	3.29	50.2	0.11
	2	2.89	53.2	0.15
	3	3.27	49.6	0.08
	4	2.6	50	0.11
	5	3.3	49.6	0.07
	6	2.62	59	0.06
	7	3.17	51.6	0.12
	8	3.07	52.4	0.11
	9	3.48	49.8	0.07
	10	2.94	51.8	0.14
	11	3.35	51	0.07
	12	3.62	50.4	0.09
	13	3.46	51.2	0.08
	14	3.01	53.6	0.09
	15	3.44	52.6	0.2
	16	4.65	54.8	0.09
	17	2.83	46	0.11
	18	3.81	55.6	0.09

	19	3.51	53.4	0.07
	20	3.18	50.2	0.14
	21	3.31	50	0.09
	22	3.7	59.4	0.14
	23	3.24	50.4	0.06
	24	3.26	54.8	0.13
	25	3.75	49.4	0.07
	26	4.09	56	0.12
	27	3.18	47.4	0.1
	28	2.68	54.4	0.11
	29	2.9	50.8	0.01
	30	3.55	57	0.04

Table 8. Data summary for XPS analysis (atomic percent) for NT-3DFG synthesized under 25.0 mTorr CH_4 partial pressure for 90 min (Figure 6.3)

	Carbon	**Oxygen**	**Nitrogen**
pristine	98.8 ± 0.2	1.2 ± 0.2	-
Nitric treated	96.6 ± 0.1	3.4 ± 0.1	trace
Nitric-treated and KF modified	93.9 ± 0.4	4.0 ± 0.2	2.0 ± 0.2

Table 9. Data summary for XPS analysis (peak positions) for NT-3DFG synthesized under 25.0 mTorr CH_4 partial pressure for 90 min (Figure 6.3)

	Carbon			**Oxygen**		**Nitrogen**	
	C sp^2	**C shake-up**	**O-C=O/ N-C=O**	**C=O**	**C-O**	**C-NH_2**	**NO_3^-**
pristine	284.4 ± 0.0	290.3 ± 0.0	-	532.7 ± 0.1	-	-	-
Nitric treated	284.3 ± 0.0	290.7 ± 0.0	287.6 ± 0.1	532.5 ± 0.0	-	-	405.9 ± 0.2
Nitric-treated and KF modified	284.4 ± 0.0	290.3 ± 0.3	287.8 ± 0.3	531.9 ± 0.0	533.4 ± 0.0	400.2 ± 0.0	406.3 ± 0.1

REFERENCES

1. Feynman, R., There's plenty of room at the bottom. In *Feynman and computation*, CRC Press: 2018; pp 63-76.
2. Ramsden, J., *Nanotechnology: an introduction*. William Andrew: 2016.
3. Poole Jr, C. P.; Owens, F. J., *Introduction to nanotechnology*. John Wiley & Sons: 2003.
4. Fahrner, W., *Nanotechnology and nanoelectronics*. Springer: 2005.
5. Zhang, L.; Webster, T. J., Nanotechnology and nanomaterials: promises for improved tissue regeneration. *Nano today* **2009,** *4* (1), 66-80.
6. Biswas, P.; Wu, C.-Y., Nanoparticles and the environment. *Journal of the Air & Waste Management Association* **2005,** *55* (6), 708-746.
7. Rao, C. N. R.; Müller, A.; Cheetham, A. K., *The chemistry of nanomaterials: synthesis, properties and applications*. John Wiley & Sons: 2006.
8. Guozhong, C., *Nanostructures and nanomaterials: synthesis, properties and applications*. World scientific: 2004.
9. Huczko, A., Template-based synthesis of nanomaterials. *Applied Physics A* **2000,** *70* (4), 365-376.
10. Edelstein, A. S.; Cammaratra, R., *Nanomaterials: synthesis, properties and applications*. CRC press: 1998.
11. Fahlman, B. D., What Is "Materials Chemistry"? In *Materials chemistry*, Springer: 2018; pp 1-21.
12. Ma, Z.; Kotaki, M.; Inai, R.; Ramakrishna, S., Potential of nanofiber matrix as tissue-engineering scaffolds. *Tissue engineering* **2005,** *11* (1-2), 101-109.
13. Goenka, S.; Sant, V.; Sant, S., Graphene-based nanomaterials for drug delivery and tissue engineering. *Journal of Controlled Release* **2014,** *173*, 75-88.
14. Hubbell, J. A.; Chilkoti, A., Nanomaterials for drug delivery. *Science* **2012,** *337* (6092), 303-305.
15. Rastogi, S. K.; Bliley, J.; Shiwarski, D. J.; Raghavan, G.; Feinberg, A. W.; Cohen-Karni, T., Graphene Microelectrode Arrays for Electrical and Optical Measurements of Human Stem Cell-Derived Cardiomyocytes. *Cellular and Molecular Bioengineering* **2018,** *11* (5), 407-418.
16. Rastogi, S. K.; Cohen-Karni, T., Nanoelectronics for Neuroscience. **2019**.

17. Rastogi, S. K.; Kalmykov, A.; Johnson, N.; Cohen-Karni, T., Bioelectronics with nanocarbons. *Journal of Materials Chemistry B* **2018**.

18. Kandel, E. R.; Schwartz, J. H.; Jessell, T. M.; Siegelbaum, S. A.; Hudspeth, A. J., *Principles of neural science*. McGraw-hill New York: 2000; Vol. 4.

19. Nicholls, J. G.; Martin, A. R.; Wallace, B. G.; Fuchs, P. A., *From neuron to brain*. Sinauer Associates Sunderland, MA: 2001; Vol. 271.

20. Josephson, M. E., *Clinical cardiac electrophysiology: techniques and interpretations*. Lippincott Williams & Wilkins: 2008.

21. Cole, K. S.; Curtis, H. J., Electric impedance of the squid giant axon during activity. *The Journal of general physiology* **1939,** *22* (5), 649-670.

22. Galvani, L., ``De viribus electricitatis in motu musculari Commentarius"De bononiensi scientiarum et artium instituto atque academia Commentarii (Bononiae), cited in Bernardi (2000). **1791**.

23. Hodgkin, A. L.; Huxley, A. F., The dual effect of membrane potential on sodium conductance in the giant axon of Loligo. *The Journal of physiology* **1952,** *116* (4), 497.

24. Hodgkin, A.; Huxley, A., The components of membrane conductance in the giant axon of Loligo. *The Journal of physiology* **1952,** *116* (4), 473-496.

25. Hodgkin, A. L.; Huxley, A. F., Currents carried by sodium and potassium ions through the membrane of the giant axon of Loligo. *The Journal of physiology* **1952,** *116* (4), 449.

26. Hodgkin, A. L.; Huxley, A. F.; Katz, B., Measurement of current-voltage relations in the membrane of the giant axon of Loligo. *The Journal of physiology* **1952,** *116* (4), 424-448.

27. Hodgkin, A. L.; Huxley, A. F., Propagation of electrical signals along giant nerve fibres. *Proceedings of the Royal Society of London. Series B, Biological Sciences* **1952**, 177-183.

28. Hodgkin, A. L.; Huxley, A. F., A quantitative description of membrane current and its application to conduction and excitation in nerve. *The Journal of physiology* **1952,** *117* (4), 500.

29. Hodgkin, A. L.; Katz, B., The effect of sodium ions on the electrical activity of the giant axon of the squid. *The Journal of physiology* **1949,** *108* (1), 37.

30. Hodgkin, A.; Huxley, A., Resting and action potentials in single nerve fibres. *The Journal of physiology* **1945,** *104* (2), 176.

31. Hodgkin, A. L.; Huxley, A. F., Action potentials recorded from inside a nerve fibre. *Nature* **1939,** *144* (3651), 710-711.

32. Calabresi, P.; Mercuri, N.; Sancesario, G.; Bernardi, G., Electrophysiology of dopamine-denervated striatal neurons. Implications for Parkinson's disease. *Brain: a journal of neurology* **1993,** *116*, 433-452.

33. Farwell, D.; Gollob, M. H., Electrical heart disease: Genetic and molecular basis of cardiac arrhythmias in normal structural hearts. *Canadian Journal of Cardiology* **2007,** *23*, 16A-22A.

34. Rubaiy, H. N., A short guide to electrophysiology and ion channels. *Journal of Pharmacy & Pharmaceutical Sciences* **2017,** *20*, 48-67.

35. Clare, J. J., Targeting ion channels for drug discovery. *Discovery medicine* **2010,** *9* (46), 253-260.

36. Lebedev, M. A.; Nicolelis, M. A., Brain–machine interfaces: past, present and future. *TRENDS in Neurosciences* **2006,** *29* (9), 536-546.

37. Dvir, T.; Timko, B. P.; Kohane, D. S.; Langer, R., Nanotechnological strategies for engineering complex tissues. *Nature nanotechnology* **2011,** *6* (1), 13.

38. Ghasemi-Mobarakeh, L.; Prabhakaran, M. P.; Morshed, M.; Nasr-Esfahani, M. H.; Baharvand, H.; Kiani, S.; Al-Deyab, S. S.; Ramakrishna, S., Application of conductive polymers, scaffolds and electrical stimulation for nerve tissue engineering. *Journal of tissue engineering and regenerative medicine* **2011,** *5* (4), e17-e35.

39. Tandon, N.; Cannizzaro, C.; Chao, P.-H. G.; Maidhof, R.; Marsano, A.; Au, H. T. H.; Radisic, M.; Vunjak-Novakovic, G., Electrical stimulation systems for cardiac tissue engineering. *Nature protocols* **2009,** *4* (2), 155.

40. Sakmann, B.; Neher, E., Patch clamp techniques for studying ionic channels in excitable membranes. *Annual review of physiology* **1984,** *46* (1), 455-472.

41. Spira, M. E.; Hai, A., Multi-electrode array technologies for neuroscience and cardiology. *Nature nanotechnology* **2013,** *8* (2), 83-94.

42. Edwards, F. A.; Konnerth, A.; Sakmann, B.; Takahashi, T., A thin slice preparation for patch clamp recordings from neurones of the mammalian central nervous system. *Pflügers Archiv European Journal of Physiology* **1989,** *414* (5), 600-612.

43. Kornblum, H. I.; Araujo, D. M.; Annala, A. J.; Tatsukawa, K. J.; Phelps, M. E.; Cherry, S. R., In vivo imaging of neuronal activation and plasticity in the rat brain by high resolution positron emission tomography (microPET). *Nature biotechnology* **2000,** *18* (6), 655-660.

44. Poldrack, R. A.; Farah, M. J., Progress and challenges in probing the human brain. *Nature* **2015,** *526* (7573), 371-379.

45. Hamel, E. J.; Grewe, B. F.; Parker, J. G.; Schnitzer, M. J., Cellular level brain imaging in behaving mammals: an engineering approach. *Neuron* **2015,** *86* (1), 140-159.

46. Hochbaum, D. R.; Zhao, Y.; Farhi, S. L.; Klapoetke, N.; Werley, C. A.; Kapoor, V.; Zou, P.; Kralj, J. M.; Maclaurin, D.; Smedemark-Margulies, N., All-optical electrophysiology in mammalian neurons using engineered microbial rhodopsins. *Nature methods* **2014,** *11* (8), 825-833.

47. Llinás, R. R., Central Nervous System Function. **1988**.

48. Contreras, D., Electrophysiological classes of neocortical neurons. *Neural Networks* **2004,** *17* (5), 633-646.

49. Assad, J. A.; Berdondini, L.; Cancedda, L.; De Angelis, F.; Diaspro, A.; Dipalo, M.; Fellin, T.; Maccione, A.; Panzeri, S.; Sileo, L., Brain function: novel technologies driving novel understanding. In *Bioinspired Approaches for Human-Centric Technologies*, Springer: 2014; pp 299-334.

50. Joye, N.; Schmid, A.; Leblebici, Y., Electrical modeling of the cell–electrode interface for recording neural activity from high-density microelectrode arrays. *Neurocomputing* **2009,** *73* (1-3), 250-259.

51. Polikov, V. S.; Tresco, P. A.; Reichert, W. M., Response of brain tissue to chronically implanted neural electrodes. *Journal of neuroscience methods* **2005,** *148* (1), 1-18.

52. Lagoa, C. E.; Bartels, J.; Baratt, A.; Tseng, G.; Clermont, G.; Fink, M. P.; Billiar, T. R.; Vodovotz, Y., The role of initial trauma in the host's response to injury and hemorrhage: insights from a correlation of mathematical simulations and hepatic transcriptomic analysis. *Shock* **2006,** *26* (6), 592-600.

53. Schwartz, A. B., Cortical neural prosthetics. *Annu. Rev. Neurosci.* **2004,** *27*, 487-507.

54. Leach, J.; Achyuta, A. K. H.; Murthy, S. K., Bridging the divide between neuroprosthetic design, tissue engineering and neurobiology. *Frontiers in neuroengineering* **2010,** *2*, 18.

55. Biran, R.; Martin, D. C.; Tresco, P. A., Neuronal cell loss accompanies the brain tissue response to chronically implanted silicon microelectrode arrays. *Experimental neurology* **2005,** *195* (1), 115-126.

56. Szarowski, D.; Andersen, M.; Retterer, S.; Spence, A.; Isaacson, M.; Craighead, H.; Turner, J.; Shain, W., Brain responses to micro-machined silicon devices. *Brain research* **2003,** *983* (1), 23-35.

57. Turner, J.; Shain, W.; Szarowski, D.; Andersen, M.; Martins, S.; Isaacson, M.; Craighead, H., Cerebral astrocyte response to micromachined silicon implants. *Experimental neurology* **1999,** *156* (1), 33-49.

58. Edell, D. J.; Toi, V.; McNeil, V. M.; Clark, L., Factors influencing the biocompatibility of insertable silicon microshafts in cerebral cortex. *IEEE Transactions on Biomedical Engineering* **1992,** *39* (6), 635-643.

59. Maynard, E.; Hatsopoulos, N.; Ojakangas, C.; Acuna, B.; Sanes, J.; Normann, R.; Donoghue, J., Neuronal interactions improve cortical population coding of movement direction. *Journal of Neuroscience* **1999,** *19* (18), 8083-8093.

60. Biran, R.; Martin, D. C.; Tresco, P. A., The brain tissue response to implanted silicon microelectrode arrays is increased when the device is tethered to the skull. *Journal of Biomedical Materials Research Part A* **2007,** *82* (1), 169-178.

61. Ludwig, K. A.; Uram, J. D.; Yang, J.; Martin, D. C.; Kipke, D. R., Chronic neural recordings using silicon microelectrode arrays electrochemically deposited with a poly (3, 4-ethylenedioxythiophene)(PEDOT) film. *Journal of neural engineering* **2006,** *3* (1), 59.

62. Rousche, P. J.; Normann, R. A., Chronic recording capability of the Utah Intracortical Electrode Array in cat sensory cortex. *Journal of neuroscience methods* **1998,** *82* (1), 1-15.

63. Hatsopoulos, N. G.; Ojakangas, C. L.; Paninski, L.; Donoghue, J. P., Information about movement direction obtained from synchronous activity of motor cortical neurons. *Proceedings of the National Academy of Sciences* **1998,** *95* (26), 15706-15711.

64. Kralik, J. D.; Dimitrov, D. F.; Krupa, D. J.; Katz, D. B.; Cohen, D.; Nicolelis, M. A., Techniques for chronic, multisite neuronal ensemble recordings in behaving animals. *Methods* **2001,** *25* (2), 121-150.

65. Kim, S.; Bhandari, R.; Klein, M.; Negi, S.; Rieth, L.; Tathireddy, P.; Toepper, M.; Oppermann, H.; Solzbacher, F., Integrated wireless neural interface based on the Utah electrode array. *Biomedical microdevices* **2009,** *11* (2), 453-466.

66. Kovacs, G. T.; Stenger, D.; McKenna, T., Enabling technologies for cultured neural networks. *Stenger, DA* **1994**, 121-165.

67. Drake, K. L.; Wise, K.; Farraye, J.; Anderson, D.; BeMent, S., Performance of planar multisite microprobes in recording extracellular single-unit intracortical activity. *IEEE Transactions on Biomedical Engineering* **1988,** *35* (9), 719-732.

68. Robinson, D. A., The electrical properties of metal microelectrodes. *Proceedings of the IEEE* **1968,** *56* (6), 1065-1071.

69. Frey, U.; Egert, U.; Heer, F.; Hafizovic, S.; Hierlemann, A., Microelectronic system for high-resolution mapping of extracellular electric fields applied to brain slices. *Biosensors and Bioelectronics* **2009,** *24* (7), 2191-2198.

70. Scanziani, M.; Häusser, M., Electrophysiology in the age of light. *Nature* **2009,** *461* (7266), 930-939.

71. Fattahi, P.; Yang, G.; Kim, G.; Abidian, M. R., A review of organic and inorganic biomaterials for neural interfaces. *Advanced Materials* **2014,** *26* (12), 1846-1885.

72. Hanein, Y.; Bareket-Keren, L., Carbon nanotube-based multi electrode arrays for neuronal interfacing: progress and prospects. *Frontiers in neural circuits* **2013,** *6*, 122.

73. Garg, R.; Rastogi, S. K.; Lamparski, M.; de la Barrera, S. C.; Pace, G. T.; Nuhfer, N. T.; Hunt, B. M.; Meunier, V.; Cohen-Karni, T., Nanowire-Mesh-Templated Growth of Out-of-Plane Three-Dimensional Fuzzy Graphene. *ACS nano* **2017,** *11* (6), 6301-6311.

74. Novoselov, K. S.; Geim, A. K.; Morozov, S. V.; Jiang, D.; Zhang, Y.; Dubonos, S. V.; Grigorieva, I. V.; Firsov, A. A., Electric field effect in atomically thin carbon films. *science* **2004,** *306* (5696), 666-669.

75. Geim, A. K., Graphene: status and prospects. *science* **2009,** *324* (5934), 1530-1534.

76. Bolotin, K. I.; Sikes, K. J.; Jiang, Z.; Klima, M.; Fudenberg, G.; Hone, J.; Kim, P.; Stormer, H., Ultrahigh electron mobility in suspended graphene. *Solid State Communications* **2008,** *146* (9-10), 351-355.

77. Lee, C.; Wei, X.; Kysar, J. W.; Hone, J., Measurement of the elastic properties and intrinsic strength of monolayer graphene. *science* **2008,** *321* (5887), 385-388.

78. Stoller, M. D.; Park, S.; Zhu, Y.; An, J.; Ruoff, R. S., Graphene-based ultracapacitors. *Nano letters* **2008,** *8* (10), 3498-3502.

79. Nair, R. R.; Blake, P.; Grigorenko, A. N.; Novoselov, K. S.; Booth, T. J.; Stauber, T.; Peres, N. M.; Geim, A. K., Fine structure constant defines visual transparency of graphene. *Science* **2008,** *320* (5881), 1308-1308.

80. Li, D.; Müller, M. B.; Gilje, S.; Kaner, R. B.; Wallace, G. G., Processable aqueous dispersions of graphene nanosheets. *Nature nanotechnology* **2008,** *3* (2), 101.

81. Eda, G.; Fanchini, G.; Chhowalla, M., Large-area ultrathin films of reduced graphene oxide as a transparent and flexible electronic material. *Nature nanotechnology* **2008,** *3* (5), 270.

82. Park, S.; Ruoff, R. S., Chemical methods for the production of graphenes. *Nature nanotechnology* **2009,** *4* (4), 217.

83. Berger, C.; Song, Z.; Li, X.; Wu, X.; Brown, N.; Naud, C.; Mayou, D.; Li, T.; Hass, J.; Marchenkov, A. N., Electronic confinement and coherence in patterned epitaxial graphene. *Science* **2006,** *312* (5777), 1191-1196.

84. Kim, K. S.; Zhao, Y.; Jang, H.; Lee, S. Y.; Kim, J. M.; Kim, K. S.; Ahn, J.-H.; Kim, P.; Choi, J.-Y.; Hong, B. H., Large-scale pattern growth of graphene films for stretchable transparent electrodes. *nature* **2009,** *457* (7230), 706.

85. Li, X.; Cai, W.; An, J.; Kim, S.; Nah, J.; Yang, D.; Piner, R.; Velamakanni, A.; Jung, I.; Tutuc, E., Large-area synthesis of high-quality and uniform graphene films on copper foils. *science* **2009,** *324* (5932), 1312-1314.

86. Mattevi, C.; Kim, H.; Chhowalla, M., A review of chemical vapour deposition of graphene on copper. *Journal of Materials Chemistry* **2011,** *21* (10), 3324-3334.

87. Suk, J. W.; Kitt, A.; Magnuson, C. W.; Hao, Y.; Ahmed, S.; An, J.; Swan, A. K.; Goldberg, B. B.; Ruoff, R. S., Transfer of CVD-grown monolayer graphene onto arbitrary substrates. *ACS nano* **2011,** *5* (9), 6916-6924.

88. Lock, E. H.; Baraket, M.; Laskoski, M.; Mulvaney, S. P.; Lee, W. K.; Sheehan, P. E.; Hines, D. R.; Robinson, J. T.; Tosado, J.; Fuhrer, M. S., High-quality uniform dry transfer of graphene to polymers. *Nano letters* **2011,** *12* (1), 102-107.

89. Liang, X.; Sperling, B. A.; Calizo, I.; Cheng, G.; Hacker, C. A.; Zhang, Q.; Obeng, Y.; Yan, K.; Peng, H.; Li, Q., Toward clean and crackless transfer of graphene. *ACS nano* **2011,** *5* (11), 9144-9153.

90. Kim, S. M.; Hsu, A.; Lee, Y.-H.; Dresselhaus, M.; Palacios, T.; Kim, K. K.; Kong, J., The effect of copper pre-cleaning on graphene synthesis. *Nanotechnology* **2013,** *24* (36), 365602.

91. Vlassiouk, I.; Regmi, M.; Fulvio, P.; Dai, S.; Datskos, P.; Eres, G.; Smirnov, S., Role of hydrogen in chemical vapor deposition growth of large single-crystal graphene. *ACS nano* **2011,** *5* (7), 6069-6076.

92. Blake, P.; Hill, E.; Neto, A. C.; Novoselov, K.; Jiang, D.; Yang, R.; Booth, T.; Geim, A., Making graphene visible. *Applied Physics Letters* **2007,** *91* (6), 063124.

93. Saito, R.; Hofmann, M.; Dresselhaus, G.; Jorio, A.; Dresselhaus, M., Raman spectroscopy of graphene and carbon nanotubes. *Advances in Physics* **2011,** *60* (3), 413-550.

94. Nakahara, M., The Science of Color. Baifukan: 2002.

95. Sanchez, V. C.; Jachak, A.; Hurt, R. H.; Kane, A. B., Biological interactions of graphene-family nanomaterials: an interdisciplinary review. *Chemical research in toxicology* **2011,** *25* (1), 15-34.

96. Chen, D.; Ji, G.; Ma, Y.; Lee, J. Y.; Lu, J., Graphene-encapsulated hollow Fe3O4 nanoparticle aggregates as a high-performance anode material for lithium ion batteries. *ACS applied materials & interfaces* **2011,** *3* (8), 3078-3083.

97. Yang, S.; Feng, X.; Ivanovici, S.; Müllen, K., Fabrication of graphene-encapsulated oxide nanoparticles: towards high-performance anode materials for lithium storage. *Angewandte Chemie International Edition* **2010,** *49* (45), 8408-8411.

98. Luo, J.; Zhao, X.; Wu, J.; Jang, H. D.; Kung, H. H.; Huang, J., Crumpled graphene-encapsulated Si nanoparticles for lithium ion battery anodes. *The journal of physical chemistry letters* **2012,** *3* (13), 1824-1829.

99. Son, I. H.; Park, J. H.; Kwon, S.; Park, S.; Rümmeli, M. H.; Bachmatiuk, A.; Song, H. J.; Ku, J.; Choi, J. W.; Choi, J.-m., Silicon carbide-free graphene growth on silicon for lithium-ion battery with high volumetric energy density. *Nature communications* **2015,** *6*, 7393.

100. Kim, H.; Son, Y.; Park, C.; Cho, J.; Choi, H. C., Catalyst-free direct growth of a single to a few layers of graphene on a germanium nanowire for the anode material of a lithium battery. *Angewandte Chemie International Edition* **2013,** *52* (23), 5997-6001.

101. Lee, J.-H.; Choi, S.-H.; Patole, S. P.; Jang, Y.; Heo, K.; Joo, W.-J.; Yoo, J.-B.; Hwang, S. W.; Whang, D., Reliability enhancement of germanium nanowires using graphene as a protective layer: Aspect of thermal stability. *ACS applied materials & interfaces* **2014,** *6* (7), 5069-5074.

102. Chen, Z.; Ren, W.; Gao, L.; Liu, B.; Pei, S.; Cheng, H.-M., Three-dimensional flexible and conductive interconnected graphene networks grown by chemical vapour deposition. *Nature materials* **2011,** *10* (6), 424.

103. Xu, Y.; Sheng, K.; Li, C.; Shi, G., Self-assembled graphene hydrogel via a one-step hydrothermal process. *ACS nano* **2010,** *4* (7), 4324-4330.

104. Chen, L.; Guo, L.; Wu, Y.; Jia, Y.; Li, Z.; Chen, X., Fabrication of vertically aligned graphene sheets on SiC substrates. *RSC Advances* **2013,** *3* (33), 13926-13933.

105. Zheng, S.; Li, Z.; Wu, Z.-S.; Dong, Y.; Zhou, F.; Wang, S.; Fu, Q.; Sun, C.; Guo, L.; Bao, X., High packing density unidirectional arrays of vertically aligned graphene with enhanced areal capacitance for high-power micro-supercapacitors. *ACS nano* **2017,** *11* (4), 4009-4016.

106. Yang, C.; Bi, H.; Wan, D.; Huang, F.; Xie, X.; Jiang, M., Direct PECVD growth of vertically erected graphene walls on dielectric substrates as excellent multifunctional electrodes. *Journal of Materials Chemistry A* **2013,** *1* (3), 770-775.

107. Hiramatsu, M.; Hori, M., *Carbon Nanowalls: Synthesis and Emerging Applications*. Springer Science & Business Media: 2010.

108. Yu, K.; Bo, Z.; Lu, G.; Mao, S.; Cui, S.; Zhu, Y.; Chen, X.; Ruoff, R. S.; Chen, J., Growth of carbon nanowalls at atmospheric pressure for one-step gas sensor fabrication. *Nanoscale research letters* **2011,** *6* (1), 202.

109. Williams, D. B.; Carter, C. B., The Transmission Electron Microscope. In *Transmission Electron Microscopy*, Springer: 1996; pp 3-17.

110. Bayot, V.; Piraux, L.; Michenaud, J.-P.; Issi, J.-P.; Lelaurain, M.; Moore, A., Two-Dimensional Weak Localization in Partially Graphitic Carbons. *Physical Review B* **1990,** *41* (17), 11770.

111. Rao, A.; Fung, A.; Dresselhaus, M.; Endo, M., Structural Characterization of Heat-Treated Activated Carbon Fibers. *Journal of Materials Research* **1992,** *7* (07), 1788-1794.

112. Śliwińska-Bartkowiak, M.; Drozdowski, H.; Kempiński, M.; Jażdżewska, M.; Long, Y.; Palmer, J. C.; Gubbins, K. E., Structural Analysis of Water and Carbon Tetrachloride Adsorbed in Activated Carbon Fibres. *Physical Chemistry Chemical Physics* **2012,** *14* (19), 7145-7153.

113. Ferrari, A. C.; Basko, D. M., Raman Spectroscopy as a Versatile Tool for Studying the Properties of Graphene. *Nature Nanotechnology* **2013,** *8* (4), 235-246.

114. Torrisi, F.; Hasan, T.; Wu, W.; Sun, Z.; Lombardo, A.; Kulmala, T. S.; Hsieh, G.-W.; Jung, S.; Bonaccorso, F.; Paul, P. J.; Chu, D.; Ferrari, A. C., Inkjet-Printed Graphene Electronics. *ACS Nano* **2012,** *6* (4), 2992-3006.

115. Döbbelin, M.; Ciesielski, A.; Haar, S.; Osella, S.; Bruna, M.; Minoia, A.; Grisanti, L.; Mosciatti, T.; Richard, F.; Prasetyanto, E. A., Light-Enhanced Liquid-Phase Exfoliation and Current Photoswitching in Graphene-Azobenzene Composites. *Nature Communications* **2016,** *7*.

116. Ferrari, A.; Robertson, J., Resonant Raman Spectroscopy of Disordered, Amorphous, and Diamondlike Carbon. *Physical Review B* **2001,** *64* (7), 075414.

117. Sun, H.; Castillo, A. E. D. R.; Monaco, S.; Capasso, A.; Ansaldo, A.; Prato, M.; Dinh, D. A.; Pellegrini, V.; Scrosati, B.; Manna, L., Binder-Free Graphene as an Advanced Anode for Lithium Batteries. *Journal of Materials Chemistry A* **2016,** *4* (18), 6886-6895.

118. van der Pauw, L., A Method of Measuring Specific Resistivity and Hall Effect of Discs of Arbitrary Shape. *Philips Res. Rep* **1958,** *13*, 1-9.

119. Li, X.; Zhu, Y.; Cai, W.; Borysiak, M.; Han, B.; Chen, D.; Piner, R. D.; Colombo, L.; Ruoff, R. S., Transfer of Large-Area Graphene Films for High-Performance Transparent Conductive Electrodes. *Nano Letters* **2009,** *9* (12), 4359-4363.

120. Choi, B. G.; Yang, M.; Hong, W. H.; Choi, J. W.; Huh, Y. S., 3D Macroporous Graphene Frameworks for Supercapacitors with High Energy and Power Densities. *ACS Nano* **2012,** *6* (5), 4020-4028.

121. Worsley, M. A.; Pauzauskie, P. J.; Olson, T. Y.; Biener, J.; Satcher Jr, J. H.; Baumann, T. F., Synthesis of Graphene Aerogel with High Electrical Conductivity. *Journal of the American Chemical Society* **2010,** *132* (40), 14067-14069.

122. Shao, Y.; El-Kady, M. F.; Lin, C. W.; Zhu, G.; Marsh, K. L.; Hwang, J. Y.; Zhang, Q.; Li, Y.; Wang, H.; Kaner, R. B., 3D Freeze-Casting of Cellular Graphene Films for Ultrahigh-Power-Density Supercapacitors. *Advanced Materials* **2016,** *28* (31), 6719-6726.

123. Campbell, A. S.; Jeong, Y. J.; Geier, S. M.; Koepsel, R. R.; Russell, A. J.; Islam, M. F., Membrane/Mediator-Free Rechargeable Enzymatic Biofuel Cell Utilizing Graphene/Single-Wall Carbon Nanotube Cogel Electrodes. *ACS Applied Materials & Interfaces* **2015,** *7* (7), 4056-4065.

124. Kasry, A.; Kuroda, M. A.; Martyna, G. J.; Tulevski, G. S.; Bol, A. A., Chemical doping of large-area stacked graphene films for use as transparent, conducting electrodes. *ACS nano* **2010,** *4* (7), 3839-3844.

125. Bard, A. J.; Faulkner, L. R.; Leddy, J.; Zoski, C. G., *Electrochemical methods: fundamentals and applications*. wiley New York: 1980; Vol. 2.

126. Monk, P. M., *Fundamentals of Electro-Analytical Chemistry*. John Wiley & Sons: 2008; Vol. 29.

127. Li, C. W.; Ciston, J.; Kanan, M. W., Electroreduction of carbon monoxide to liquid fuel on oxide-derived nanocrystalline copper. *Nature* **2014,** *508* (7497), 504.

128. Wang, G.; Zhang, L.; Zhang, J., A review of electrode materials for electrochemical supercapacitors. *Chemical Society Reviews* **2012,** *41* (2), 797-828.

129. Campbell, A. S.; Jose, M. V.; Marx, S.; Cornelius, S.; Koepsel, R. R.; Islam, M. F.; Russell, A. J., Improved Power Density of an Enzymatic Biofuel Cell with Fibrous Supports of High Curvature. *RSC Advances* **2016,** *6* (12), 10150-10158.

130. Jiang, H.; Lee, P. S.; Li, C., 3D Carbon Based Nanostructures for Advanced Supercapacitors. *Energy & Environmental Science* **2013,** *6* (1), 41-53.

131. Zhang, L. L.; Zhao, X., Carbon-Based Materials as Supercapacitor Electrodes. *Chemical Society Reviews* **2009,** *38* (9), 2520-2531.

132. Rastogi, S. K.; Raghavan, G.; Yang, G.; Cohen-Karni, T., Effect of graphene on nonneuronal and neuronal cell viability and stress. *Nano letters* **2017,** *17* (5), 3297-3301.

133. Pinto, A. M.; Gonçalves, I. C.; Magalhães, F. D., Graphene-based materials biocompatibility: a review. *Colloids and Surfaces B: Biointerfaces* **2013,** *111*, 188-202.

134. Zhang, Y.; Nayak, T. R.; Hong, H.; Cai, W., Graphene: a versatile nanoplatform for biomedical applications. *Nanoscale* **2012,** *4* (13), 3833-3842.

135. Liao, K.-H.; Lin, Y.-S.; Macosko, C. W.; Haynes, C. L., Cytotoxicity of graphene oxide and graphene in human erythrocytes and skin fibroblasts. *ACS applied materials & interfaces* **2011,** *3* (7), 2607-2615.

136. Zhang, Y.; Ali, S. F.; Dervishi, E.; Xu, Y.; Li, Z.; Casciano, D.; Biris, A. S., Cytotoxicity effects of graphene and single-wall carbon nanotubes in neural phaeochromocytoma-derived PC12 cells. *Acs Nano* **2010,** *4* (6), 3181-3186.

137. Sasidharan, A.; Panchakarla, L. S.; Sadanandan, A. R.; Ashokan, A.; Chandran, P.; Girish, C. M.; Menon, D.; Nair, S. V.; Rao, C.; Koyakutty, M., Hemocompatibility and macrophage response of pristine and functionalized graphene. *Small* **2012,** *8* (8), 1251-1263.

138. Sasidharan, A.; Panchakarla, L.; Chandran, P.; Menon, D.; Nair, S.; Rao, C.; Koyakutty, M., Differential nano-bio interactions and toxicity effects of pristine versus functionalized graphene. *Nanoscale* **2011,** *3* (6), 2461-2464.

139. Hu, W.; Peng, C.; Lv, M.; Li, X.; Zhang, Y.; Chen, N.; Fan, C.; Huang, Q., Protein corona-mediated mitigation of cytotoxicity of graphene oxide. *ACS nano* **2011,** *5* (5), 3693-3700.

140. Ryoo, S.-R.; Kim, Y.-K.; Kim, M.-H.; Min, D.-H., Behaviors of NIH-3T3 fibroblasts on graphene/carbon nanotubes: proliferation, focal adhesion, and gene transfection studies. *Acs Nano* **2010,** *4* (11), 6587-6598.

141. Kalbacova, M.; Broz, A.; Kong, J.; Kalbac, M., Graphene substrates promote adherence of human osteoblasts and mesenchymal stromal cells. *Carbon* **2010,** *48* (15), 4323-4329.

142. Ruiz, O. N.; Fernando, K. S.; Wang, B.; Brown, N. A.; Luo, P. G.; McNamara, N. D.; Vangsness, M.; Sun, Y.-P.; Bunker, C. E., Graphene oxide: a nonspecific enhancer of cellular growth. *ACS nano* **2011,** *5* (10), 8100-8107.

143. Park, S. Y.; Park, J.; Sim, S. H.; Sung, M. G.; Kim, K. S.; Hong, B. H.; Hong, S., Enhanced differentiation of human neural stem cells into neurons on graphene. *Advanced Materials* **2011,** *23* (36).

144. Li, N.; Zhang, Q.; Gao, S.; Song, Q.; Huang, R.; Wang, L.; Liu, L.; Dai, J.; Tang, M.; Cheng, G., Three-dimensional graphene foam as a biocompatible and conductive scaffold for neural stem cells. *Scientific reports* **2013,** *3*.

145. Li, N.; Zhang, X.; Song, Q.; Su, R.; Zhang, Q.; Kong, T.; Liu, L.; Jin, G.; Tang, M.; Cheng, G., The promotion of neurite sprouting and outgrowth of mouse hippocampal cells in culture by graphene substrates. *Biomaterials* **2011,** *32* (35), 9374-9382.

146. Chong, Y.; Ge, C.; Yang, Z.; Garate, J. A.; Gu, Z.; Weber, J. K.; Liu, J.; Zhou, R., Reduced cytotoxicity of graphene nanosheets mediated by blood-protein coating. *ACS nano* **2015,** *9* (6), 5713-5724.

147. Perry, S. W.; Norman, J. P.; Barbieri, J.; Brown, E. B.; Gelbard, H. A., Mitochondrial membrane potential probes and the proton gradient: a practical usage guide. *Biotechniques* **2011,** *50* (2), 98.

148. Kroemer, G.; Galluzzi, L.; Brenner, C., Mitochondrial membrane permeabilization in cell death. *Physiological reviews* **2007,** *87* (1), 99-163.

149. Chipuk, J.; Bouchier-Hayes, L.; Green, D., Mitochondrial outer membrane permeabilization during apoptosis: the innocent bystander scenario. *Cell Death & Differentiation* **2006,** *13* (8), 1396-1402.

150. Karbowski, M.; Youle, R., Dynamics of mitochondrial morphology in healthy cells and during apoptosis. *Cell Death & Differentiation* **2003,** *10* (8), 870-880.

151. Kroemer, G.; Mariño, G.; Levine, B., Autophagy and the integrated stress response. *Molecular cell* **2010,** *40* (2), 280-293.

152. Kimura, S.; Noda, T.; Yoshimori, T., Dissection of the autophagosome maturation process by a novel reporter protein, tandem fluorescent-tagged LC3. *Autophagy* **2007,** *3* (5), 452-460.

153. Mizushima, N.; Yoshimori, T.; Levine, B., Methods in mammalian autophagy research. *Cell* **2010,** *140* (3), 313-326.

154. Akhavan, O.; Ghaderi, E., Toxicity of graphene and graphene oxide nanowalls against bacteria. *ACS nano* **2010,** *4* (10), 5731-5736.

155. Bove, M.; Grattarola, M.; Martinoia, S.; Verreschi, G., Interfacing cultured neurons to planar substrate microelectrodes: characterization of the neuron-to-microelectrode junction. *Bioelectrochemistry and bioenergetics* **1995,** *38* (2), 255-265.

156. Shmoel, N.; Rabieh, N.; Ojovan, S. M.; Erez, H.; Maydan, E.; Spira, M. E., Multisite electrophysiological recordings by self-assembled loose-patch-like junctions between cultured hippocampal neurons and mushroom-shaped microelectrodes. *Scientific reports* **2016,** *6*, 27110.

157. Herron, T. J.; Lee, P.; Jalife, J., Optical imaging of voltage and calcium in cardiac cells & tissues. *Circulation research* **2012,** *110* (4), 609-623.

158. Qiang, Y.; Seo, K. J.; Zhao, X.; Artoni, P.; Golshan, N. H.; Culaclii, S.; Wang, P. M.; Liu, W.; Ziemer, K. S.; Fagiolini, M., Bilayer Nanomesh Structures for Transparent Recording and Stimulating Microelectrodes. *Advanced Functional Materials* **2017,** *27* (48).

159. Deisseroth, K., Optogenetics. *Nature methods* **2011,** *8* (1), 26.

160. Kuzum, D.; Takano, H.; Shim, E.; Reed, J. C.; Juul, H.; Richardson, A. G.; De Vries, J.; Bink, H.; Dichter, M. A.; Lucas, T. H., Transparent and flexible low noise graphene electrodes for simultaneous electrophysiology and neuroimaging. *Nature communications* **2014,** *5*, 5259.

161. Xia, J.; Chen, F.; Li, J.; Tao, N., Measurement of the quantum capacitance of graphene. *Nature nanotechnology* **2009,** *4* (8), 505.

162. Fang, T.; Konar, A.; Xing, H.; Jena, D., Carrier statistics and quantum capacitance of graphene sheets and ribbons. *Applied Physics Letters* **2007,** *91* (9), 092109.

163. Mummery, C.; Ward, D.; Van Den Brink, C.; Bird, S.; Doevendans, P.; Opthof, T.; La Riviere, D.; Brutel, A.; Tertoolen, L.; Van Der Heyden, M., Cardiomyocyte differentiation of mouse and human embryonic stem cells. *Journal of anatomy* **2002,** *200* (3), 233-242.

164. Caspi, O.; Itzhaki, I.; Kehat, I.; Gepstein, A.; Arbel, G.; Huber, I.; Satin, J.; Gepstein, L., In vitro electrophysiological drug testing using human embryonic stem cell derived cardiomyocytes. *Stem cells and development* **2009,** *18* (1), 161-172.

165. Kehat, I.; Kenyagin-Karsenti, D.; Snir, M.; Segev, H.; Amit, M.; Gepstein, A.; Livne, E.; Binah, O.; Itskovitz-Eldor, J.; Gepstein, L., Human embryonic stem cells can differentiate into myocytes with structural and functional properties of cardiomyocytes. *Journal of clinical investigation* **2001,** *108* (3), 407.

166. Hayakawa, T.; Kunihiro, T.; Ando, T.; Kobayashi, S.; Matsui, E.; Yada, H.; Kanda, Y.; Kurokawa, J.; Furukawa, T., Image-based evaluation of contraction–relaxation kinetics of human-induced pluripotent stem cell-derived cardiomyocytes: Correlation and complementarity with extracellular electrophysiology. *Journal of molecular and cellular cardiology* **2014,** *77*, 178-191.

167. Park, D.-W.; Schendel, A. A.; Mikael, S.; Brodnick, S. K.; Richner, T. J.; Ness, J. P.; Hayat, M. R.; Atry, F.; Frye, S. T.; Pashaie, R., Graphene-based carbon-layered electrode array technology for neural imaging and optogenetic applications. *Nature communications* **2014,** *5*.

168. Duranteau, J.; Chandel, N. S.; Kulisz, A.; Shao, Z.; Schumacker, P. T., Intracellular signaling by reactive oxygen species during hypoxia in cardiomyocytes. *Journal of biological chemistry* **1998,** *273* (19), 11619-11624.

169. Huang, S.; Heikal, A. A.; Webb, W. W., Two-photon fluorescence spectroscopy and microscopy of NAD (P) H and flavoprotein. *Biophysical journal* **2002,** *82* (5), 2811-2825.

170. Pascut, F. C.; Goh, H. T.; Welch, N.; Buttery, L. D.; Denning, C.; Notingher, I., Noninvasive detection and imaging of molecular markers in live cardiomyocytes derived from human embryonic stem cells. *Biophysical journal* **2011,** *100* (1), 251-259.

171. Fu, T.-M.; Hong, G.; Zhou, T.; Schuhmann, T. G.; Viveros, R. D.; Lieber, C. M., Stable long-term chronic brain mapping at the single-neuron level. *Nature methods* **2016,** *13* (10), 875.

172. Kozai, T. D. Y.; Langhals, N. B.; Patel, P. R.; Deng, X.; Zhang, H.; Smith, K. L.; Lahann, J.; Kotov, N. A.; Kipke, D. R., Ultrasmall implantable composite microelectrodes with bioactive surfaces for chronic neural interfaces. *Nature materials* **2012,** *11* (12), 1065.

173. Luan, L.; Wei, X.; Zhao, Z.; Siegel, J. J.; Potnis, O.; Tuppen, C. A.; Lin, S.; Kazmi, S.; Fowler, R. A.; Holloway, S., Ultraflexible nanoelectronic probes form reliable, glial scar–free neural integration. *Science Advances* **2017,** *3* (2), e1601966.

174. Salatino, J. W.; Ludwig, K. A.; Kozai, T. D.; Purcell, E. K., Glial responses to implanted electrodes in the brain. *Nature biomedical engineering* **2017,** *1* (11), 862.

175. Seymour, J. P.; Kipke, D. R. In *Fabrication of polymer neural probes with sub-cellular features for reduced tissue encapsulation*, 2006 International Conference of the IEEE Engineering in Medicine and Biology Society, IEEE: 2006; pp 4606-4609.

176. Maguire, Y. G.; Shapiro, M. G.; Cybulski, T. R.; Glaser, J. I.; Amodei, D.; Stranges, P. B.; Kalhor, R.; Dalrymple, D. A.; Seo, D.; Alon, E., Physical principles for scalable neural recording. *Frontiers in computational neuroscience* **2013,** *7*, 137.

177. Novak, J. L.; Wheeler, B. C., Recording from the Aplysia abdominal ganglion with a planar microelectrode array. *IEEE transactions on biomedical engineering* **1986,** (2), 196-202.

178. Chang, J. C.; Brewer, G. J.; Wheeler, B. C., Microelectrode array recordings of patterned hippocampal neurons for four weeks. *Biomedical Microdevices* **2000,** *2* (4), 245-253.

179. Mathieson, K.; Kachiguine, S.; Adams, C.; Cunningham, W.; Gunning, D.; O'shea, V.; Smith, K.; Chichilnisky, E.; Litke, A.; Sher, A., Large-area microelectrode arrays for recording of neural signals. *IEEE Transactions on Nuclear Science* **2004,** *51* (5), 2027-2031.

180. Maher, M.; Pine, J.; Wright, J.; Tai, Y.-C., The neurochip: a new multielectrode device for stimulating and recording from cultured neurons. *Journal of neuroscience methods* **1999,** *87* (1), 45-56.

181. Kim, R.; Hong, N.; Nam, Y., Gold nanograin microelectrodes for neuroelectronic interfaces. *Biotechnology journal* **2013,** *8* (2), 206-214.

182. Kim, J.-H.; Kang, G.; Nam, Y.; Choi, Y.-K., Surface-modified microelectrode array with flake nanostructure for neural recording and stimulation. *Nanotechnology* **2010,** *21* (8), 085303.

183. Cui, X.; Martin, D. C., Fuzzy gold electrodes for lowering impedance and improving adhesion with electrodeposited conducting polymer films. *Sensors and Actuators A: Physical* **2003,** *103* (3), 384-394.

184. Gabay, T.; Ben-David, M.; Kalifa, I.; Sorkin, R.; Ze'ev, R. A.; Ben-Jacob, E.; Hanein, Y., Electro-chemical and biological properties of carbon nanotube based multi-electrode arrays. *Nanotechnology* **2007,** *18* (3), 035201.

185. Suzuki, I.; Fukuda, M.; Shirakawa, K.; Jiko, H.; Gotoh, M., Carbon nanotube multi-electrode array chips for noninvasive real-time measurement of dopamine, action potentials, and postsynaptic potentials. *Biosensors and Bioelectronics* **2013,** *49*, 270-275.

186. Cui, X.; Lee, V. A.; Raphael, Y.; Wiler, J. A.; Hetke, J. F.; Anderson, D. J.; Martin, D. C., Surface modification of neural recording electrodes with conducting polymer/biomolecule blends. *Journal of biomedical materials research* **2001,** *56* (2), 261-272.

187. Ludwig, K. A.; Langhals, N. B.; Joseph, M. D.; Richardson-Burns, S. M.; Hendricks, J. L.; Kipke, D. R., Poly (3, 4-ethylenedioxythiophene)(PEDOT) polymer coatings facilitate smaller neural recording electrodes. *Journal of neural engineering* **2011,** *8* (1), 014001.

188. Venkatraman, S.; Hendricks, J.; King, Z. A.; Sereno, A. J.; Richardson-Burns, S.; Martin, D.; Carmena, J. M., In vitro and in vivo evaluation of PEDOT microelectrodes for neural stimulation and recording. *IEEE Transactions on Neural Systems and Rehabilitation Engineering* **2011,** *19* (3), 307-316.

189. Meyer, R. D.; Cogan, S. F.; Nguyen, T. H.; Rauh, R. D., Electrodeposited iridium oxide for neural stimulation and recording electrodes. *IEEE Transactions on Neural Systems and Rehabilitation Engineering* **2001,** *9* (1), 2-11.

190. Zhou, H.; Cheng, X.; Rao, L.; Li, T.; Duan, Y. Y., Poly (3, 4-ethylenedioxythiophene)/multiwall carbon nanotube composite coatings for improving the stability of microelectrodes in neural prostheses applications. *Acta biomaterialia* **2013,** *9* (5), 6439-6449.

191. Deng, M.; Yang, X.; Silke, M.; Qiu, W.; Xu, M.; Borghs, G.; Chen, H., Electrochemical deposition of polypyrrole/graphene oxide composite on microelectrodes towards tuning the electrochemical properties of neural probes. *Sensors and Actuators B: Chemical* **2011,** *158* (1), 176-184.

192. Lu, Y.; Lyu, H.; Richardson, A. G.; Lucas, T. H.; Kuzum, D., Flexible neural electrode array based-on porous graphene for cortical microstimulation and sensing. *Scientific reports* **2016,** *6*, 33526.

193. Cogan, S. F.; Guzelian, A. A.; Agnew, W. F.; Yuen, T. G.; McCreery, D. B., Over-pulsing degrades activated iridium oxide films used for intracortical neural stimulation. *Journal of neuroscience methods* **2004,** *137* (2), 141-150.

194. Trasatti, S.; Petrii, O., Real surface area measurements in electrochemistry. *Pure and applied chemistry* **1991,** *63* (5), 711-734.

195. Cogan, S. F., Neural stimulation and recording electrodes. *Annu. Rev. Biomed. Eng.* **2008,** *10*, 275-309.

196. Minev, I. R.; Musienko, P.; Hirsch, A.; Barraud, Q.; Wenger, N.; Moraud, E. M.; Gandar, J.; Capogrosso, M.; Milekovic, T.; Asboth, L., Electronic dura mater for long-term multimodal neural interfaces. *Science* **2015,** *347* (6218), 159-163.

197. Jeong, J.-W.; Shin, G.; Park, S. I.; Yu, K. J.; Xu, L.; Rogers, J. A., Soft materials in neuroengineering for hard problems in neuroscience. *Neuron* **2015,** *86* (1), 175-186.

198. Lacour, S. P.; Courtine, G.; Guck, J., Materials and technologies for soft implantable neuroprostheses. *Nature Reviews Materials* **2016,** *1* (10), 16063.

199. Chen, R.; Canales, A.; Anikeeva, P., Neural recording and modulation technologies. *Nature Reviews Materials* **2017,** *2* (2), 16093.

200. Jiang, Y.; Parameswaran, R.; Li, X.; Carvalho-de-Souza, J. L.; Gao, X.; Meng, L.; Bezanilla, F.; Shepherd, G. M.; Tian, B., Nongenetic optical neuromodulation with silicon-based materials. *Nature protocols* **2019,** *14* (5), 1339.

201. Carvalho-de-Souza, J. L.; Pinto, B. I.; Pepperberg, D. R.; Bezanilla, F., Optocapacitive generation of action potentials by microsecond laser pulses of nanojoule energy. *Biophysical journal* **2018,** *114* (2), 283-288.

202. Wells, J.; Kao, C.; Mariappan, K.; Albea, J.; Jansen, E. D.; Konrad, P.; Mahadevan-Jansen, A., Optical stimulation of neural tissue in vivo. *Optics letters* **2005,** *30* (5), 504-506.

203. Shapiro, M. G.; Homma, K.; Villarreal, S.; Richter, C.-P.; Bezanilla, F., Infrared light excites cells by changing their electrical capacitance. *Nature communications* **2012,** *3*, 736.

204. Jiang, Y.; Li, X.; Liu, B.; Yi, J.; Fang, Y.; Shi, F.; Gao, X.; Sudzilovsky, E.; Parameswaran, R.; Koehler, K., Rational design of silicon structures for optically controlled multiscale biointerfaces. *Nature biomedical engineering* **2018,** *2* (7), 508.

205. Jiang, Y.; Carvalho-de-Souza, J. L.; Wong, R. C.; Luo, Z.; Isheim, D.; Zuo, X.; Nicholls, A. W.; Jung, I. W.; Yue, J.; Liu, D.-J., Heterogeneous silicon mesostructures for lipid-supported bioelectric interfaces. *Nature materials* **2016,** *15* (9), 1023.

206. Carvalho-de-Souza, J. L.; Treger, J. S.; Dang, B.; Kent, S. B.; Pepperberg, D. R.; Bezanilla, F., Photosensitivity of neurons enabled by cell-targeted gold nanoparticles. *Neuron* **2015,** *86* (1), 207-217.

207. Mustata, G.-M.; Kim, Y. H.; Zhang, J.; DeGrado, W. F.; Grigoryan, G.; Wanunu, M., Graphene symmetry amplified by designed peptide self-assembly. *Biophysical journal* **2016,** *110* (11), 2507-2516.

208. Mattevi, C.; Eda, G.; Agnoli, S.; Miller, S.; Mkhoyan, K. A.; Celik, O.; Mastrogiovanni, D.; Granozzi, G.; Garfunkel, E.; Chhowalla, M., Evolution of electrical, chemical, and structural properties of transparent and conducting chemically derived graphene thin films. *Advanced Functional Materials* **2009,** *19* (16), 2577-2583.

209. Deokar, G.; Avila, J.; Razado-Colambo, I.; Codron, J.-L.; Boyaval, C.; Galopin, E.; Asensio, M.-C.; Vignaud, D., Towards high quality CVD graphene growth and transfer. *Carbon* **2015,** *89*, 82-92.

210. Garg, R.; Gopalan, D.; de la Barrera, S. C.; Hafiz, H.; Nuhfer, N. T.; Viswanathan, V.; Hunt, B. M.; Cohen-Karni, T., Electron transport in multi-dimensional fuzzy graphene nanostructures. *Nano letters* **2019**.

211. Polzonetti, G.; Battocchio, C.; Iucci, G.; Dettin, M.; Gambaretto, R.; Di Bello, C.; Carravetta, V., Thin films of a self-assembling peptide on TiO2 and Au studied by NEXAFS, XPS and IR spectroscopies. *Materials Science and Engineering: C* **2006,** *26* (5-7), 929-934.

212. Sai, L.; Chen, J.; Chang, Q.; Shi, W.; Chen, Q.; Huang, L., Protein-derived carbon nanodots with an ethylenediamine-modulated structure as sensitive fluorescent probes for Cu 2+ detection. *RSC Advances* **2017,** *7* (27), 16608-16615.

213. Araújo, M. P.; Soares, O.; Fernandes, A.; Pereira, M.; Freire, C., Tuning the surface chemistry of graphene flakes: new strategies for selective oxidation. *RSC Advances* **2017,** *7* (23), 14290-14301.

214. Stevens, J. S.; de Luca, A. C.; Pelendritis, M.; Terenghi, G.; Downes, S.; Schroeder, S. L., Quantitative analysis of complex amino acids and RGD peptides by X-ray photoelectron spectroscopy (XPS). *Surface and Interface Analysis* **2013,** *45* (8), 1238-1246.

215. Barazzouk, S.; Daneault, C., Amino acid and peptide immobilization on oxidized nanocellulose: spectroscopic characterization. *Nanomaterials* **2012,** *2* (2), 187-205.

216. Landoulsi, J.; Genet, M. J.; Fleith, S.; Touré, Y.; Liascukiene, I.; Méthivier, C.; Rouxhet, P. G., Organic adlayer on inorganic materials: XPS analysis selectivity to cope with adventitious contamination. *Applied Surface Science* **2016,** *383*, 71-83.

217. Fillaux, F.; Menu, S.; Conard, J.; Fuzellier, H.; Parker, S.; Hanon, A.; Tomkinson, J., Inelastic neutron scattering study of the proton dynamics in HNO3 graphite intercalation compounds. *Chemical physics* **1999,** *242* (2), 273-281.

218. Fu, S. Y.; Li, Y. Z.; Chu, W.; Li, C.; Tong, D. G., Monodisperse CuB23 nanoparticles grown on graphene as highly efficient catalysts for unactivated alkyl halide Heck coupling and levulinic acid hydrogenation. *Catalysis Science & Technology* **2015,** *5* (3), 1638-1649.

219. Kim, S.; Kim, K.-H.; Hill, D. J.; Park, H.-G.; Cahoon, J. F., Mie-coupled bound guided states in nanowire geometric superlattices. *Nature communications* **2018,** *9* (1), 2781.

220. Fang, Y.; Jiang, Y.; Acaron Ledesma, H.; Yi, J.; Gao, X.; Weiss, D. E.; Shi, F.; Tian, B., Texturing silicon nanowires for highly localized optical modulation of cellular dynamics. *Nano letters* **2018,** *18* (7), 4487-4492.

221. Kaplan, D. T.; Clay, J. R.; Manning, T.; Glass, L.; Guevara, M. R.; Shrier, A., Subthreshold dynamics in periodically stimulated squid giant axons. *Physical Review Letters* **1996,** *76* (21), 4074.

222. Akerboom, J.; Chen, T.-W.; Wardill, T. J.; Tian, L.; Marvin, J. S.; Mutlu, S.; Calderón, N. C.; Esposti, F.; Borghuis, B. G.; Sun, X. R., Optimization of a GCaMP calcium indicator for neural activity imaging. *Journal of neuroscience* **2012,** *32* (40), 13819-13840.

223. Scemes, E.; Giaume, C., Astrocyte calcium waves: what they are and what they do. *Glia* **2006,** *54* (7), 716-725.

224. Lallouette, J.; De Pittà, M.; Berry, H., Astrocyte networks and intercellular calcium propagation. In *Computational Glioscience*, Springer: 2019; pp 177-210.

225. Berridge, M. J., Neuronal calcium signaling. *Neuron* **1998,** *21* (1), 13-26.

226. Cukierman, E.; Pankov, R.; Stevens, D. R.; Yamada, K. M., Taking cell-matrix adhesions to the third dimension. *Science* **2001,** *294* (5547), 1708-1712.

227. LaPlaca, M. C.; Vernekar, V. N.; Shoemaker, J. T.; Cullen, D. K., Three-dimensional neuronal cultures. *Methods in bioengineering: 3D tissue engineering* **2010**, 187-204.

228. Hindie, M.; Vayssade, M.; Dufresne, M.; Queant, S.; Warocquier-Clérout, R.; Legeay, G.; Vigneron, P.; Olivier, V.; Duval, J. L.; Nagel, M. D., Interactions of B16F10 melanoma cells aggregated on a cellulose substrate. *Journal of cellular biochemistry* **2006,** *99* (1), 96-104.

229. Bursac, N.; Papadaki, M.; White, J. A.; Eisenberg, S. R.; Vunjak-Novakovic, G.; Freed, L. E., Cultivation in rotating bioreactors promotes maintenance of cardiac myocyte electrophysiology and molecular properties. *Tissue engineering* **2003,** *9* (6), 1243-1253.

230. Irons, H. R.; Cullen, D. K.; Shapiro, N. P.; Lambert, N. A.; Lee, R. H.; LaPlaca, M. C., Three-dimensional neural constructs: a novel platform for neurophysiological investigation. *Journal of neural engineering* **2008,** *5* (3), 333.

231. Frega, M.; Tedesco, M.; Massobrio, P.; Pesce, M.; Martinoia, S., Network dynamics of 3D engineered neuronal cultures: a new experimental model for in-vitro electrophysiology. *Scientific reports* **2014,** *4*.

232. Quadrato, G.; Brown, J.; Arlotta, P., The promises and challenges of human brain organoids as models of neuropsychiatric disease. *Nature medicine* **2016,** *22* (11), 1220.

233. Lee, C.-T.; Bendriem, R. M.; Wu, W. W.; Shen, R.-F., 3D brain Organoids derived from pluripotent stem cells: promising experimental models for brain development and neurodegenerative disorders. *Journal of biomedical science* **2017,** *24* (1), 59.

234. Lancaster, M. A.; Renner, M.; Martin, C.-A.; Wenzel, D.; Bicknell, L. S.; Hurles, M. E.; Homfray, T.; Penninger, J. M.; Jackson, A. P.; Knoblich, J. A., Cerebral organoids model human brain development and microcephaly. *Nature* **2013,** *501* (7467), 373.

235. Pamies, D.; Barrera, P.; Block, K.; Makri, G.; Kumar, A.; Wiersma, D.; Smirnova, L.; Zhang, C.; Bressler, J.; Christian, K. M., A human brain microphysiological system derived from induced pluripotent stem cells to study neurological diseases and toxicity. *Altex* **2017,** *34* (3), 362.

236. Kim, S.; Kim, S. Y.; Choi, S.-K.; Bae, J.; Jeon, W. B.; Jang, J. E.; Moon, C., Spheroid Culture of Mammalian Olfactory Receptor Neurons: Potential Applications for a Bioelectronic Nose. *Experimental neurobiology* **2018,** *27* (6), 574-592.

237. Kawada, J.; Kaneda, S.; Kirihara, T.; Maroof, A.; Levi, T.; Eggan, K.; Fujii, T.; Ikeuchi, Y., Generation of a motor nerve organoid with human stem cell-derived neurons. *Stem cell reports* **2017,** *9* (5), 1441-1449.

238. Gualda, E. J.; Simão, D.; Pinto, C.; Alves, P. M.; Brito, C., Imaging of human differentiated 3D neural aggregates using light sheet fluorescence microscopy. *Frontiers in cellular neuroscience* **2014,** *8*, 221.

239. Lee, G.; Lim, J.; Park, J.; Lee, W.; Yoon, D. S.; Kim, S. H.; Kim, M.-K.; Lee, S.-H.; Kim, D.-H., Construction of neurospheroids via surface modified concave microwells. *Journal of industrial and engineering chemistry* **2018,** *62*, 341-351.

240. Mataev, E.; Rastogi, S. K.; Madhusudan, A.; Bone, J.; Lamprinakos, N.; Picard, Y.; Cohen-Karni, T., Synthesis of group IV nanowires on graphene: the case of Ge nanocrawlers. *Nano letters* **2016,** *16* (8), 5267-5272.

241. Kendall, B. E., Disorders of lysosomes, peroxisomes, and mitochondria. *American journal of neuroradiology* **1992,** *13* (2), 621-653.

242. Kann, O.; Kovács, R., Mitochondria and neuronal activity. *American Journal of Physiology-Cell Physiology* **2007,** *292* (2), C641-C657.

243. Xiao, S.; Shaw, R. M., Cardiomyocyte protein trafficking: Relevance to heart disease and opportunities for therapeutic intervention. *Trends in cardiovascular medicine* **2015,** *25* (5), 379-389.

244. Radisic, M.; Park, H.; Shing, H.; Consi, T.; Schoen, F. J.; Langer, R.; Freed, L. E.; Vunjak-Novakovic, G., Functional assembly of engineered myocardium by electrical stimulation of cardiac myocytes cultured on scaffolds. *Proceedings of the National Academy of Sciences* **2004,** *101* (52), 18129-18134.

245. Lee, A.; Hudson, A.; Shiwarski, D.; Tashman, J.; Hinton, T.; Yerneni, S.; Bliley, J.; Campbell, P.; Feinberg, A., 3D bioprinting of collagen to rebuild components of the human heart. *Science* **2019,** *365* (6452), 482-487.

246. Hinton, T. J.; Jallerat, Q.; Palchesko, R. N.; Park, J. H.; Grodzicki, M. S.; Shue, H.-J.; Ramadan, M. H.; Hudson, A. R.; Feinberg, A. W., Three-dimensional printing of complex biological structures by freeform reversible embedding of suspended hydrogels. *Science advances* **2015,** *1* (9), e1500758.

247. Meyer, J. C.; Geim, A. K.; Katsnelson, M. I.; Novoselov, K. S.; Booth, T. J.; Roth, S., The Structure of Suspended Graphene Sheets. *Nature* **2007,** *446* (7131), 60-63.

248. Stankovich, S.; Dikin, D. A.; Piner, R. D.; Kohlhaas, K. A.; Kleinhammes, A.; Jia, Y.; Wu, Y.; Nguyen, S. T.; Ruoff, R. S., Synthesis of graphene-based nanosheets via chemical reduction of exfoliated graphite oxide. *carbon* **2007,** *45* (7), 1558-1565.